# ABSTRACT

Title of dissertation: AN INVESTIGATION OF CIRRUS CLOUD PROPERTIES USING AIRBORNE LIDAR

John Edward Yorks, Doctor of Philosophy, 2014

Dissertation directed by: Russell R. Dickerson
Department of Atmospheric and Oceanic Science

The impact of cirrus clouds on the Earth's radiation budget remains a key uncertainty in assessing global radiative balance and climate change. Composed of ice, and located in the cold upper troposphere, cirrus clouds can cause large warming effects because they are relatively transmissive to short-wave solar radiation, but absorptive of long wave radiation.  Our ability to model radiative effects of cirrus clouds is inhibited by uncertainties in cloud optical properties. Studies of mid-latitude cirrus properties have revealed notable differences compared to tropical anvil cirrus, likely a consequence of varying dynamic formation mechanisms. Cloud-aerosol lidars provide critical information about the vertical structure of cirrus for climate studies. For this dissertation, I helped develop the Airborne Cloud-Aerosol Transport System (ACATS), a Doppler wind lidar system at NASA Goddard Space Flight Center (GSFC). ACATS is also a high spectral resolution lidar (HSRL), uniquely capable of directly resolving backscatter and extinction properties of a particle from high-altitude aircraft. The first ACATS science flights were conducted out of Wallops Island, VA in September of 2012 and included coincident measurements with the Cloud Physics Lidar (CPL) instrument.

In this dissertation, I provide an overview of the ACATS method and instrument design, describe the ACATS retrieval algorithms for cloud and aerosol properties, explain the ACATS HSRL retrieval errors due to the instrument calibration, and use the coincident CPL data to validate and evaluate ACATS cloud and aerosol retrievals. Both the ACATS HSRL and standard backscatter retrievals agree well with coincident CPL retrievals. Mean ACATS and CPL extinction profiles for three case studies demonstrate similar structure and agree to within 25 percent for cirrus clouds. The new HSRL retrieval algorithms developed for ACATS have direct application to future spaceborne missions. Furthermore, extinction and particle wind velocity retrieved from ACATS can be used for science applications such as dust transport and convective anvil outflow.

The relationship between cirrus cloud properties and dynamic formation mechanism is examined through statistics of CPL cirrus observations from more than 100 aircraft flights. The CPL 532 nm lidar ratios (also referred to as the extinction to backscatter ratio) for cirrus clouds formed by synoptic-scale uplift over land are lower than convectively-generated cirrus over tropical oceans. Errors in assuming a constant lidar ratio can lead to errors of ~50% in cloud optical extinction derived from space-borne lidar such as CALIOP. The 1064 nm depolarization ratios for synoptically-generated cirrus over land are lower than convectively-generated cirrus, formed due to rapid upward motions of tropical convection, as a consequence of differences in cloud temperatures and ice particle size and shape. Finally, the backscatter color ratio is directly proportional to depolarization ratio for synoptically-generated cirrus, but not for any other type of cirrus. The relationships between cirrus properties and formation mechanisms determined in this study can be used as part of a larger global climatology of cirrus clouds to improve parameterizations in global climate models and satellite retrievals to improve our understanding of the impact of clouds on weather and climate.

# AN INVESTIGATION OF CIRRUS CLOUD PROPERTIES USING AIRBORNE LIDAR

by

John Edward Yorks

Dissertation submitted to the Faculty of the Graduate School of the
University of Maryland, College Park in partial fulfillment
of the requirements for the degree of
Doctor of Philosophy
2014

Advisor Committee:

Professor Russell R. Dickerson, Chair
Professor Christopher C. Davis, Dean’s Representative
Professor Robert D. Hudson
Professor Zhanqing Li
Adjunct Professor Matthew J. McGill
Adjunct Professor Anne M. Thompson

# Preface

The focus of this dissertation is two fold: introducing and assessing a new airborne HSRL technique to directly retrieve cloud and aerosol properties using the Airborne Cloud-Aerosol Transport System (ACATS) and investigating the relationship between cirrus cloud properties and formation mechanism using airborne lidar data from the Cloud Physics Lidar (CPL). This dissertation is organized into six chapters. The first chapter outlines the current understanding and importance of cirrus clouds, as well as the role of lidar systems in collecting measurements of cirrus properties. Chapter 2 provides an overview of the ACATS method and instrument design, describes the ACATS retrieval algorithms for cloud and aerosol properties, explains the sensitivity of the ACATS HSRL retrieval errors to the instrument calibration, and demonstrates the data products derived from ACATS using initial results from the first science flights. Chapter 3 discusses the validation and evaluation of ACATS cloud and aerosol retrievals for both the standard and HSRL methods using coincident CPL data. Chapter 4 focuses on the relationship between cirrus cloud properties and dynamic formation mechanism, examined through statistics of CPL cirrus properties from more than 100 flights. Chapter 5 outlines the ACATS wind retrieval algorithms and future work to assess the ACATS wind products, while Chapter 6 summarizes the finding of the dissertation. Chapters 2 and 3 have been submitted to the *Journal of Atmospheric and Oceanic Technology* in 2014 and are currently under the peer-review process (Yorks *et al.* 2014a; 2014b). Chapter 4 is in preparation for submission to a peer-reviewed journal.

# Acknowledgements

I would like to thank the people that have helped guide me both personally and professionally through the past 5 years. To Haley, thank you for your love and support, especially in the past few months. Mom and Dad, thank you for believing in me and encouraging me to pursue my goals. I would particularly like to thank Matt, Anne, Russ, Rich Clark, and Sepi Yalda for the opportunities, mentorship, and constructive criticism that have helped shape me into the scientist I am today. A special thanks to the entire CPL/CATS team (Dennis Hlavka, Steve Palm, Bill Hart, Andrew Kupchock, Patrick Selmer, Stan Scott) for their help with data analysis and algorithm development the past 6 years. Finally, I would like to thank Mark Vaughan and Melody Avery for their help with the CALIPSO data shown in the dissertation, as well as Bastiaan van Diendenhoven for providing helpful interpretation of RSP data.

# Table of Contents

# List of Tables

Table Page

# List of Figures

# List of Abbreviations

| | |
|---|---|
| ACATS | Airborne Cloud-Aerosol Transport System |
| AMCS | Advanced MultiChannel Scaler |
| APB | Attenuated Particulate Backscatter |
| ATB | Attenuated Total Backscatter |
| ATTREX | Airborne Tropical Tropopause Experiment |
| CATS | Cloud-Aerosol Transport System |
| CALIOP | Cloud-Aerosol Lidar with Orthogonal Polarization |
| CALIPSO | Cloud-Aerosol Lidar and Infrared Pathfinder Satellite Observation |
| CC-VEX | CALIPSO-CloudSat Validation Experiment |
| CIN | Cloud Integrating Nephelometer |
| CLASIC | Cloud and Land Surface Interaction Campaign |
| COD | Cloud Optical Depth |
| CPI | Cloud Particle Imager |
| CPL | Cloud Physics Lidar |
| DEDG | Double-Edge Technique |
| EDG | Edge Technique |
| FOV | Field-Of-View |
| FSSP | Forward Scattering Spectrometer Probe |
| FWHH | Full-Width Half Height |
| GCM | General Circulation Model |
| GLOW | Goddard Lidar Observatory for Winds |
| GPS | Global Positioning System |
| GSFC | Goddard Space Flight Center |
| HOE | Holographic Optic Element |
| HSRL | High Spectral Resolution Lidar |
| HS3 | Hurricane and Severe Storms Sentinel |
| ICEAX | ICESat-2 Arctic eXperiment |
| ICESat-2 | Ice, Cloud and land Elevation Satellite 2 |
| IMU | Inertial Measurement Unit |
| IN | Ice Nuclei |
| IR | Infrared |
| ISS | International Space Station |
| LOS | Line-Of-Sight |
| LW | Longwave |
| MABEL | Multiple Altimeter Beam Experimental Lidar |
| MC | Multi-Channel |
| NASA | National Aeronautics and Space Administration |
| Nd:YAG | Neodymium Yttrium Aluminum Garnet |
| Nd:YVO4 | Neodymium-doped Yttrium Orthovanadate |
| OHP | Observatoire de Haute Provence |
| PDF | Probability Density Function |
| PODEX | Polarimeter Definition Experiment |
| RSP | Research Scanning Polarimeter |
| SAA | South American Anomaly |

| | |
|---|---|
| SBIR | Small Business Innovative Research |
| SEAC$^4$RS | Studies of Emissions and Atmospheric Composition, Clouds and Climate Coupling by Regional Surveys |
| SNR | Signal-to-Noise Ratio |
| SPEC | Stratton Park Engineering Company |
| T | Temperature |
| TC4 | Tropical Composition, Cloud and Climate Coupling mission |
| THORPEX | The Observing System Research and Predictability Experiment |
| TTL | Tropical Tropopause Layer |
| UAV | Unmanned Aerial Vehicle |
| UTC | Coordinated Universal Time |
| WAVE | Wallops Airborne Vegetation Experiment |
| 2D-S | 2 Dimensional Stereo probe |

# List of Symbols

| | |
|---|---|
| $A_n$ | etalon transmission parameter |
| $A_T$ | telescope area |
| $\alpha$ | attenuated particulate backscatter |
| $\alpha_0$ | attenuated particulate backscatter uncertainty |
| $\alpha_{ac}$ | azimuth angle in aircraft-relative coordinates |
| b | laser beam vector |
| $b_{ac}$ | laser beam vector in aircraft-relative coordinates |
| $B_D$ | detector noise background signal |
| $B_S$ | solar background signal |
| $b_t$ | laser beam vector in track-relative coordinates |
| $\beta_p$ | particulate backscatter coefficient |
| $\beta_m$ | molecular backscatter coefficient |
| c | speed of light |
| $\chi$ | backscatter color ratio |
| d | etalon spacing |
| D | aircraft drift |
| $D_{MET}$ | horizontal wind direction in meteorological coordinates |
| $\delta$ | depolarization ratio |
| $E_T$ | transmitted laser energy (J) |
| $\varepsilon$ | relative error |
| $\phi$ | earth-relative elevation angle |
| $\phi_{ac}$ | elevation angle in aircraft-relative coordinates |
| g | asymmetry parameter |
| G | generalized matrix to be inverted |
| $\gamma$ | attenuated total backscatter |
| h | Planck's constant |
| H | aircraft heading |
| $\eta$ | detector normalization coefficient |
| j | channel number |
| $\varphi$ | observation zenith angle |
| $\ell$ | path length |
| L | etalon plate loss |
| $L_{GPS}$ | distance between antenna and GPS |
| $\lambda$ | wavelength |
| $\lambda_0$ | center position of the laser linewidth |
| $\lambda_c$ | center wavelength of the etalon |
| M | order of interference |
| $M_H$ | conversion matrix for aircraft heading |
| $M_P$ | conversion matrix for aircraft pitch |
| $M_R$ | conversion matrix for aircraft roll |
| n | number of iterations |
| N | number of photon counts |
| $n_c$ | number of detector channels |

| | |
|---|---|
| $N_{FSR}$ | free spectral range in units of channels |
| $\nu_t$ | particle terminal velocity |
| $O_A$ | overlap correction function |
| $P$ | aircraft pitch |
| $P_m$ | molecular backscatter phase function |
| $P_p$ | particulate backscatter phase function |
| $P_{tot}$ | total scattering phase function |
| $Q_E$ | detector quantum efficiency |
| $\theta$ | off-nadir angle of the laser beam |
| $\theta_{ac}$ | rotation angle in aircraft-relative coordinates |
| $\Theta$ | scattering angle |
| $r$ | range to scattering particles |
| $R$ | etalon plate reflectivity |
| $R_{eff}$ | particle effective radius |
| $S_p$ | lidar ratio |
| $\sigma$ | total extinction coefficient |
| $\sigma_p$ | particulate extinction coefficient |
| $\sigma_m$ | molecular extinction coefficient |
| $T$ | transmission |
| $T_F$ | transmission of receiver filters |
| $T_m^2$ | two-way molecular transmission |
| $T_O$ | transmission of optics |
| $T_p^2$ | two-way molecular transmission |
| $\tau_{ac}$ | tilt angle in aircraft-relative coordinates |
| $\tau_p$ | particulate optical depth |
| $u$ | u-component of horizontal wind (east-west) |
| $U_{LOS}$ | line-of-sight wind velocity |
| $U_{LOS,0}$ | line-of-sight wind velocity uncertainty |
| $v$ | v-component of horizontal wind (north-south) |
| $V$ | horizontal wind velocity vector |
| $V_a$ | apparent antenna motion |
| $V_{ac}$ | aircraft velocity vector |
| $VG_{ac}$ | horizontal component of aircraft velocity |
| $w$ | w-component of horizontal wind (vertical) |
| $W$ | weighting matrix |
| $WG_{ac}$ | vertical component of aircraft velocity |
| $\omega$ | attenuated molecular backscatter |
| $\omega_0$ | attenuated molecular backscatter uncertainty |
| $\Omega_{ac}$ | aircraft-relative coordinates |
| $\Delta\lambda_{FSR}$ | free spectral range in units of wavelength |
| $\Delta d_D$ | etalon defect parameter |
| $\Delta r$ | range bin width |
| $\Delta\lambda_L$ | laser broadening (1/e width) |
| $\Delta\lambda_M$ | molecular broadening (1/e width) |
| $\Delta\chi$ | weighted least-squares solution |

# Chapter 1: Introduction

## 1.1 Importance and Understanding of Cirrus Clouds

Ice clouds in the upper troposphere, hereinafter referred to as cirrus, have a significant effect on the earth's radiation balance and climate, as demonstrated by general circulation model (GCM) and satellite studies (Ackerman *et al.* 1988; Stephens *et al.* 1990). For example, cirrus can significantly reduce the outgoing longwave (LW) radiation as a consequence of their location in the cold upper troposphere while, at the same time, remaining relatively transmissive to shortwave radiation (Stephens 2005). McFarquhar *et al.* (2000) and Bucholtz *et al.* (2010) found that thin cirrus have radiative heating rates in the upper troposphere of 2-3 K per day and radiative forcings up to 2 W $m^2$. This reduction in outgoing LW flux is estimated to be about 10% (Santacesaria *et al.* 2003). In addition to their radiative importance, cirrus are a source of dehydration in the upper troposphere due to depletion of water vapor in regions of supersaturation and radiative heating of upper tropospheric air as it ascends into the stratosphere (Jensen *et al.* 1996a; Gettelman *et al.* 2002; Jensen and Pfister 2004). Thus, cirrus may indirectly affect stratospheric ozone chemistry (Dvortsov and Solomon 2001) and transport of atmospheric trace gases from convective detrainment levels up to the stratosphere (Poulida *et al.* 1996). Despite the influence on the earth's climate system, there are many outstanding issues regarding cirrus properties and formation, which introduce uncertainty into cirrus parameterization schemes employed in numerical models (Del Genio 2002; Powell *et al.* 2012).

Measurements of cirrus microphysical properties have been limited over the last 30 years compared to other cloud types and have focused on the tropical regions. Thin cirrus, classified as cirrus with optical depths less than 0.30, are typically concentrated around regions of strong convection in the tropics, where thin cirrus cloud fractions have been reported in previous studies around 30%–60% and as high as 90% (McFarquhar *et al.* 2000; Comstock *et al.* 2002; Mace *et al.* 2009; Martins *et al.* 2011). Thin cirrus particles exhibit a bimodal distribution of sizes, as measured by airborne particle size spectrometers used to derive a total spherical particle volume per unit volume of air. This involves assuming that the measured particles are spheres. Previous measurements of particles in ice clouds over the range -80 to -20 C have yielded a small particle mode with diameters in the sub-100 μm size range and a large particle mode in excess of several hundred microns (McFarquhar and Heymsfield 1996; Heymsfield *et al.* 2002; Lawson *et al*. 2006a; Zhao *et al.* 2011). The instruments previously used to measure ice particle size suffer from the effects of large ice particle shattering on the probe tips, which can lead to an overestimation of small ice particle concentrations (Jensen *et al*. 2009; Zhao *et al.* 2011). Nonetheless, it is theorized the bimodal distribution of ice particle size evolves naturally within cirrus due to normal condensational growth and sedimentation (Khvorostyanov and Curry 2008; Zhao *et al.* 2011).

There are many varying theories on the formation mechanisms of cirrus clouds. The most commonly observed generation mechanism for tropical cirrus is anvil outflow from deep convective updrafts. Rickenbach (1999) and Jensen *et al.* (1996b) observed that thin tropic cirrus with small ice crystals often form as convective anvil clouds that became detached from their thunderstorm due to directional wind shear. An alternative theory is that deep convective storms induce vertical wave activity (Potter and Holton 1995). These vertically propagating waves transport moisture near the tropopause and lead to cloud formation (Santacesaria *et al.* 2003). Garrett *et al.* (2004) theorize that thin cirrus near the tropopause form above anvil cirrus as a result of convection and turbulent mixing, and may be persistent even after the convection has subsided because of the radiative cooling effects of the underlying anvil cloud. Cirrus near the tropical tropopause can also form in situ due to cooling of air in the tropopause layer (Pfister *et al.* 2001; Gettelman *et al.* 2002; Jensen *et al.* 2005). In the mid-latitudes, a variety of synoptic-scale lifting mechanisms such as the jet stream, closed upper level troughs, and frontal systems can elevate layers of moist air and promote homogeneous nucleation (Jensen *et al*. 1996b; Massie *et al*. 2002; Sassen 2002). The mechanism and geographic location of cirrus formation play a large role in the cloud temperatures, vertical velocities, and source of ice nuclei of the cloud and thus are related to cirrus properties such as extinction, ice water content (IWC), ice crystal number densities, and crystal sizes. Providing measurements of cloud physical and microphysical properties to test and improve cloud parameterizations in GCMs is a priority in current climate change research.

Measurements of mid-latitude cirrus have indicated notable differences compared to tropical anvil cirrus, likely a consequence of varying formation mechanisms (Sassen and Benson 2001; Wang and Sassen 2002; Martins *et al.* 2011; Yorks *et al*. 2011a). Limited sets of in situ and remote sensing measurements exist in the mid-latitudes despite observed thin cirrus frequencies (number of cirrus observations versus total observations) as high as 30-40% in mid-latitude regions (Wang and Sassen 2002; Martins *et al.* 2011). In situ measurements of mid-latitude cirrus found a bimodal distribution of sizes, including a small particle mode with diameters in the sub-100 μm diameter size range (Heymfield *et al.* 2002; Lawson *et al.* 2006a). However, recent measurements of convective anvils from the tropics show a higher frequency of larger particles in the 100 – 400 μm diameter range (Lawson *et al.* 2010). Mid-latitude cirrus ice particle habits observed using a Cloud Particle Imager (CPI; Lawson *et al.* 2001) display rosette shapes as shown in Figure 1.1, but these habits are rarely observed in convective turrets and anvils (Lawson *et al.* 2006a; 2010). Additionally, columns are more commonly observed in tropical cirrus than mid-latitude cirrus (Noel *et al.* 2004; Lawson *et al.* 2006a). To improve cirrus parameterizations in global climate models, a global climatology of cirrus clouds is necessary; this should include information about how cirrus properties vary by region or generation mechanism. A combination of both in situ and remote sensing measurements from field campaigns conducted in both the tropics and mid-latitudes is necessary to develop this climatology.

Aircraft remote sensing instruments can provide data with higher temporal resolution than in situ instruments and higher spatial resolution compared to their space-based counterparts. Elastic backscatter lidars such as the Cloud Physics Lidar (CPL; McGill *et al.* 2002) and Cloud-Aerosol Lidar with Orthogonal Polarization (CALIOP) aboard the Cloud-Aerosol Lidar and Infrared Pathfinder Satellite Observation (CALIPSO; Winker *et al.* 2009) satellite provide information on cirrus particle shape and optical properties. The optical property of greatest importance to estimates of cirrus shortwave radiative flux is the extinction or optical depth (COD), expressing the quantity of light removed from a beam by scattering or absorption during its path through the cirrus layer. Although statistics of cirrus properties have been examined using lidar data in past research (e.g., Sassen and Benson 2001; Vaughan *et al*. 2010; Yorks *et al*. 2011a), there are still lingering questions as to their global variability and relationship with cloud generation mechanisms.

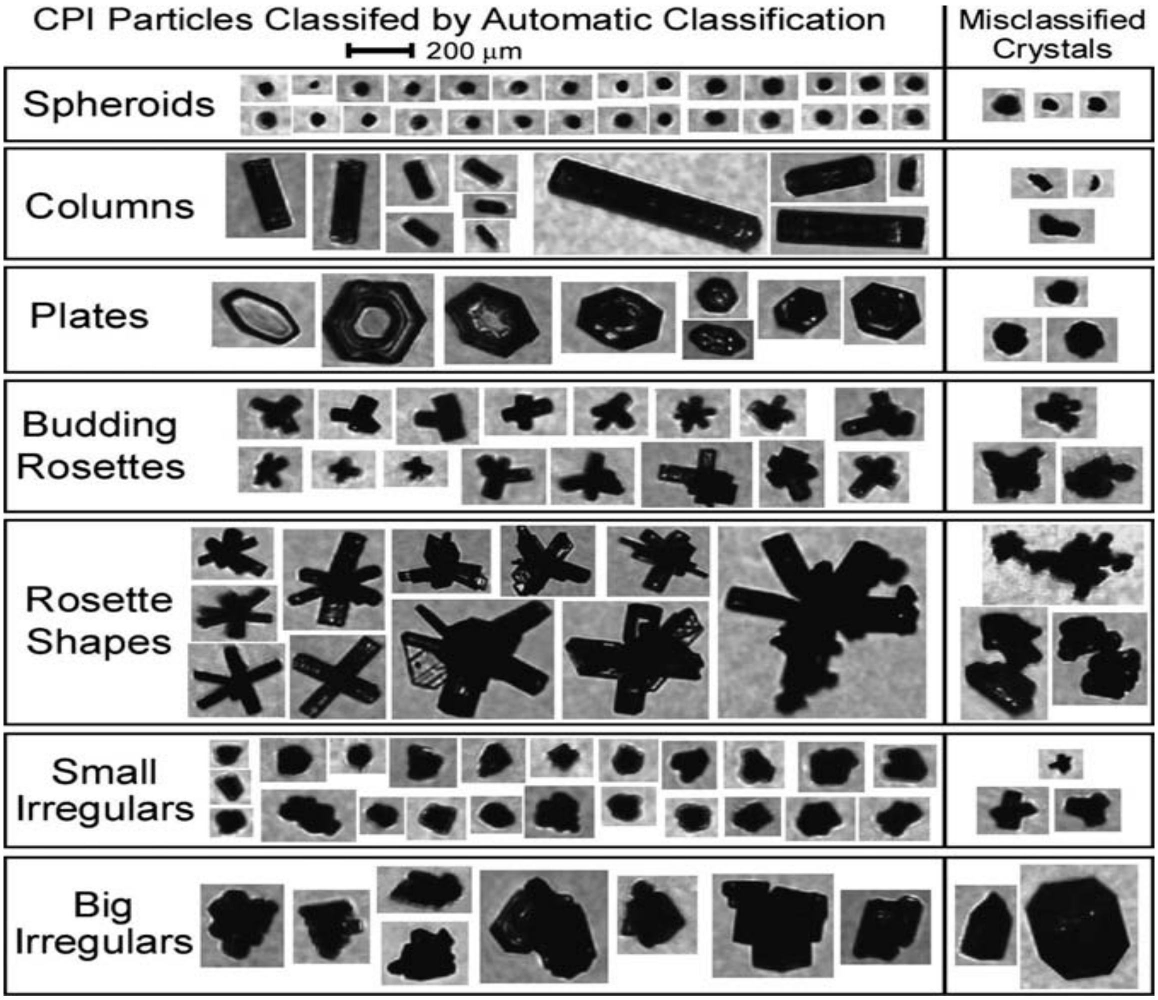

**Figure 1.1.** The ice particle habits distinguished from the CPI instrument as presented in Lawson *et al.* (2006). Rosette and irregular shapes dominate mid-latitude cirrus clouds.

Cirrus optical properties retrieved using lidar data can be related to cirrus microphysical parameters. For example, the depolarization ratio can be related to ice particle shape using its relationship to particle aspect ratio (Noel *et al*. 2004). Pulsed lasers commonly used in backscatter lidar systems naturally produce linearly polarized light. Using a beam splitter in the receiver optics, the perpendicular and parallel planes of polarization of the backscattered light are measured. The linear volume depolarization ratio is defined as the ratio of perpendicular total (Rayleigh plus particle) backscatter to parallel total backscatter, and has values between 0.2 and 0.6 for non-spherical particles such as ice crystals (Sassen and Benson 2001; Yorks *et al*. 2011a). Particles with large aspect ratios (ratio of length to width) such as columns have depolarization ratios of 0.5 to 0.6, while spheroids have lower depolarization ratios (near 0.2). Uncertainties in particle shape parameterizations can produce errors in the cirrus bidirectional reflectance and optical depth estimates (Stephens *et al.* 1990; Mishchenko *et al.* 1996; Yang *et al*. 2001).

The extinction-to-backscatter ratio, also known as the lidar ratio, is defined for atmospheric scatterers as the ratio of the volume extinction coefficient $\sigma(r)$ with units of $\text{km}^{-1}$ to the volume angular backscatter coefficient $\beta(\pi,r)$ with units of $\text{km}^{-1}\ \text{sr}^{-1}$. The lidar ratio has units of sr, since the backscatter is a function of range and angle, and is equivalent to the inverse of the single scattering albedo, multiplied by the phase function at 180 degrees. Thus, it is a function of cloud albedo and particle extinction. For tropospheric clouds, the light scattered back at 180 degrees is only a small fraction of the total extinction, so the lidar ratio typically varies from about 10 to 60 sr (Del Guasta et al. 2001; Yorks *et al*. 2011a). Seifert *et al*. (2007) found mean 532 nm lidar ratios for cirrus clouds of 33 ± 9 sr over the Maldives (4 degree North). Yorks *et al*. (2011a) analyzed statistics and trends of the 532 nm lidar ratio for four years of CPL data during five projects that occurred in varying geographic locations and meteorological seasons. They found that the lidar ratio for cirrus clouds varied between 20 and 30 sr for the five different projects and hypothesize that differences in formation mechanisms may contribute to the variability in lidar ratio. Cirrus with a lidar ratio near 20 sr either have a larger cloud albedo or lower cloud optical depth (COD) than cirrus with lidar ratios near 30 sr.

The lidar ratio is important because it is an intermediate variable solved through iterations of the singular lidar equation used for the retrieval of extinction and backscatter coefficients from elastic backscatter lidar data (Fernald *et al.* 1972). The CALIPSO and CPL standard data products and processing algorithms apply a parameterized layer-specific lidar ratio to retrieve optical depth (Hlavka *et al.* 2012, Young and Vaughan 2009). Therefore, the algorithms for these lidars rely on an accurate global parameterization of the lidar ratio in order to resolve extinction and backscatter coefficients for ice and liquid water clouds (Winker *et al.* 2009). For a cirrus cloud with a COD greater than 0.10, a 30 percent error in the assumed lidar ratio can lead to an error in the extinction retrieval from elastic backscatter lidar systems of about 50 percent (Young *et al*. 2013).

The backscatter color ratio is defined as the ratio of 1064 nm particulate backscatter to 532 nm particulate backscatter and provides information on the spectral dependence of scattering properties of an atmospheric layer. Previous studies of the color ratio have found values that range from 0.50 to 1.4 for cirrus clouds, with lower color ratios representing particle sizes smaller than the geometric optics regime (Del Guasta and Niranjan, 2001; Vaughan *et al.* 2010). Vaughan *et al.* (2010) examined cirrus color ratios using CPL data and found that the color ratio, corrected for aerosol loading in the CPL calibration region, varied between 0.76 and 1.26 with higher values in the tropics. Correlations between lidar measurements of cirrus optical properties and particle microphysical properties have been evaluated in the past (Del Guasta and Niranjan, 2001, Reichardt *et al*. 2002), but not using recent airborne and space-based measurements. More research is needed to improve our understanding of the relationship between cirrus optical properties and cloud generation mechanism, which consequently should improve the accuracy of cloud radiative forcing estimations from space-based instruments and cloud models.

## 1.2 Lidar Measurements of Cirrus Clouds

There are several different types of lidar systems used to measure cirrus properties and motion. Cloud-aerosol lidars measure the elastic backscatter from atmospheric molecules and particles to resolve vertical profiles of spatial and optical properties of clouds and aerosols. The two most common cloud-aerosol elastic backscatter lidar techniques are standard backscatter lidars and high spectral resolution lidars (HSRL). The data provided by these lidar systems are essential to investigations of cirrus properties for numerous reasons. The vertical structure of the cirrus resolved by lidar systems cannot be accurately obtained from passive satellite or passive airborne sensors. Furthermore, thin cirrus optical depths are often below the detection limits of millimeter cloud radar systems (Comstock *et al.* 2002). In situ instruments can provide critical measurements of cirrus microphysical properties, however, they do not provide vertical profiles of these measurements unless the aircraft altitude changes and can alter the physical properties of the cirrus particles (Jensen *et al*. 2009; Zhao *et al.* 2011). Information obtained from cloud-aerosol lidar systems can improve knowledge of cirrus properties, which in turn advance cirrus parameterizations and reduce the uncertainties introduced in GCMs.

Standard elastic backscatter lidars are the least complex and most common lidar systems used to study vertical profiles of thin cirrus properties. Ground-based and airborne systems have been used in numerous field campaigns over the past few decades. For example, the CPL is an elastic backscatter lidar system operating at 1064, 532, and 355 nm. Depolarization is resolved using the 1064 nm channel and cloud optical properties are retrieved using the 1064 and 532 nm channels (McGill *et al.* 2003). The vertical resolution of the CPL measurements is fixed at 30 m (McGill *et al.* 2002). CPL points near-nadir, but not exactly nadir since the ER-2 flies with a pitch of 2 degrees and aircraft wing motion can also add an additional 1 degree to the off-nadir angle. CPL data products have a wide-range of applications including the analysis of cirrus optical properties (McGill *et al.* 2004; Bucholtz *et al.* 2010; Davis *et al.* 2010) and aerosol transport (McGill *et al.* 2003; Nowottnick *et al.* 2011). The routine CPL data processing algorithms retrieve the physical and optical properties of cloud and aerosol layers. There are three primary processing algorithms used to derive physical and optical properties in the CPL data: backscatter, layer detection, and optical properties. McGill *et al.* (2007) describe the overall CPL science data processing architecture and backscatter algorithms, while Yorks *et al.* (2011b) and Hlavka *et al.* (2012) explain the algorithms for layer detection and optical properties, respectively.

Standard backscatter lidar systems, such as CPL and CALIOP, fundamentally measure vertical profiles of attenuated total backscatter. This total signal is composed of two separate signals, one from particle (Mie) scattering and the other from molecular (Rayleigh) scattering. There have been many methods developed to retrieve the particle extinction and particle backscatter coefficients from a cloud-aerosol lidar return signal.

One technique is an inversion using standard backscatter lidar data developed by Fernald *et al.* (1972) and Klett (1981; 1985). The Klett or Fernald method makes it possible to solve the standard lidar equation by assuming a lidar ratio is known and constant throughout a particulate layer. This assumption reduces the number of unknowns in the system to one. This method, shown in section 2.3.1, is commonly used to retrieve particle extinction and backscatter coefficients from standard backscatter lidars such as CALIOP (Young and Vaughan 2009) and CPL (McGill *et al.* 2002). The lidar ratio is highly dependent on the optical and microphysical properties of atmospheric layer being measured. As discussed in section 1.1, the variability in the lidar ratio can create large uncertainties in the retrieval of the particle extinction and backscatter coefficients.

Another method for retrieving the particle backscatter and extinction coefficients from a lidar signal is a HSRL, based on the use of two measured profiles instead of only one. This method was first theorized by Fiocco (1971) to distinguish the contributions of the molecular and particle scattering using the difference in Doppler broadening of light backscattered by the two components. Air molecules experience significant thermal velocities as a result of their small size, and thus the scattering from air molecules is broadened by about 2 GHz ($10^{-3}$ nm) at visible wavelengths (Young 1981). In contrast, particle backscatter is hardly broadened (about 30 MHz or $10^{-5}$ nm) as a consequence of the relatively slow thermal motion of atmospheric cloud and aerosol particles. The narrow spectral shape of particle backscatter can be characterized by the small frequency distribution of lasers (Esselborn *et al.* 2008). The HSRL technique utilizes the difference in spectral distribution of the molecular (red) and particle (blue) backscattered signals, as shown in Figure 1.2a. High spectral resolution optical filters are required to separate the particle contribution from the molecular backscatter and resolve particle extinction and backscatter coefficients independently with no assumption about the lidar ratio required. In addition, the center frequencies of the transmitting laser and the optical filter must be aligned and the laser broadening must be narrower than the filter width (Eloranta 2005). These requirements make HSRLs more difficult to implement than standard backscatter lidars.

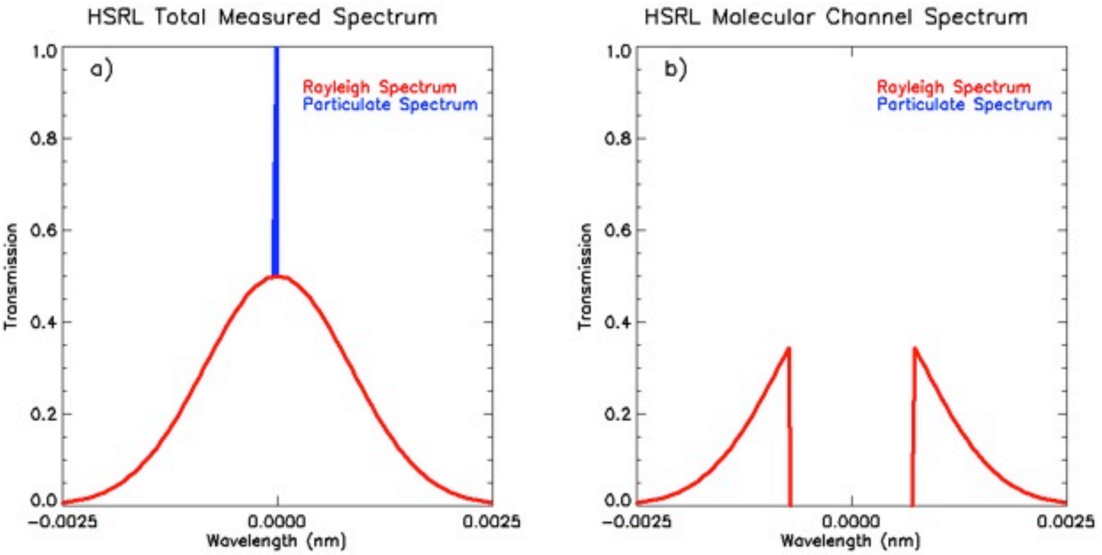

**Figure 1.2**. The Rayleigh (red) and particulate (blue) broadening for atmospheric backscattered light at a given laser wavelength (a), which is typically measured by the HSRL total backscatter channel. The typical HSRL instrument also has a molecular channel, which employs an absorption filter to block out the center of the scattering spectrum and measures the wings of the broad Rayleigh spectrum (b).

Only a few HSRL instruments have been successfully developed and operated to measure cloud and aerosol optical properties from ground or aircraft platforms. These HSRL systems employ either Fabry-Perot interferometers (Shipley *et al*. 1983; Grund *et al*. 1991) or absorption filters to differentiate particle scattering from molecular scattering (Piironen and Eloranta 1994). The most common HSRL technique is the use of molecular absorption filters in the receiver system of the instrument, where the received atmospheric signal is split into two detector channels to discriminate between particle and molecular backscatter. The total backscatter channel measures the full spectrum shown in Figure 1.2a, which includes both the particulate and molecular components  similar to a standard backscatter lidar, with no sensitivity to the spectral broadening of the two components (Hair *et al.* 2008).  The molecular channel contains the absorption filter, which rejects the particle backscatter and transmits the wings of the Doppler broadened molecular spectrum as a total molecular signal (Figure 1.2b).  The transmitter consists of an injection-seeded laser that operates on a single longitudinal mode to ensure that the laser linewidth is narrower than the molecular spectrum but wider than the particle broadening (Hair *et al.* 2008).

Researchers at Colorado State University developed the first HSRL using the absorption filter technique, which employed heated absorption cells containing Barium vapor (Alvarez *et al.* 1990; She *et al.* 1992). A simpler concept was pioneered at the University of Wisconsin (Piironen and Eloranta, 1994) using a molecular iodine absorption cell to replace the Barium cell.  This method has several advantages over the Barium cell concept.  The iodine vapor filters exhibit more robust rejection of aerosol backscatter and less sensitivity to optical alignment.  Furthermore, iodine vapor filters operate at much lower temperatures (25 to 100 C) compared to Barium cells (Esselborn *et al.* 2008).  Most notably, 532 nm frequency-doubled Nd:YAG lasers can be employed because iodine has several absorption lines within the thermal tuning range of these lasers.  This is advantageous because Nd:YAG lasers are readily available and can be injection-seeded to generate a narrow spectral linewidth and lock the laser to the same wavelength as the specified iodine absorption line (Eloranta 2005).  Consequently, the iodine filter method is the preferred method for HSRL systems to date.  Recently airborne HSRL systems that employ iodine filters have been implemented and demonstrated on the NASA King Air (B-200) research aircraft (Hair *et al.* 2008) and the German

Aerospace Center Falcon research aircraft (Esselborn *et al.* 2008). HSRL data have been used to independently resolve the extinction coefficient for aerosol layers over Mexico during the MILAGRO campaign (Rodgers *et al.* 2009). However, a caveat of the iodine filter technique is that the spectral broadening of the particle backscatter is not measured but inferred from the total and molecular backscatter. The backscattered signal also contains additional information imparted in the scattering process, such as the Doppler shift caused by the mean velocity of the particle.

Doppler wind lidars use the frequency shift imparted on atmospheric particles and molecules to determine the vertical profiles of the horizontal wind speed and direction. The two most common types of pulsed Doppler wind lidar systems are coherent (heterodyne) detection and direct (incoherent) detection. Coherent Doppler lidars use a heterodyning technique that mixes a pulsed lidar signal with a second laser signal to produce a beat frequency related to the Doppler shift. The second continuous laser beam is usually a local oscillator offset in frequency (Hall *et al.* 1984; Huffaker *et al.* 1984). Coherent systems operate at wavelengths in the IR or near-IR region and have been in use for many years (Huffaker and Hardesty 1996). Direct-detection lidars directly measure the frequency shift of the return signal using a high spectral resolution filter, such as a Fabry-Perot interferometer, and operate at shorter wavelengths than coherent systems (Benedetti-Michelangeli *et al.* 1972; Chanin *et al.* 1989; Abreu *et al.* 1992; Gentry and Korb 1994). The laser wavelength of a Doppler wind lidar can vary by the type of detection method used. Since the wind velocity error is related to the sharpness of the spectral return, most direct-detection Doppler lidar systems use the particle scattering to determine the Doppler shift.

Coherent Doppler lidar systems were the first to demonstrate accurate and dependable wind measurements. In heterodyne detection, the return signal of the pulsed laser beam is mixed with the return signal from a local optical oscillator (LO). The pulsed laser is typically seeded for high frequency stability while the LO laser is continuous-wave. The mixed signal contains both the sum and difference frequencies of the two signals. However, only the difference frequency (i.e. beat signal) is a low enough frequency to be resolved accurately by the detector (Hall et al. 1984, Huffaker et al. 1984). The beat signal is measured for the outgoing laser pulse and the LO laser beam ($f_{LO} \pm f_0$), as well as the Doppler shifted backscatter signal and LO laser ($f_{LO} \pm f_0 + \Delta f$). Two separate detectors then measure these two beat signals (Hall et al. 1984, Huffaker et al. 1984). The main assets of coherent lidar systems are the high tolerance of background light and insensitivity to thermal stability (Werner 2005).

The Fabry-Perot interferometer, developed in 1897 by Charles Fabry and Alfred Perot, has been employed for many applications including spectroscopy and direct-detection Doppler lidar systems (Hernandez 1986; Vaughan 1989). The standard Fabry-Perot interferometer is comprised of two optically flat plates with highly reflective dielectric coating on the inside surfaces. These plates are separated by a distance (d) using three posts. In the cases where d is held constant, the Fabry-Perot interferometer is also known as an etalon and will be referred to as such throughout this study. Figure 1.3 shows a schematic of the optical process known as multiple beam interference (McGill 1996). Light entering the etalon is reflected and transmitted many times between the plates, and exits through both the front and rear of the etalon. The light that exits through the front is typically referred to as the reflected light (red). Light transmitted exits through the rear of the etalon (green) and is a function of the plate spacing, as well as the incident angle and wavelength.

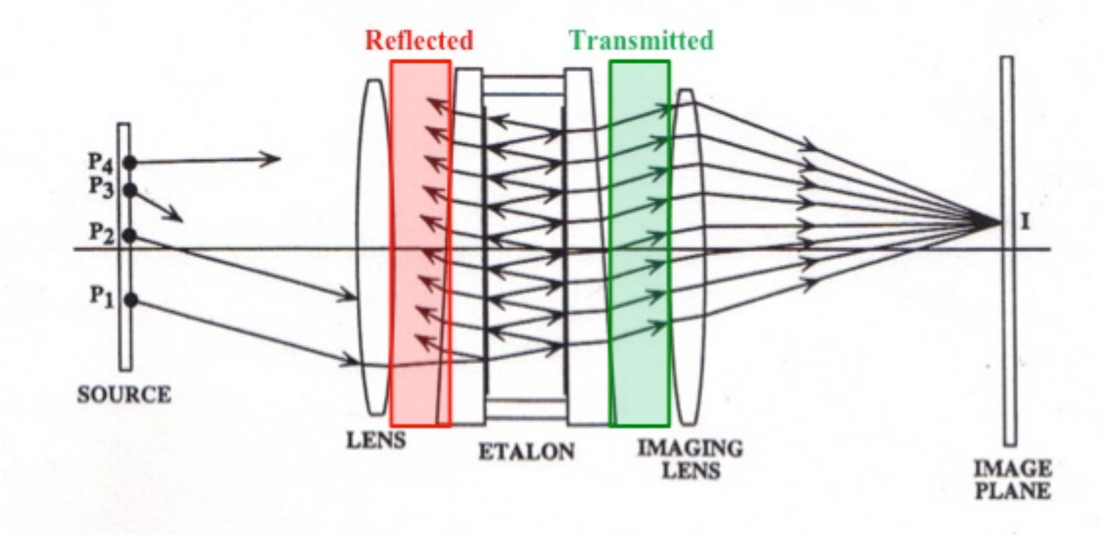

**Figure 1.3**. A schematic of the etalon optical process known as multiple beam interference adapted from McGill 1996. Source light enters the etalon and can be reflected (red) or transmitted (green). For direct-detection Doppler lidars, the transmitted light can be focused using an imaging lens and measured to determine the Doppler shift.

The constructive and destructive interference (waves traveling in-phase and out-of-phase with one another, respectively) of the transmitted light rays creates the Fabry-Perot fringe pattern (Figure 1.4). Figure 1.3 explains the origin of the fringe pattern (McGill 1996). A single ray of light emitted from an incoherent source (P1) will experience many reflections as it travels through the etalon. The transmitted rays (green) are collected by the imaging lens and focused onto the plane at point I, since these rays are from the same source point (coherent). At point I, constructive interference occurs and produces a white ring in the fringe pattern. Light rays emitted from a different source (incoherent) parallel to P1 (i.e. P2) are also focused onto the plane at point I. However, no interference occurs between these rays so their individual interference intensities add at the image plane. If other rays are emitted from different sources not parallel to P1 (i.e. P3 and P4), both constructive and destructive interference with rays from P1 and P2 occur. The constructive interference results in additional white rings, with each angle corresponding to a unique radius. Similarly, the destructive interference creates black rings. Assuming the two etalon plates have equal reflectivity, the transmission function of an etalon is:

$$T(M) = \left(1 - \frac{L}{1-R}\right)^2 \left(\frac{1-R}{1+R}\right)\left(1 + 2\sum_{n=1}^{\infty} R^n \cos(2\pi n M)\right) \qquad \text{Eq. 1.1}$$

where R is the reflectivity of the etalon plates, L is the loss through absorption and scattering by the dielectric coatings, and M is the order of interference (McGill 1996).

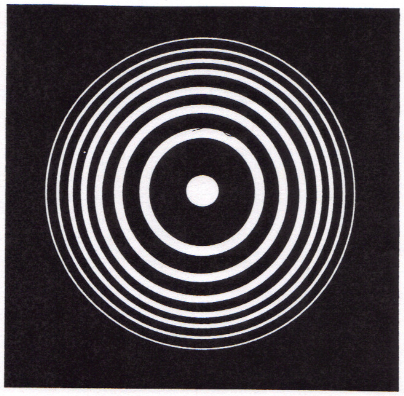

**Figure 1.4**. An image of the fringe pattern that results from the interference patterns of light transmitted through an etalon.

Direct-detection lidar systems have evolved over the last few decades as a proven technique for measuring the Doppler shift of atmospheric constituents. There are three main direct-detection methods, all of which use a narrow bandpass filter or etalon instead of a second laser. The earliest method, known as the edge technique (EDG), uses a sharply sloping atomic filter or etalon to measure the change in the signal transmission caused by the Doppler shift of the laser wavelength by converting the frequency shift into an amplitude signal (Bloom *et al.* 1991; Korb *et al.* 1992; Gentry and Korb 1994). However when the return signal is a combination of particle and molecular backscatter, an unambiguous retrieval of the Doppler shift cannot be achieved using this single-filter technique. A variation of the EDG technique was developed using two filters known as the double-edge technique (DEDG). The DEDG technique was first demonstrated using molecular backscatter by Garnier and Chanin (1992) and using aerosol backscatter by Korb *et al.* (1998), and is shown in Figure 1.5a for a molecular system. The DEDG aerosol technique usually employs two etalons symmetrically located about the laser frequency with the laser line positioned at the point of half the peak (McGill and Spinhirne 1998). The return signal is divided evenly into each etalon and measured separately on single element detectors. The transmitted signal of one etalon increases while simultaneously decreasing on the second etalon (McGill and Spinhirne 1998). The Doppler shift is then determined from the changes in the transmitted signal of the two etalons. Two recent DEDG systems include the Doppler wind lidar of the Observatoire de Haute Provence (OHP) at Saint-Jean-l'Observatoire, France (Souprayen *et al.* 1999) and the NASA Goddard Lidar Observatory for Winds (GLOW) molecular system (Gentry *et al.* 2000). A third direct-detection method, termed multichannel (MC) by McGill and Spinhirne (1998), measures the Doppler shift of atmospheric particles (such as cirrus cloud particles) by imaging the etalon fringe pattern onto a multiple element detector (Abreu *et al.* 1992; Fischer *et al.* 1995; McGill *et al.* 1997a). This method requires the etalon transmission function to be aligned with the laser wavelength, as demonstrated in Figure 1.5b.

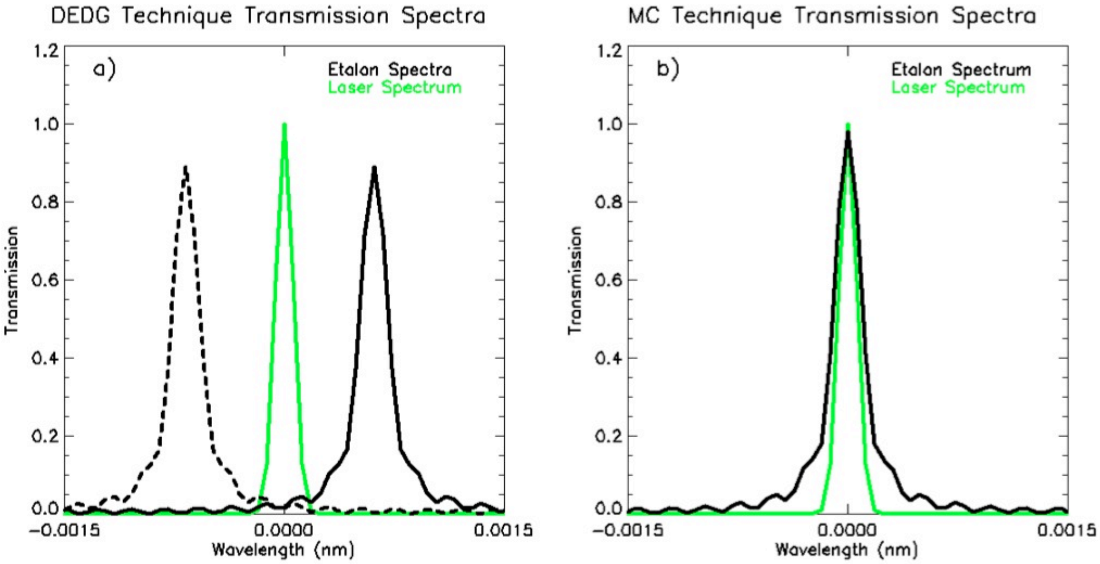

**Figure 1.5**. The DEDG technique (a) employs two etalons with peak transmission (black) symmetrically located about the laser center linewidth (green), while the MC technique (b) uses one etalon with peak transmission in alignment with the laser center linewidth.

## 1.3 Objectives of This Study

The Airborne Cloud-Aerosol Transport System (ACATS) is a multi-channel Doppler lidar system recently developed at NASA Goddard Space Flight Center (GSFC). A unique aspect of the multi-channel Doppler lidar concept such as ACATS is that it is also, by its very nature, a HSRL. Both the particulate and molecular scattered signal can be directly and unambiguously measured, allowing for direct retrievals of particle extinction. ACATS is therefore capable of simultaneously resolving the backscatter/extinction properties and motion of a particle from a high altitude aircraft. The instrument has flown on the NASA ER-2 during test flights over California in June 2012 and as part of the Wallops Airborne Vegetation Experiment (WAVE) in September 2012. The CPL instrument also participated in the WAVE project, as well as nearly a dozen other field campaigns in the past decade. The objectives of this study are:

- Develop and demonstrate a new technique for HSRL retrievals of cloud and aerosol optical properties
- Evaluate this technique using coincident CPL data
- Investigate the relationship between cirrus optical properties and dynamic formation mechanism using ten years of data from the CPL instrument

A description of the ACATS instrument design is provided in Chapter 2, which includes details of the optical and mechanical components of the subsystems as well as the software that autonomously controls the instrument operation. I advance the effort of McGill *et al*. 1997a and McGill *et al*. 1997b by demonstrating the retrieval algorithms for HSRL direct measurements of cloud and aerosol optical properties (i.e. extinction) that have direct application to future spaceborne missions such as the Cloud-Aerosol Transport System (CATS) to be installed on the International Space Station (ISS). I also present initial ACATS HSRL results and data products from the WAVE campaign, as well as a modeling study demonstrating the sensitivity of the ACATS HSRL retrieval errors to the instrument calibration. The direct extinction and particle wind velocity retrieved from the ACATS data can be used for science applications such as dust or smoke transport and convective outflow in anvil cirrus clouds.

The WAVE project provides an excellent opportunity to compare ACATS 532 nm data products to coincident CPL 532 nm measurements and assess biases in the instrument and retrieval algorithms, discussed in Chapter 3. These flights, which represent the first science flights for the ACATS instrument, targeted specific land and vegetation surfaces with a scientific objective of simulating Ice, Cloud and land Elevation Satellite 2 (ICESat-2) data using the Multiple Altimeter Beam Experimental Lidar

(MABEL; McGill *et al.* 2013). ACATS and CPL were both payloads on a total of 13 flights during the WAVE campaign, which include observations of thin cirrus clouds and smoke layers. CPL has participated in over a dozen field campaigns during the last decade and is the preferred cirrus validation tool for CALIPSO satellite retrievals (McGill *et al.* 2007; Yorks *et al.* 2011b; Hlavka *et al.* 2012). Given this strong heritage, CPL measurements are used to validate and evaluate ACATS cloud and aerosol retrievals for both the standard and HSRL methods through a series of case studies as well as statistics of cirrus lidar ratios. Such a comparison also demonstrates the effectiveness of the HSRL method in reducing the uncertainties of extinction retrievals from lidar systems.

In the final component of this study, I examine the relationship between cirrus properties and dynamic formation mechanism. CPL and ACATS are preferred instruments to study cirrus compared to space-based and ground-based lidar systems. The relatively large footprint size and orbital heights of current space-based lidars such as CALIOP can produce a signal-to-noise ratio (SNR) ten times lower and multiple scattering effects 40 percent higher compared to airborne lidar systems (Yorks *et al.* 2011b). The typical cruise altitude of the ER-2 (20 km) and relatively weak aerosol loading of the upper troposphere yields less range-to-target and lidar beam attenuation for CPL and ACATS compared to ground-based lidar systems. Over 700 hours of CPL data are used to explore the following science questions in the final section of this dissertation:

- What are the typical values of cirrus clouds properties for clouds formed in the mid-latitudes, especially cirrus formed as a result of synoptic-scale uplift?
- How do properties of synoptically-generated cirrus compare to those formed due to the rapid vertical motions of convection in the tropics?

- Are these relationships between cirrus optical properties and generation mechanism observed on a global scale?

Ultimately this study will provide statistics about how cirrus properties vary by region or dynamic generation mechanism that can be used as part of a larger global climatology of cirrus clouds to improve parameterizations in global climate models and satellite retrievals.

# Chapter 2: The Airborne Cloud-Aerosol Transport System (ACATS)

In this chapter, I provide a description of the ACATS instrument design, including details of the telescope and receiver subsystems. The determination of the ACATS calibration parameters is outlined, as well as the standard backscatter products computed similar to CPL and CALIPSO. I also demonstrate a new technique for directly retrieving HSRL cloud and aerosol products (i.e. extinction) from a multi-channel direct-detection Doppler wind lidar, different from the iodine-filter HSRL technique used in the past. Finally, I present initial ACATS HSRL results and data products from the WAVE campaign, as well as a modeling study demonstrating the sensitivity of the ACATS HSRL retrieval errors to the instrument calibration. The ACATS retrieval algorithms and data products have direct application to the future ISS CATS mission. The information contained in this chapter has been submitted to the *Journal of Atmospheric and Oceanic Technology* and is currently under the peer-review process (Yorks *et al.* 2014a)

## 2.1 ACATS Method and Instrument Description

The ACATS instrument is a multi-channel (MC) Doppler lidar system built for use on the NASA ER-2 high altitude aircraft. The MC technique passes the returned atmospheric backscatter through a single etalon and divides the transmitted signal into several channels (wavelength intervals), measured simultaneously and independently (Figure 2.1). The resulting aerosol spectral distribution is then compared to the outgoing laser distribution to infer the Doppler shift, as demonstrated in Figure 2.2a. Subsequent measurements of the atmospheric scattered light will reveal a wavelength offset proportional to the Doppler shift and directly related to the velocity of the scattering particles (Figure 2.2b). The basic concept is summarized in Figures 2.1 and 2.2. The MC method for determining horizontal wind velocity was demonstrated using the ground-based University of Michigan Doppler lidar (McGill *et al.* 1997a; McGill *et al.* 1997b).

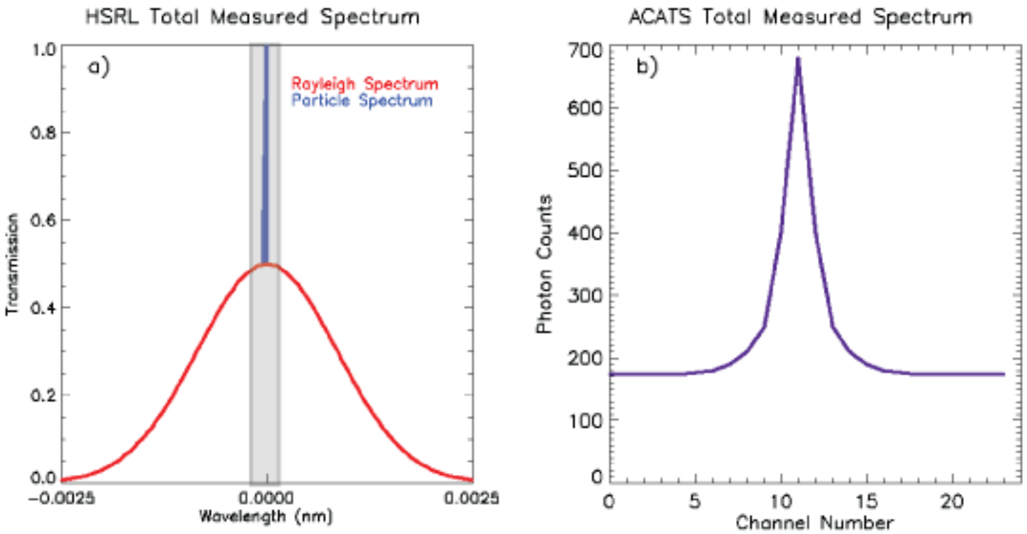

**Figure 2.1**. The ACATS method images the grey shaded area of the returned atmospheric signal (a) onto a 24 channel array detector, which measures the photon counts at each wavelength interval independently as a total backscattered signal (b).

A unique aspect of the MC Doppler lidar concept such as ACATS is that it is also a HSRL. Both the particle and molecular scattered signal can be directly and unambiguously measured since the broad Rayleigh-scattered spectrum is imaged as a nearly flat background, illustrated in Figure 2.2c. The integral of the aerosol-scattered spectrum (Figure 2.2d) is analogous to the measurement from the typical absorption filter HSRL technique, providing a separation between the particulate and molecular components of the backscattered signal. While previous ground-based MC systems have been built and operated (Benedetti-Michelangeli *et al.* 1972; Abreu *et al.* 1992; McGill *et al.* 1997a), there has been no airborne demonstration of the technique and the method has not been used to derive HSRL cloud and aerosol properties.

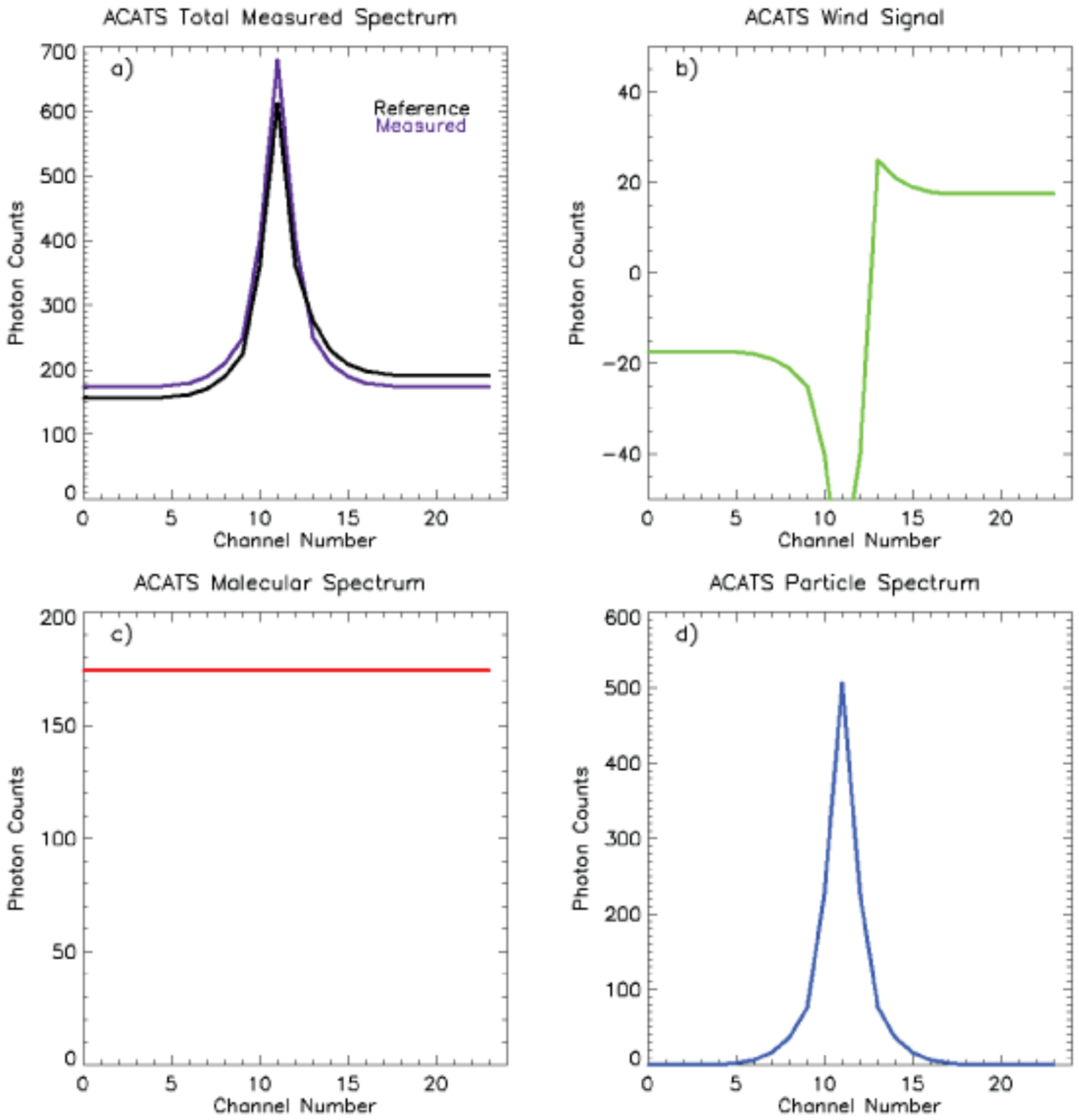

**Figure 2.2**. The Doppler shifted atmospheric signal (purple) measured by ACATS is compared to an unshifted reference spectrum (a), which yields the Doppler wind signal (b) of the ACATS measurement. The broad Rayleigh scattered spectrum (c) is measured by ACATS as a nearly flat background of the total atmospheric return signal, resulting in a sharp particle spectrum (d) that is directly measured.

The ACATS instrument is composed of three main subsystems; laser transmitter, telescope, and receiver optics. A list of the ACATS instrument parameters is provided in Table 2.1. A picture of the ACATS instrument fully assembled, with the receiver and telescope subsystems, is shown in Figure 2.3. The instrument also includes a heating/cooling loop to provide stable thermal operation of the laser.

**Table 2.1**. Primary system parameters for ACATS lidar.

| Parameter | Value |
|---|---|
| Laser Type | Nd: YAG, seeded |
| Wavelength | 532 nm |
| Laser Repetition Rate | 250 Hz |
| Laser Output Energy | ~10 mJ/pulse |
| Telescope Diameter | 8 inches |
| Viewing Angle | 45 degrees |
| Telescope FOV | 350 μradians (full angle) |
| Bandpass Filter | 150 pm FWHH |
| Etalon Spacing | 10 cm |
| Etalon Reflectivity | 85% |
| Orders Imaged | 1.2 |
| Detector Channels | 24 |
| Raw Range Resolution | 30 m |
| Horizontal Resolution | 1 sec (~200 m) |
| Platform Speed | ~200 $ms^{-1}$ |
| Platform Altitude | ~ 20 km (65,000 ft) |

The frequency characteristics of pulsed lasers have recently been advanced due to the development of direct detection Doppler lidars and HSRLs. These techniques impose further requirements compared to standard backscatter lidars, such as lasers that are single frequency on a single pulse basis and more stable in time (central frequency drift of less than 1 MHz per minute). An injection-seeded, pulsed Nd:YAG laser was developed for the TWiLiTE instrument (Hovis *et al.* 2004) that achieves these frequency characteristics. This laser was later replicated for the ACATS instrument and provides a narrow wavelength distribution suitable for resolving the small frequency shifts due to the Doppler effect. The laser operates at an output power of about 10 mJ per pulse and repetition rate of 250 Hz at 532 nm and is designed for use in the low-pressure environment of high-altitude aircraft.

**Figure 2.3**. The fully assembled ACATS instrument (a) includes the receiver tube covered in insulation (left) and a pressurized telescope dome (right). A picture of the inside of the receiver subsystem (b) shows the etalon (silver device in the middle), the 24-channel array detector, and circle-to-point converter. The inside of the telescope subsystem (c) contains a motor to rotate the telescope and a HOE.

The ACATS telescope employs a rotating holographic optic element (HOE) to fit the small volume envelope of the ER-2 superpod and to enable vector wind measurements, which requires more than one viewing direction (Figure 2.3c). The telescope system is set for 45 degree off-nadir viewing and rotates on a bearing to permit step-stare operation. The number of scan angles (up to 8) and dwell time at each scan angle is controlled by software and can be modified before flight. The HOE focuses the return signal onto the fiber and allows for a resting place for mirrors that direct the outgoing laser light out of the telescope at 45 degrees. A schematic of the optical design is presented in Figure 2.4. As the telescope rotates, the optical alignment changes and may lead to a loss in return signal if not corrected. A procedure that steps the telescope position using piezoelectric actuators and scans for the largest return signal is run during flight to determine the optical alignment at each scan position. The 8-inch diameter telescope is also fiber-coupled to the receiver subsystem to provide greatest flexibility.

The primary difference between a lidar system capable of only measuring total backscatter intensity (e.g., CALIOP or CPL) and an instrument that directly measures the particle extinction and Doppler shift, such as ACATS, lies in the receiver subsystem (Figures 2.3b; 2.4). The heart of the ACATS receiver system is an etalon that provides the spectral resolution needed for the HSRL measurement and also to resolve the Doppler shift inherent in the backscattered signal. Backscattered light collected by the telescope is passed through the etalon and an image of the etalon fringe pattern is created. A bandpass filter is used in tandem with the etalon to reject background sunlight, permitting daytime operation. The optical gap of the etalon is 10 cm with an operational diameter of 35 mm and plate reflectivity of 85%. As with any MC system, it is critical to maintain the symmetry and shape of the etalon fringe pattern to avoid uncertainty in the measurement. A digital etalon controller was developed by Michigan Aerospace Corporation in which piezoelectric actuators control the etalon electronics to position and maintain the plate parallelism. Considerable work was performed to create autonomous flight software that maintains the etalon alignment over the entirety of an ER-2 flight. The signal transmitted by the etalon is then passed to the detector subsystem.

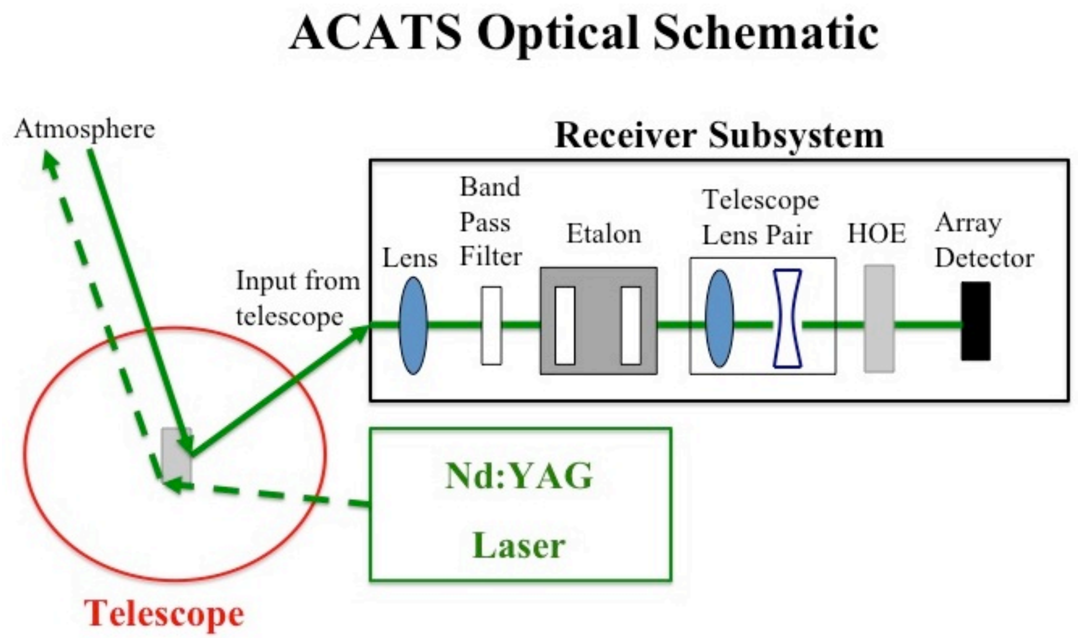

**Figure 2.4**. The ACATS optical schematic shows the outgoing 532 nm laser light (dashed green), originating from the Nd:YAG laser, directed out of the telescope by a mirror. The return signal (solid green) is passed through the telescope and into the receiver subsystem using an optical fiber, where it is transmitted through optical lenses and filters, including the etalon. The circle-to-point converter in the receiver box is labeled as HOE.

A holographic circle-to-point converter optic (McGill *et al.* 1997c; McGill and Rallison 2001) is placed in the focal plane to provide the spectral detection. The circle-to-point converter simplifies hardware requirements, improves efficiency of measuring the spectral content in the fringe pattern, and allows ACATS to utilize photon-counting detection. The holographic optic is coupled to a Hamamatsu H7260 linear array detector, which utilizes back-end electronics developed by Sigma Space Corporation to permit photon-counting detection at count rates in excess of 50 MHz. The ACATS receiver images ~1.2 orders over 24 detector channels. The ACATS etalon parameters result in a measurement dynamic range of ~400 ms$^{-1}$, more than sufficient for typical atmospheric motions.

An autonomous multi-channel data system is the final component of the instrument and was based entirely on work completed by Sigma Space Corporation in support of the CPL, UAV-CPL, and TWiLiTE lidars. The basis for the data system, the Advanced MultiChannel Scaler (AMCS) card, was first applied in the ER-2 CPL instrument. The data acquisition software is included in the data system and has its heritage in the CPL and UAV-CPL instruments. An important aspect of the ACATS data system, as developed for CPL and UAV-CPL, is the ability to downlink data in real-time from the aircraft using the onboard air and navigation payload server. The data system also incorporates a Novatel model OEMV-3RT2i GPS receiver and OEM-IMU-H58 inertial unit to enable accurate correction for platform motion. The Novatel system provides greater than 20 Hz update rates with 2 cm $s^{-1}$ velocity accuracy. The raw ACATS data file consists of photon counts at each horizontal record (1 sec), range bin (30 m) and detector channel, which is then converted to atmospheric parameters such as backscatter and extinction coefficients.

There are several differences between HSRL systems that use the iodine filter technique and the multichannel etalon technique used in the ACATS instrument. ACATS directly measures the *spectral broadening* of the particulate and molecular backscatter using the etalon to filter out all backscattered light with the exception of a narrow wavelength interval (1.5 picometers for ACATS) that contains the particulate spectrum (Figure 2.1a). This signal is imaged onto a 24-channel linear array detector (Figure 2.1b). The iodine filter technique measures the total backscatter (molecular plus particulate signal) in one detector channel irrespective of spectral broadening, similar to a standard backscatter lidar, and also measures the molecular backscatter in another detector channel using the iodine absorption filter to remove the entire particulate signal. Thus the iodine absorption filter technique, unlike ACATS, does not measure the particulate backscatter directly but instead infers the particulate backscatter from the total and molecular components. Also, ACATS measures the *spectral broadening* of the backscattered signal, where as the iodine absorption filter technique does not. Finally, the iodine absorption filter technique works only at the laser frequency doubled and tripled wavelengths of 532 and 355 nm. Since iodine does not have an absorption line near 1064 nm, the technique cannot be used at this wavelength. By contrast, the ACATS HSRL method can be employed at all three laser wavelengths.

## 2.2 ACATS Calibration Procedures

Several calibration parameters are required to accurately retrieve the wind velocity, aerosol and molecular backscatter from the ACATS data. These include normalization constants, instrument defect parameter, and detector nonlinearity. The illumination and sensitivity of the detector channels are not the same, necessitating normalization constants to compensate. The detector normalization coefficients are determined using a white-light source to illuminate the telescope while the receiving optics remains unchanged. These normalization constants describe the relative response of the detector to broad bandwidth illumination.

The alignment of the circle-to-point converter (HOE) and Fabry-Perot fringe pattern also must be characterized. Each ring in the circle-to-point converter represents a detector channel. Since the circle-to-point converter and etalon are manufactured separately, a ring can have a dissimilar centricity and diameter compared to the fringe pattern projected onto it, resulting in signal loss to the corresponding detector channel. To complicate matters, this loss of signal can vary in each channel. In the case of ACATS the outer rings (higher detector channels) of the circle-to-point converter are not perfectly concentric with the fringe pattern, requiring normalization constants to compensate. The normalization coefficients are determined using the peak transmission of the etalon calibration data in each channel. Assuming perfect alignment in all channels, the peak transmission will remain constant as the signal is stepped through all detector channels. Thus, the ACATS channel with the highest transmission represents the best alignment, allowing all other channels to be normalized to the "best aligned" channel. These normalization constants describe the relative signal loss of the detector channel due to alignment imperfections. The most current ACATS detector and HOE normalization coefficients from 26 April 2012 are shown in Table 2.2.

To characterize the instrument defect parameter, I developed an etalon calibration procedure for ACATS similar to the one outlined in McGill *et al.* (1997a). The etalon transmission equation (Eq. 1.1) can be rewritten and expressed as a function of detector channel (j) as demonstrated by McGill (1996):

$$T(\Delta\lambda, j) = \sum_{n=0}^{\infty} A_n \cos\left[2\pi n\left(\frac{\Delta\lambda}{\Delta\lambda_{FSR}} + \frac{j}{N_{FSR}}\right)\right]\sin c\left(\frac{n}{N_{FSR}}\right) \qquad \text{Eq. 2.1}$$

where $\Delta\lambda_{FSR}$ is the free spectral range and is defined as the change in wavelength necessary to change the order of interference by one. The free spectral range can also be represented by the number of channels necessary to change the order of interference by one, $N_{FSR}$. The function $A_n$ is defined as:

$$A_n = 2\left(1 - \frac{L}{1-R}\right)^2 \left(\frac{1-R}{1+R}\right) \mathrm{R}^n \, e^{-4\pi^2 n^2 \Delta d_D^2 \lambda_0^2} \qquad \text{Eq. 2.2}$$

where L is the loss of light due to absorption or scattering by the etalon plates and R is the plate reflectivity. The etalon transmission equation (Eq 2.1) is for an idealized etalon.

Several effects, such as plate bowing, microscopic plate defects, detector broadening, and off-axis aberrations, will broaden a real etalon function.

**Table 2.2**. ACATS detector and HOE normalization coefficients as of April 2012.

| **Channel** | **Detector** | **HOE** |
|---|---|---|
| 1 | 1.00 | 0.91 |
| 2 | 1.13 | 0.72 |
| 3 | 0.85 | 1.00 |
| 4 | 0.87 | 0.92 |
| 5 | 0.89 | 0.92 |
| 6 | 0.85 | 0.93 |
| 7 | 0.82 | 1.00 |
| 8 | 0.92 | 0.82 |
| 9 | 0.96 | 0.81 |
| 10 | 0.96 | 0.78 |
| 11 | 0.99 | 0.73 |
| 12 | 0.94 | 0.71 |
| 13 | 0.92 | 0.73 |
| 14 | 0.99 | 0.66 |
| 15 | 0.94 | 0.63 |
| 16 | 0.93 | 0.74 |
| 17 | 0.91 | 0.66 |
| 18 | 0.97 | 0.58 |
| 19 | 0.91 | 0.48 |
| 20 | 0.96 | 0.48 |
| 21 | 0.89 | 0.46 |
| 22 | 0.84 | 0.37 |
| 23 | 1.18 | 0.26 |
| 24 | 1.25 | 0.27 |

For the purpose of this study, it is sufficient to use an instrument defect parameter ($\Delta d_D$) to represent the etalon broadening effects and tune the etalon model so that it matches the measured ACATS spectral response. There are two important assumptions in determining the ACATS defect parameter. First, the defect parameter varies with detector channel to account for the variability of the etalon finesse with channel. It is also assumed that any broadening effects, and thus the etalon defect parameter, will follow a Gaussian distribution. The ACATS defect parameter is then determined by a calibration procedure similar to the one demonstrated in McGill *et al.* (1997a). Software runs a calibration procedure at least once per flight that varies the etalon gap using piezoelectric actuators. Varying the etalon gap moves the interference fringe pattern across the detector in 128 small steps, sampling nearly 3 orders (42 points per order). One can then determine the defect parameter for each channel by performing a least-squares fit to match the modeled etalon transmission function to the ACATS measured etalon response function using a similar technique to McGill *et al.* 1997a. The best fit (using a defect parameter of 27.0 nm) modeled (blue) and measured (red) ACATS etalon functions for channel 1 are shown in Figure 2.5 for ground test data collected on 29 April 2012. The light source used to measure the ACATS etalon response is the same laser used for atmospheric measurements. Additionally, the calibration technique automatically compensates for any uncertainty in computing the laser bandwidth, since the laser width follows a Gaussian distribution similar to the etalon broadening term.

The measured ACATS spectrum can become distorted due to detector dead time and must be compensated for. All lidar systems that employ photon-counting detection experience this effect, which is a limitation on the number of photons that can be counted in a given time interval. For ACATS, the large near-field return pushes the detector into a nonlinear counting region. The nonlinear effects for this type of detector can be quantified by a detector dead time coefficient. This coefficient represents the fact that only one photon event can be counted at once, and the detector system has a certain time delta, or dead time, before it can count another. A typical Hamamatsu linear array detector, such as the one employed in ACATS, has a discriminator dead time of 65 to 75 ns for a discriminator maximum count rate on the order of 15 MHz. To improve this performance, the ACATS Hamamatsu linear array detector is customized with a discriminator built by Sigma Space Corporation under Small Business Innovative Research (SBIR) funding that has a shorter discriminator dead time. This permits photon-counting detection at count rates in excess of 40 MHz before there is a 10% reduction in observed count rate. The ACATS detector rarely experiences count rates higher than 10 MHz in atmospheric bins below 17 km (assuming an ER-2 altitude greater than 19 km). Therefore, the detector dead time coefficient is less than 1.05 for 99.5% of atmospheric bins with the exception of the near-field return.

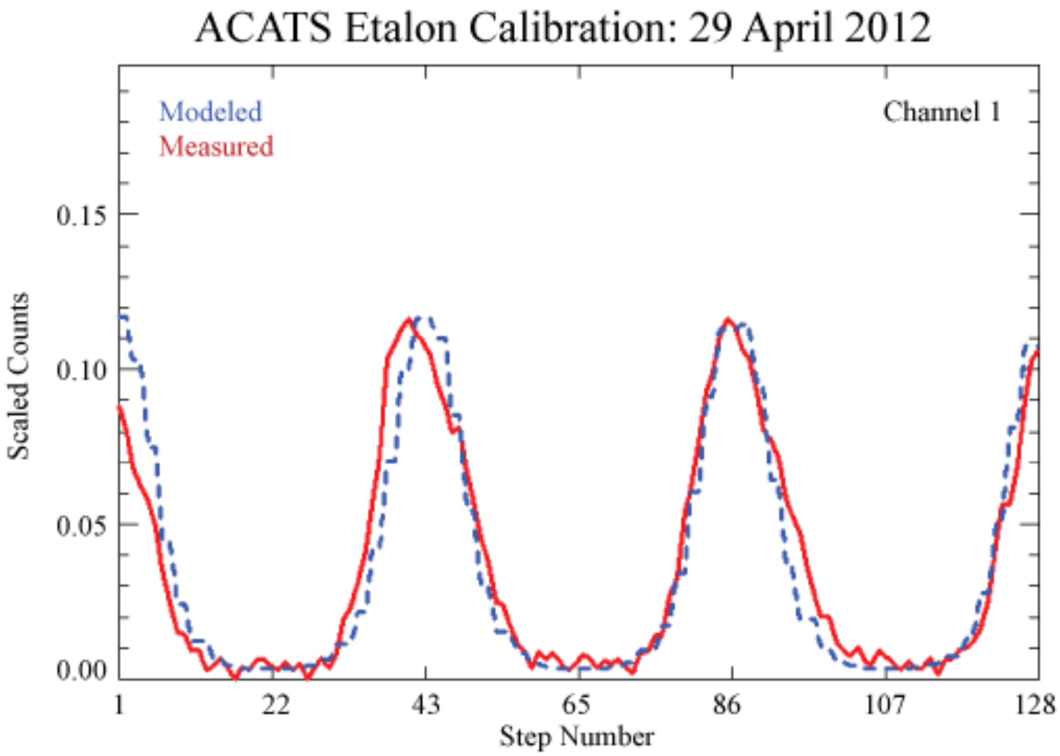

**Figure 2.5**. ACATS fitted (blue) and measured (red) etalon response function for Channel 1 on 29 April 2012. This least-square fitting technique is performed on all 24 channels to determine the ACATS defect parameter.

## 2.3 Development of ACATS Retrieval Algorithms

ACATS provides data products similar to other cloud-aerosol lidars, HSRL systems, and Doppler wind lidars. The system is currently set for 45 degree off-nadir viewing and the telescope rotates to allow for two orthogonal line-of-sight (LOS) wind measurements, which are then used to compute vertical profiles of horizontal wind velocity and direction within particulate layers. The ACATS retrieval algorithms and data products for the horizontal wind velocity will be presented in Chapter 5. This chapter focuses on two types of aerosol/cloud products available from ACATS data directly applicable to the ISS CATS instrument. Standard backscatter products are computed similar to CPL and CALIPSO (McGill *et al.* 2007). HSRL products are produced at courser resolutions (450 m vertical and 5 km horizontal), but include direct retrievals of attenuated particle backscatter, optical depth, as well as particle extinction and backscatter coefficients. These products are similar to those produced by other HSRL systems.

### *2.3.1 Development of Standard Backscatter Algorithms*

If the measured ACATS photon counts are summed over all channels as to neglect the spectral information provided by the etalon, vertical profiles of total backscatter can be retrieved from ACATS data. Similar to a standard backscatter lidar system (i.e. CALIOP), this total signal is composed of both the particle scattering and molecular scattering. The total signal is typically represented by the single scattering lidar equation, which describes the number of photon counts $N(r)$ detected from the range $r$ (Measures 1984; McGill 2003):

$$
\begin{aligned}
N(r) = {} & \left[\left(\frac{E_T\lambda}{hc}\right)\Delta r Q_E T_O O_A(r)\right]\left[\frac{A_T}{r^2}\right] \\
& \times\left[\left(P_P(\pi,r)\beta_P(r) + P_M(\pi,r)\beta_M(r)\right)e^{-2\int_0^r \sigma(r')dr'}\right] + B_D + B_S
\end{aligned}
\qquad \text{Eq. 2.3}
$$

Table 2.3 provides the definition and dimensions of the variables in the photon version of the lidar equation (the equation can also be written in terms of power transmitted and power received). It is important to note that this equation neglects the effects of multiple scattering, which can be significant for lidar systems with a large field-of-view (FOV) or space-based lidar systems (Winker 2003). Furthermore, the assumption that the laser pulse length is much less than the range bin length $\Delta r$ is invoked. For more complicated lidar systems, such as HSRLs or Doppler lidars, additional terms may be included in the equation.

The single scattering lidar equation as written here is grouped into three main contributions to the measured signal. The first group represents the instrument parameters, with the $E_T\lambda/hc$ term converting the laser energy into units of photon counts. The solid angle viewed by the receiver is denoted by the second set of brackets, $A_T / r^2$ (McGill 2003). The atmospheric physics is specified in the third bracket, which contains the phase function $P(\pi,r)$, volume total scattering coefficient $\beta(r)$, and volume total extinction coefficient $\sigma(r)$. This term can be simplified by combining the phase function and volume total scattering coefficient $P(\pi,r)*\beta(r)$ into the volume angular backscatter coefficient $\beta(\pi,r)$ with units of km $^{-1}$ sr $^{-1}$, composed of both molecular $\beta_M(\pi,r)$ and particle $\beta_P(\pi,r)$ components. The attenuation of the atmosphere represented by the volume total extinction coefficient $\sigma(r)$ is a result of absorption and scattering from molecules and particle. For purposes of a standard backscatter lidar, the absorption is neglected.

**Table 2.3**. Definitions of parameters found in the standard lidar equation

| **Variable** | **Definition** | **Units** |
|---|---|---|
| N(r) | number of photons detected per range bin | - |
| r | distance to the scattering particle | m |
| $E_T$ | transmitted laser energy | J |
| $\lambda$ | laser wavelength | m |
| h | Planck's constant | J sec |
| c | speed of light | m $s^{-1}$ |
| $A_T$ | area of lidar telescope | $m^2$ |
| $\Delta r$ | range bin width | m |
| $Q_E$ | detector quantum efficiency | - |
| $T_O$ | system optical efficiency | - |
| $O_A(r)$ | overlap function | - |
| $P_P(\pi,r)$ | particle backscatter phase function | $sr^{-1}$ |
| $P_M(\pi,r)$ | molecular backscatter phase function | $sr^{-1}$ |
| $B_P(r)$ | particle vol. total scattering coefficient | $m^{-1}$ |
| $\beta_M(r)$ | molecular volume total scattering coefficient | $m^{-1}$ |
| $\sigma(r)$ | volume total extinction coefficient | $m^{-1}$ |
| $B_D$ | thermal noise background signal | - |
| $B_S$ | solar background signal | - |

The first set of ACATS data products are similar to those products derived by cloud-aerosol lidars such as CPL and CALIOP. The standard lidar equation can be regrouped and solved for the attenuated total backscatter (ATB or $\gamma$), which has units of $km^{-1}$ $sr^{-1}$ and is defined as:

$$\gamma(\pi,r) = \left[\beta_M(\pi,r) + \beta_P(\pi,r)\right] * e^{-2\int_0^r \sigma(r')dr} \qquad \text{Eq. 2.4}$$

The ACATS standard ATB is calibrated by normalizing the signal to the molecular backscatter profile at high altitudes where aerosol loading is weakest (Russell *et al.* 1979; Del Guasta 1998). This calibration technique is the well-accepted method of calibrating backscatter lidar signals and is used in CALIPSO and CPL retrievals (McGill *et al.*

2007). The molecular backscatter coefficient is determined from Rayleigh scattering theory (Tenti *et al.* 1974; Young 1981) and is proportional to atmospheric density. Furthermore, the molecular extinction coefficient ($\sigma_M$) is resolved from the molecular backscatter coefficient though the relationship $\sigma_M(r) = \beta_M(\pi,r) * (8/3)\pi$.

ACATS cloud and aerosol layer boundaries are determined using a similar method to CPL (Yorks *et al*. 2011b). For each lidar backscatter profile, a threshold profile is computed as the sum of the minimum attenuated backscatter coefficient and a constant fraction (modeled using CPL data) of the square root of the variance of the attenuated backscatter coefficient. If the attenuated backscatter coefficient is above this threshold for three consecutive range bins, these bins are designated a layer. The top height of the layer is located at the height where the highest of the consecutive samples is found and the bottom height of the layer is the height of the bin just above where the first of three consecutive below-threshold samples is located.

There are two common methods to estimate optical properties from the ATB data. For optically thick clouds or profiles with low SNR, a constant and known lidar ratio is assumed throughout the particulate layer. The following relationships must be defined, assuming no multiple scattering effects:

$$T_p^2(r) = \exp\left(-2\int_{r_0}^{r} \sigma_p(r)\,dr\right) \quad \text{and} \quad S'_p = \frac{\sigma_p}{\beta_p} \qquad \text{Eq. 2.5}$$

and

$$T_m^2(r) = \exp\left(-2\int_{r_0}^{r} \sigma_m(r)\,dr\right) \quad \text{and} \quad S_m = \frac{\sigma_m}{\beta_m}, \qquad \text{Eq. 2.6}$$

where $S_m$ and $S'_p$ are the molecular and effective particulate lidar ratios, respectively, and

$S'_p$ is assumed to be a constant for each layer. The molecular transmission $[T_m^2(r)]$, molecular backscatter coefficient $[\beta_m(r)]$, and atmospheric temperature profiles were obtained using the WMO (World Meteorological Organization) Upper Air station radiosonde closest in space and in time to the ER-2 flight track for each flight. Luers and Eskridge (1998) report the uncertainties in the temperature profiles from these radiosonde instruments. Once the molecular backscatter coefficient and two-way molecular transmission are computed, the lidar equation (Eq. 2.3) can be used to solve for the vertical profile of $T_p^2$ by the method outlined in the appendix of Spinhirne *et al.* (1980). The optical properties such as particulate backscatter coefficient, optical depth, and extinction profiles are estimated from the values of $S_p$, and $T_p^2$.

For transparent cloud and aerosol layers, a more accurate estimate of optical properties can be achieved as outlined below for the CPL instrument. The layer-integrated values of lidar ratio are determined using a similar method to Fernald *et al.* (1972) and Spinhirne *et al.* (1980), by calculating an iterative best-fit lidar ratio based on measuring the cloud layer two-way transmission loss as indicated by the reduction in CPL measured molecular scattering below the transparent or semi-transparent cloud bottom. The first step is to obtain values of effective particulate transmission squared, which by definition does not include a multiple scattering correction factor. The effective particulate transmission squared for a slant angle θ is defined as $T'^{\,2sec\theta}_p\,(r_t)$ and $T_p^{2sec\theta}\,(\mathrm{r}_b)$ at the top and bottom of the layer, respectively, where θ is the tilt angle of the instrument. The $T'^{\,2sec\theta}_p\,(\mathrm{r}_t)$ term is assumed to equal the $T'^{\,2sec\theta}_p\,(\mathrm{r}_b)$ term of all layers above the current layer, or 1.0 if there is no layer above. The $T'^{\,2sec\theta}_p\,(\mathrm{r}_b)$ term for the current layer can be estimated if the presumed clear atmosphere directly below the particulate layer is at least 616 m in physical thickness (i.e., 20 range bins) with a zone-mean (vertical average of all bins within the ”clear air” zone) SNR greater than the 0.2 threshold for 532 nm (0.25 for 1064 nm). If the particulate layer meets these criteria, the effective transmission $T'_p{}^{2sec\theta}$ ($r_b$) is approximated by comparing the integrated lidar signal, which has been attenuated by the particulate layer, in the presumed clear atmosphere (with maximum thickness of 3 km) directly below the particulate layer ($\Gamma_i$) to the modeled integrated molecular signal at the same altitude assuming no attenuation by the cloud layer ($\Gamma_0$), as shown in the equation below from Spinhirne et al. (1996)

$$T_p'^{2\sec\theta}(r_b) = \frac{\Gamma_i}{\Gamma_0}. \qquad \text{Eq. 2.7}$$

This equation can also be written using the total attenuated backscatter coefficient at each height bin [$\gamma'(\pi,r)$], the molecular backscatter assuming no attenuation by the cloud layer [$\beta_m(\pi,r)$], the molecular transmission calculated from the plane altitude to height r assuming no attenuation by the cloud layer [$T_m{}^{2sec\theta}$ ($r$)], the distance to the bottom of the particulate layer ($r_b$) and the distance to the end of the clear air analysis zone ($r_c$)

$$T_p'^{2\sec\theta}(r_b) = \frac{\int_{r_b}^{r_c} \gamma(\pi,r)\,dr}{\int_{r_b}^{r_c} \beta_m(\pi,r) T_m^{2\sec\theta}(r)\,dr}. \qquad \text{Eq. 2.8}$$

This method is called the transmission loss method (or constrained lidar ratio method). The divisor incorporates the accumulated molecular transmission loss starting from the instrument height assuming no cloud layer was detected.

The optical depth and the signal loss can then be quantified by the $T'_p{}^{2sec\theta}$ ($r_b$) parameter. The equation for the cloud layer optical depth ($\tau_{\text{layer}}$) is

$$\tau_{layer} = -0.50 \ln \frac{T_p'^{2\sec\theta}(r_b)}{T_p'^{2\sec\theta}(r_t)}. \qquad \text{Eq. 2.9}$$

To obtain the effective lidar ratio ($S'_p$), the transmission form of the slant angle lidar equation integrated over the layer from $r_t$ to $r_b$ is invoked. The equation is derived by Spinhirne et al. (1980), where $T'^{2sec\theta}_p$ ($r_b$) is computed using Eq. 2.8 for an equally qualifying $r_c$ and $r_t$

$$T_p'^{2\sec\theta}(r_b)T_m^{2X\sec\theta}(r_b) = T_p'^{2\sec\theta}(r_t)T_m^{2X\sec\theta}(r_t) - 2\sec\theta \int_{r_t}^{r_b} S'_p\beta'(r)T_m^{2(X-1)\sec\theta}(r)dr \qquad \text{Eq. 2.10}$$

where $X \equiv \frac{S'_p}{S_m}$. To simplify the equation, we can define the transmission boundary condition at the top of any layer [$I_B$ ($r_t$)], and similarly for the bottom of any layer, as

$$I_B(r_h) = T_p'^{2\sec\theta}(r_h)T_m^{2X\sec\theta}(r_h) \qquad \text{Eq. 2.11}$$

If the particulate layer is the first layer encountered, the term $T'^{2sec\theta}_p$ ($r_b$) can be estimated as 1.00. The effective lidar ratio ($S'_p$) can then be calculated through an iterative solution from the equation

$$S'_p = \frac{I_B(r_t) - I_B(r_b)}{2\sec\theta \int_{r_t}^{r_b} \beta'(r)T_m^{2(X-1)\sec\theta}(r)dr} \qquad \text{Eq. 2.12}$$

assuming $S'_p$ is constant through the particulate layer. The iterative process is started with an initial guess of $S'_p$ as it relates to the *X* parameter, with the next iteration using the calculated value until the solution converges to a set tolerance of 0.08 sr. To convert the effective lidar ratio to the true lidar ratio ($S_p$), $S'_p$ is divided by the multiple scattering factor (η) associated with the layer. For CPL, η is assumed to be 1.0 since multiple scattering effects are negligible for cirrus cloud measurements (McGill et al. 2003).

The particulate backscatter coefficient with attenuation removed ($\beta_p$) and particulate extinction coefficient ($\sigma_p$) can be determined from the values of $S'_p$ and $T'^{\,2sec\theta}_p$. The equation for the backscatter coefficient is obtained by using the results from equation 2.10 as input to equation 2.4 and rearranging:

$$\beta_p(\pi,r) = \frac{\beta'(\pi,r)}{T_m^{2\sec\theta}(r)\,T_p^{2\eta\sec\theta}(r)} - \beta_m(\pi,r) \qquad \text{Eq. 2.13}$$

Once the particulate effective transmission and backscatter profiles for each layer have been calculated, the extinction profile through the layer is then expressed as a simple product of $S_p$ and $\beta_p(\pi,r)$. The advantage of using this retrieval scheme is that the particulate layer properties can be obtained at higher resolutions, both vertically and horizontally, than using the HSRL retrieval algorithms. Therefore, this "standard" lidar method is used to compute ACATS attenuated total backscatter, as well as cloud and aerosol layer boundaries at a vertical resolution of 40 m and horizontal resolution of 400 m (2 sec).

### 2.3.2 *Development of HSRL Algorithms*

The ACATS HSRL retrieval algorithms are different compared to the algorithms of current iodine filter HSRL systems (Hair *et al.* 2008). The inclusion of an etalon in the ACATS instrument design results in a more complicated ACATS lidar equation compared to the standard lidar equation and iodine filter HSRL equations. The etalon transmission function (Eq. 2.1) is convolved with the standard backscatter lidar equation (Eq. 2.3) to yield the expression for the number of photon counts detected per channel (j), as derived in McGill 1996:

$$N(r,j) = \frac{E_T \lambda}{hc} O_A(r) \frac{A_T}{4\pi r^2} \Delta r Q_E T_O T_F(\lambda) \frac{\eta(j)}{n_C}$$
$$\times \sum_{n=0}^{\infty} A_{n,j} \mathrm{sinc}(\frac{n}{N_{FSR}}) \exp(\frac{-\pi^2 n^2 \Delta\lambda_L^2}{\Delta\lambda_{FSR}^2})[\alpha(r) + \omega(r) \exp(\frac{-\pi^2 n^2 \Delta\lambda_M^2}{\Delta\lambda_{FSR}^2})]$$
$$\times \cos[2\pi n(\frac{\lambda_0 - \lambda_C}{\Delta\lambda_{FSR}} - \frac{2U_{LOS}(r)\lambda_0 \sin\varphi}{c\Delta\lambda_{FSR}} - \frac{j}{N_{FSR}})] \qquad \text{Eq. 2.14}$$

The first term represents the instrument parameters. The second term contains the laser broadening ($\Delta\lambda_L$), molecular broadening ($\Delta\lambda_M$), and the atmospheric physics. The attenuated particulate backscatter ($\alpha$) and attenuated molecular backscatter ($\omega$) are expressed as:

$$\omega(\pi,r) = \beta_M(\pi,r) * e^{-2\int_0^r \sigma(r')dr} \qquad \text{Eq. 2.15}$$

$$\alpha(\pi,r) = \beta_P(\pi,r) * e^{-2\int_0^r \sigma(r')dr} \qquad \text{Eq. 2.16}$$

The Doppler shift is characterized by the second part of the third term, where $U_{LOS}$ is the LOS wind velocity in $ms^{-1}$. The attenuated particulate backscatter, attenuated molecular backscatter, and LOS wind velocity are the three unknown variables in Equation 2.14. Since there are 24 detector channels, the ACATS system is an over-determined set of equations. These three unknowns are determined using a method developed by McGill *et al.* (1997b). First, the ACATS lidar equation (Eq. 2.5) is linearized by expanding the relevant variables in a Taylor series. The equation is then written in matrix form:

$$\begin{bmatrix} N_1 - N_{0,1} \\ \cdot \\ \cdot \\ N_{24} - N_{0,24} \end{bmatrix} = \begin{bmatrix} \left.\frac{\partial N_1}{\partial U_{LOS}}\right|_{U_{LOS,0}} & \left.\frac{\partial N_1}{\partial \alpha}\right|_{\alpha_0} & \left.\frac{\partial N_1}{\partial \omega}\right|_{\omega_0} \\ \cdot & \cdot & \cdot \\ \cdot & \cdot & \cdot \\ \left.\frac{\partial N_{24}}{\partial U_{LOS}}\right|_{U_{LOS,0}} & \left.\frac{\partial N_{24}}{\partial \alpha}\right|_{\alpha_0} & \left.\frac{\partial N_{24}}{\partial \omega}\right|_{\omega_0} \end{bmatrix} \begin{bmatrix} U_{LOS} - U_{LOS,0} \\ \alpha - \alpha_0 \\ \omega - \omega_0 \end{bmatrix} \qquad \text{Eq. 2.17}$$

This equation can also be written as:

$$\Delta N = G \Delta x \qquad \text{Eq. 2.18}$$

An iterative weighted least-squares fitting technique is employed to resolve these three parameters and their corresponding uncertainty, in which the solution is:

$$\Delta x^{est} = \left(G^T W G\right)^{-1} G^T W \Delta N \qquad \text{Eq. 2.19}$$

where W is the weighting matrix and G is the generalized matrix to be inverted. The solution for the molecular and particle signals are linear, but non-linear for the Doppler shift. This least-squares fit method is tested and proven by McGill *et al.* (1997b) to retrieve the horizontal wind velocity. I advance the effort of McGill *et al.* (1997a) and McGill *et al.* (1997b) by using the definitions of attenuated particulate backscatter (Eq. 2.16) and attenuated molecular backscatter (Eq. 2.15) to develop HSRL retrievals of cloud and aerosol properties. The first step is to compute the molecular backscatter coefficient and two-way transmission ($T_M^2$) from Rayleigh scattering theory and meteorological data from a WMO (World Meteorological Organization) Upper Air station radiosonde closest in space and in time to the ER-2 flight track for each flight. The definition for the attenuated molecular backscatter (Eq. 2.15) can be rewritten in terms of the two-way transmission, corrected for the slant path, and solved for the two-way particle transmission ($T_p^2$):

$$T_P^2(r) = \left[ \frac{\omega(\pi,r)}{\beta_M(\pi,r)T_M^2(r)} \right]^{\cos\theta} \qquad \text{Eq. 2.20}$$

Therefore, the two-way particle transmission can be determined without making unnecessary assumptions about the lidar ratio, as in the Klett or Fernald method (Fernald *et al.* 1972; Klett 1981, 1985). Once $T_p^2$ is known, the definition of the attenuated particulate backscatter (Eq. 2.16) can be rewritten and used to directly retrieve the particulate backscatter coefficient ($\beta_P$):

$$\beta_P(\pi,r) = \frac{\alpha(\pi,r)}{T_M^2(r)T_P^2(r)} \qquad \text{Eq. 2.21}$$

The particle optical depth is then:

$$\tau_P(r) = -\frac{1}{2}\ln\left[T_P^2(r)\right] \qquad \text{Eq. 2.22}$$

The particle extinction coefficient ($\sigma_P$) is directly retrieved using the equation:

$$\sigma_P(r) = \frac{\partial\tau_P(r)}{\partial r} \qquad \text{Eq. 2.23}$$

and the particle lidar ratio is:

$$S_P(r) = \frac{\sigma_P(r)}{\beta_P(r)} \qquad \text{Eq. 2.24}$$

This method is used to compute profiles and layer-integrated values of the aforementioned variables at a vertical resolution of 450 m and horizontal resolution of 5 km (25 sec). Their corresponding uncertainties are computed using propagation of errors, as outlined in Appendix A. If higher resolution optical properties are desired, the directly retrieved lidar ratio can be utilized as a parameterization to compute high-resolution optical properties using the Klett or Fernald method.

## 2.4 Initial Results from the WAVE Campaign

During the period of 9 to 27 September 2012, ER-2 aircraft flights were conducted out of Wallops Island, VA as part of the WAVE project. These flights were planned over land, targeting specific land and vegetation surfaces with a scientific objective of simulating ICESAT-2 data using the MABEL instrument (McGill *et al.* 2013). ACATS was part of a payload on a total of 13 ER-2 flights, which included observations of thin cirrus clouds, and smoke layers. During these flights, software directed the ACATS telescope to rotate counter-clockwise to four look angle positions denoted by azimuth angle relative to the aircraft nose: $0^o$ (fore), $90^o$ (right or starboard), $180^o$ (aft), and $270^o$ (left or port). At each look angle, the dwell time was set for 60 seconds. The WAVE campaign represents the first science flights for the ACATS instrument in which the telescope rotated and more than one look angle was used. Due to limited time before the project, I was only able to optimize the telescope alignment at the 270-degree look angle. The telescope alignment for the other three look angles was performed in the field using the new and untested in-flight telescope alignment procedure. Portions of flights, and in some cases entire flights, were used to test and refine the etalon calibration procedure and telescope alignment. Furthermore, only two look angles were used for some flights if proper telescope alignment was not achieved at all four look angles due to the instability of the telescope bearing. An example of the photon counts summed across all 24 detector channels at each of the four look angles from the 26 September 2012 flight is shown in Figure 2.6 and demonstrates the ability of ACATS to observe cirrus clouds (between 10 and 12 km) at multiple look angles. Overall, ACATS collected science data with high SNR in at least one look angle during 8 of the 13 total flights. The telescope alignment and LOS wind retrievals will be improved before future ACATS flights. This study will focus on ACATS retrievals of cloud and aerosol properties from the WAVE project, particularly those at the 270-degree look angle and high quality data from the other look angles.

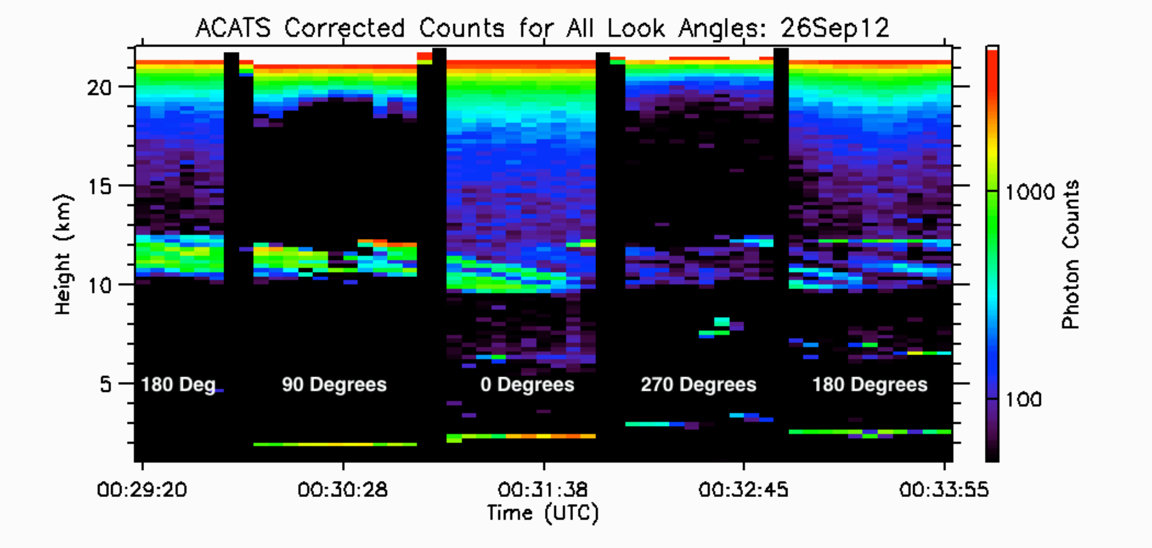

**Figure 2.6**. ACATS photon counts from an ER-2 flight on 26 September 2012. The high count rates between 10 and 12 km show the detection of a cirrus layer at all four look angles at intervals of 60 seconds. The high photon counts (greater than 1,000) around 21 km are the near field return off of the molecular atmosphere, since these values are not range-corrected.

There were several flights during WAVE in which ACATS collected quality data at multiple look angles. Perhaps the best ACATS performance was on the 26 September ferry flight back to Palmdale, CA when all four look angles were well aligned. Figure 2.7 shows the 532 nm ATB ($km^{-1}$ $sr^{-1}$) computed using the standard method (a), the Attenuated Particulate Backscatter ($km^{-1}$ $sr^{-1}$) using the HSRL method (b), and the directly-retrieved Particulate Extinction Coefficient ($km^{-1}$) at the 0 degree look angle (c) for the flight on 26 September 2012. Clearly visible in these images are cloud layers observed by ACATS as the ER-2 flew over the Ohio River Valley (20:28:05 to 21:30:00 UTC) and over North Dakota (about 00:24:10 UTC). ACATS also measured a large smoke plume (00:24:10 to 02:10:00 UTC) that extended as high as 6 km over Montana.

The images in Figure 2.7 demonstrate the typical ACATS cloud and aerosol data products. The extinction and backscatter values are typical for cloud and smoke layers and appear to be similar across retrieval methods.

The ACATS telescope alignment on the 14 Sept. flight at the 270 degree look angle was the best for the entire campaign, making it a good case to assess biases in the two retrieval methods. Figure 2.8 shows the 532 nm ATB computed using the standard method (a) and using the HSRL method (b). The latter is essentially $\alpha + \omega$. Cirrus clouds between 9 and 13 km were observed throughout the flight. Figure 2.9 shows the mean profiles of 532 nm ATB computed using the standard method (blue) averaged to the resolutions of the HSRL products, as well as the ATB using the HSRL method (red) for the grey shaded box in Figure 2.8b centered around 22:32:22 UTC. Both ATB profiles follow the modeled molecular profile closely above the cirrus layer and show similar structure inside the cirrus layer. The standard ATB retrieval is about 10 percent higher than the ATB computed using the HSRL method within the cirrus layer, within the combined uncertainty of the both retrievals. The error in the ACATS Rayleigh normalization constant is similar to the CPL calibration constant, estimated to be around 5 percent at 532 nm due to signal noise and the presence of aerosols in the calibration zone (Campbell *et al.* 2008; Vaughan *et al.* 2010). Errors in the determination of the etalon defect parameter and HOE normalization values can lead to errors in the HSRL retrieved attenuated molecular and particulate backscatter. The sensitivity of the ACATS HSRL data products to the calibration parameters will be discussed in the next section. Although this comparison provides confidence in the ACATS HSRL algorithms, it does not resolve any possible instrument biases. To address this issue, the ACATS standard backscatter and HSRL products are compared to coincident CPL cloud and aerosol properties during the WAVE campaign in the next chapter.

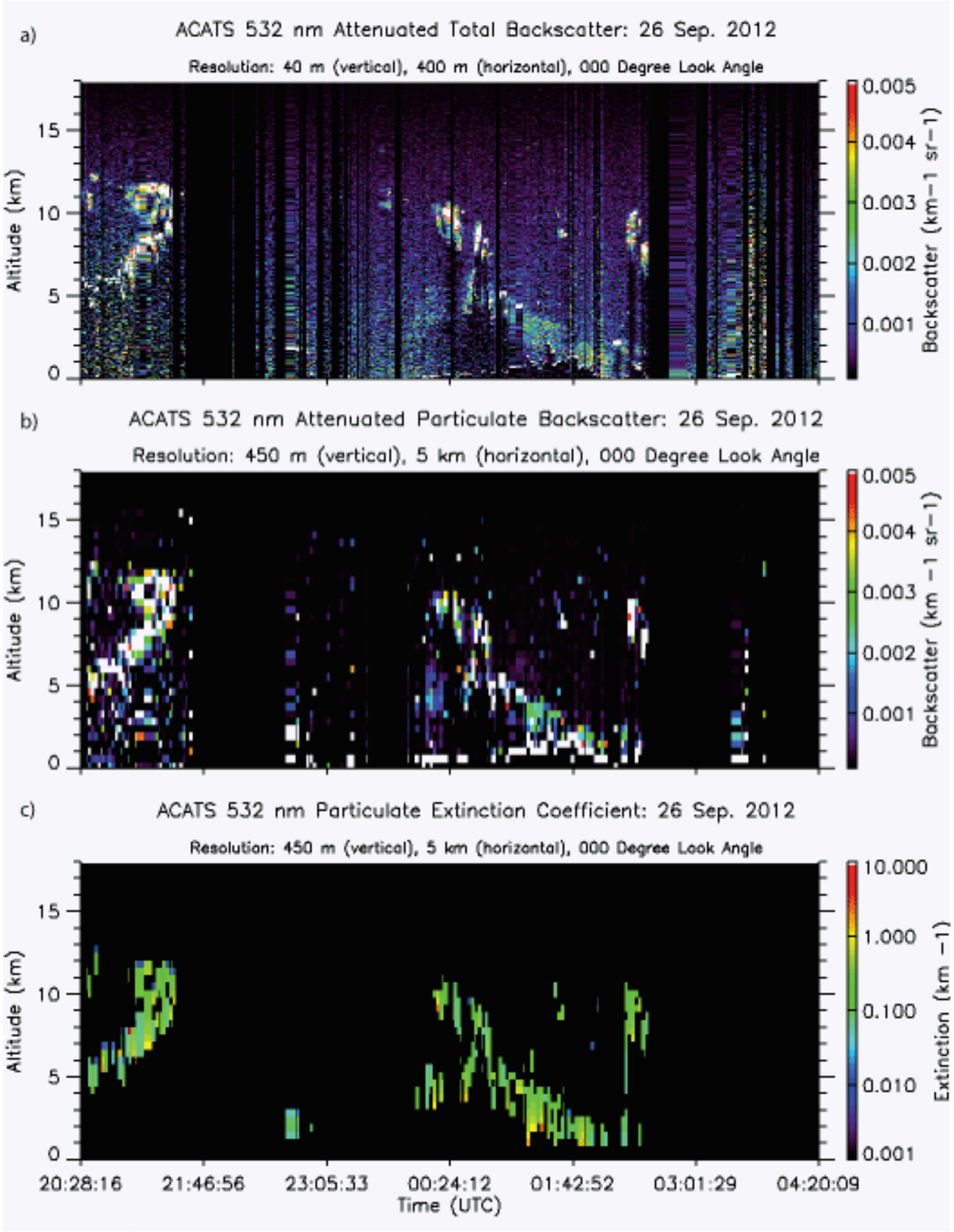

**Figure 2.7**. The ACATS 532 nm ATB (km$^{-1}$ sr$^{-1}$) computed using the standard method (a), the Attenuated Particulate Backscatter (km$^{-1}$ sr$^{-1}$) derived using the HSRL method (b), and the directly-retrieved Particulate Extinction Coefficient (km$^{-1}$) at the 0 degree look angle (c) for the WAVE flight on 26 September. Cloud layers were detected over the Ohio River Valley (20:28:05 to 21:30:00 UTC) and over North Dakota (about 00:24:10 UTC). A large smoke plume (00:24:10 to 02:10:00 UTC) that extended as high as 6 km was observed over Montana.

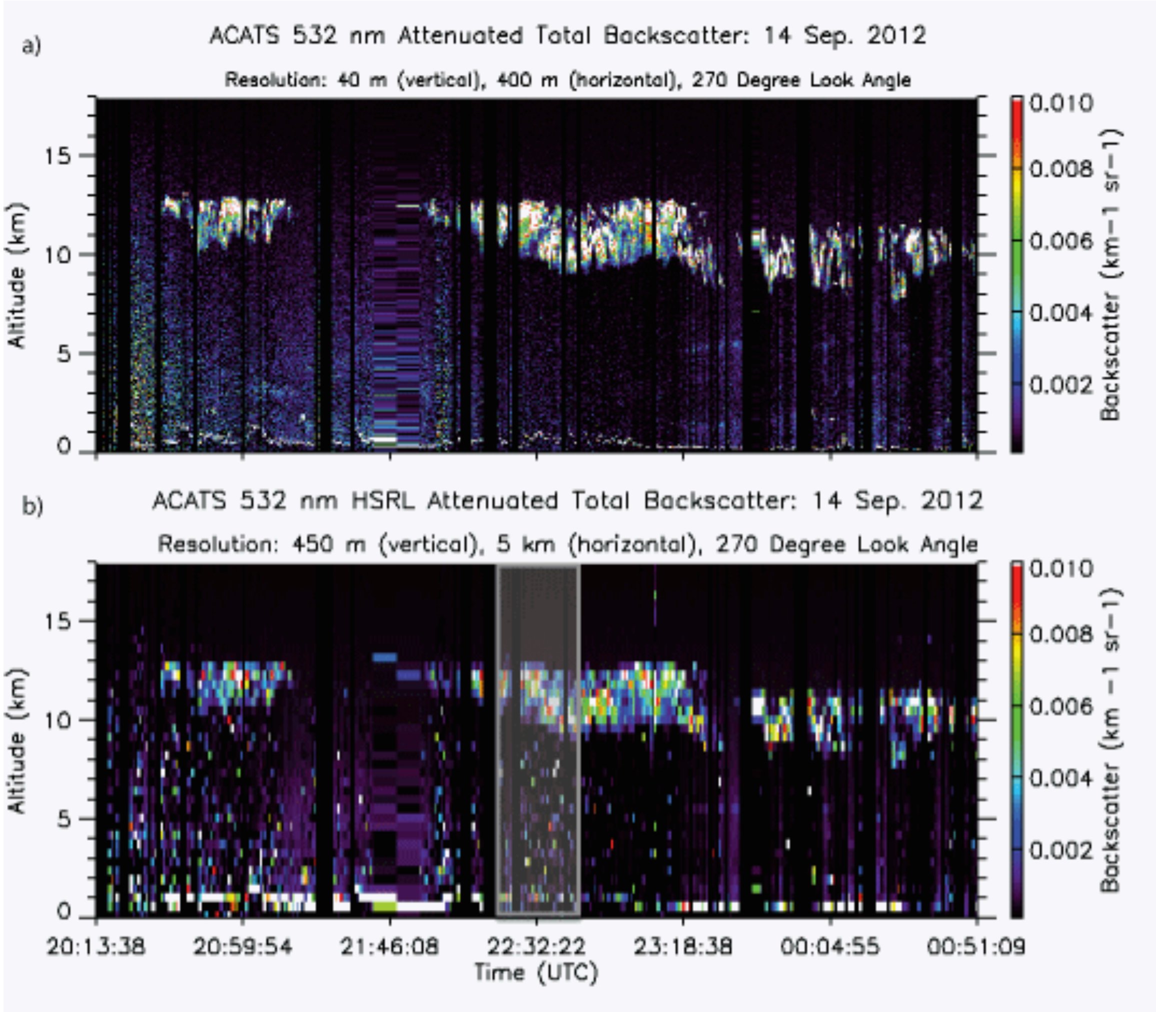

**Figure 2.8**. The ACATS 532 nm Attenuated Total Backscatter computed using the standard method (a) and using the HSRL method (b) at the 270 degree look angle for the ER-2 flight on 14 September. The grey box focuses on a 35 minute segment in which the mean profiles are compared in Figure 2.9 for cirrus clouds.

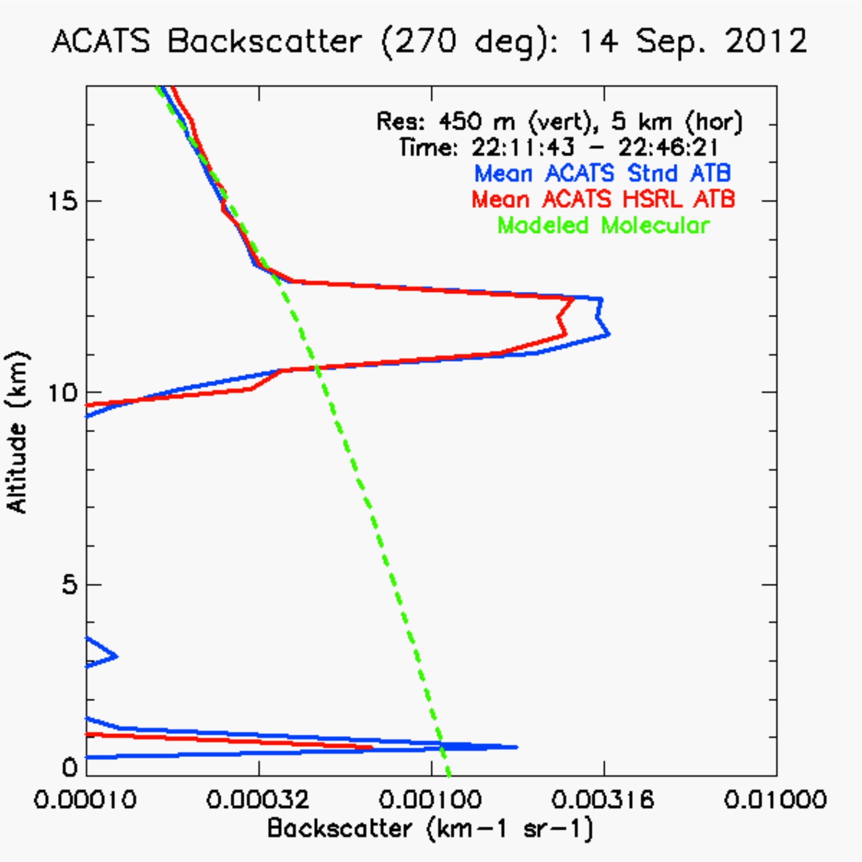

**Figure 2.9**. The ACATS mean profiles of 532 nm ATB computed using the standard method (blue) averaged to the resolutions of the HSRL products, as well as the ATB using the HSRL method (red) for the grey shaded box in Figure 2.8b (22:11:43 – 22:46:21 UTC).

## 2.5 Sensitivity of ACATS HSRL Retrievals to Calibration Procedures

There are three main sources of error in the ACATS HSRL retrievals: detector noise, instrument defect parameter, and HOE normalization values. In this section, I provide the results of a modeling study to assess the sensitivity of the ACATS HSRL retrievals to the ACATS calibration procedures. I construct a simulated atmospheric scene using the molecular atmosphere as computed from temperature and pressure profiles over the tropics using a GEOS-5 forecast from July 15, 2009. Embedded in this molecular atmosphere is a cirrus cloud between 10 and 12 km altitude with the properties shown in Table 2.4. It is assumed that the extinction and backscatter has a constant value through the cirrus layer and that the scene is during the nighttime hours (no solar background simulated). Using the ACATS lidar equation (Eq. 2.14), ACATS instrument parameters (Table 2.1), and the profiles of attenuated particle and molecular backscatter ($\alpha$ and $\omega$), the photon counts measured by the ACATS instrument are simulated for 60 m range bins and a 1 sec record. The ACATS defect parameter is assumed to be 20.0 nm for all channels and the HOE detector normalization values in Table 2.2 are employed in the simulation. The simulated photon counts are duplicated to create 2000 profiles and a Poisson random number generator is applied to each bin and profile to represent the detector noise present in true ACATS measurements.

**Table 2.4**. Simulated cirrus layer properties.

| **Parameter** | **Value** | **Units** |
|---|---|---|
| COD | 0.40 | - |
| $\alpha$ | 0.00485 | $km^{-1}$ $sr^{-1}$ |
| $\sigma p$ | 0.20 | $km^{-1}$ |
| $\beta p$ | 0.008 | $km^{-1}$ $sr^{-1}$ |
| Sp | 25.0 | sr |

I used the simulated photon counts to perform eleven tests in which the ACATS HSRL products are retrieved (as presented in Section 2.3) at the standard vertical (450 m) and horizontal (25 sec) resolutions of the HSRL products. The error is computed for the attenuated particulate and molecular backscatter, as well as the lidar ratio, particle extinction and backscatter coefficients using propagation of errors as outlined in Appendix A. The relative error is estimated for a parameter (x) using the equation:

$$\varepsilon(x) = \frac{\delta_x}{x} \times 100 \qquad \text{Eq. 2.25}$$

For one test I assumed that all the calibration parameters are known without error, so that the only source of error in the ACATS HSRL retrievals is the detector noise. Figure 2.10 shows the retrieved attenuated particle (red) and molecular (blue) backscatter coefficients for the simulated atmospheric scene (dashed lines). The retrieved attenuated particulate and molecular backscatter agree very well with the simulated profiles when no calibration errors are included. Table 2.5 shows the mean error in attenuated particulate and molecular backscatter, as well as the lidar ratio, particle extinction and backscatter coefficients averaged over 2000 profiles for a range in defect parameter errors of 0-40%. When there is no error in the computation of the defect parameter or HOE normalization constants, there is less than 5% error in the ACATS attenuated particle and molecular backscatter coefficients and about 15-20% error in the lidar ratio and extinction coefficient.

I performed a set of tests in which HOE normalization values are held constant at their simulated values, but the error in the defector parameter is increased incrementally by 10%. As the error in the defect parameter increases to 40%, the retrieval does not accurately determine the molecular backscatter component (blue) of the signal within the cirrus layer, as shown in Figure 2.11. This causes the error in the attenuated molecular backscatter to increase to over 20%, which propagates to error in the retrieved extinction coefficient and lidar ratio of over 40%. The attenuated particulate backscatter is less sensitive to error in the defect parameter. The error in the attenuated particulate backscatter remains below 6% and the profile of retrieved attenuated particulate backscatter (red) is nearly identical to the simulated profile (purple) in Figure 2.11. The error in the particulate backscatter coefficient [ε(β)] is 20-30% lower than the extinction and lidar ratio, because it is not dependent on ε(ω), only on ε(α).

**Table 2.5**. Relative error (%) in ACATS retrievals for error in defect parameter.

| ε (Defect) | ε (α) | ε (ω) | ε (βp) | ε (σ) | ε (Sp) |
|---|---|---|---|---|---|
| 0.00 | 2.99 | 3.59 | 6.843 | 16.77 | 18.11 |
| 10.00 | 3.81 | 4.35 | 7.645 | 17.55 | 19.15 |
| 20.00 | 4.10 | 7.80 | 10.132 | 22.26 | 24.46 |
| 30.00 | 4.78 | 15.08 | 16.591 | 35.21 | 38.93 |
| 40.00 | 5.84 | 20.51 | 21.904 | 45.87 | 50.83 |

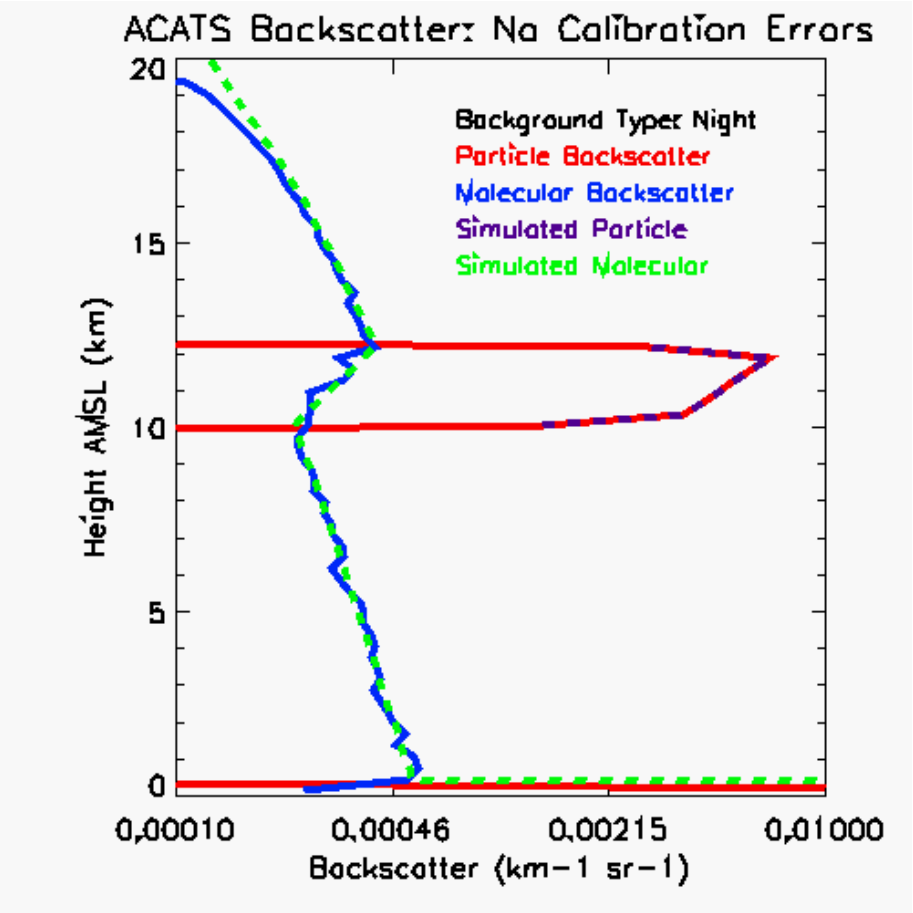

**Figure 2.10.** The ACATS attenuated particulate (red) and molecular (blue) backscatter profiles retrieved from the simulated profiles of attenuated particulate (purple) and molecular (green) backscatter assuming no errors in the calibration parameters.

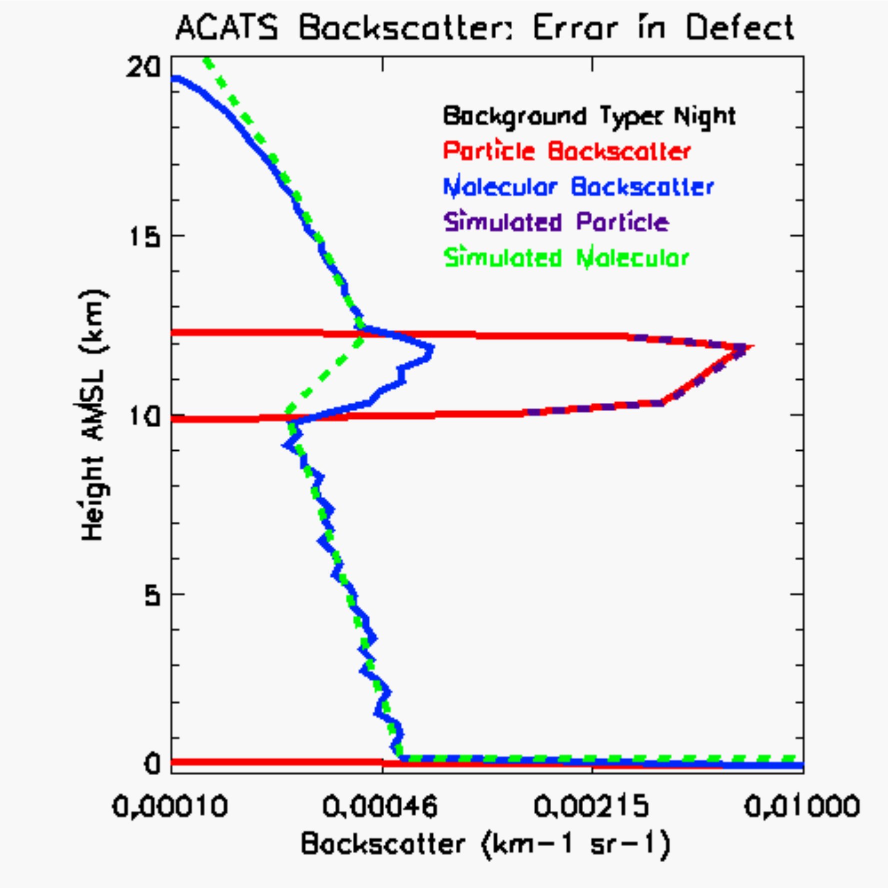

**Figure 2.11.** The ACATS attenuated particulate (red) and molecular (blue) backscatter profiles retrieved from the simulated profiles of attenuated particulate (purple) and molecular (green) backscatter assuming 30% error in the ACATS defect parameters.

I performed another set of six tests that assume all the defect parameters are known without error, so that the only sources of error in the ACATS HSRL retrievals are the detector noise and HOE normalization values. These six tests assume the error in the HOE normalization is increased in increments of 5 %, with a range of 5 to 30 %. Table 2.6 shows the mean error in attenuated particulate and molecular backscatter, as well as the lidar ratio, particle extinction and backscatter coefficients averaged over the 2000 profiles for these six tests. Error in the HOE normalization values cause a shift in the attenuated particulate (red) and molecular (blue) backscatter profiles compared to the simulated profiles of attenuated particulate (purple) and molecular (green) backscatter, as shown in Figure 2.12. The relative magnitude of this shift is slightly less than the error found in the HOE normalization values (Table 2.6). When there is a 30% error in the determination of the normalization values, the error in the lidar ratio and extinction increases to over 50%, while the error in particulate backscatter remains below 33%. The accuracy at which both the etalon defect and HOE normalization values are determined depends on the quality of the etalon calibration scans performed during flight and initial ground testing.

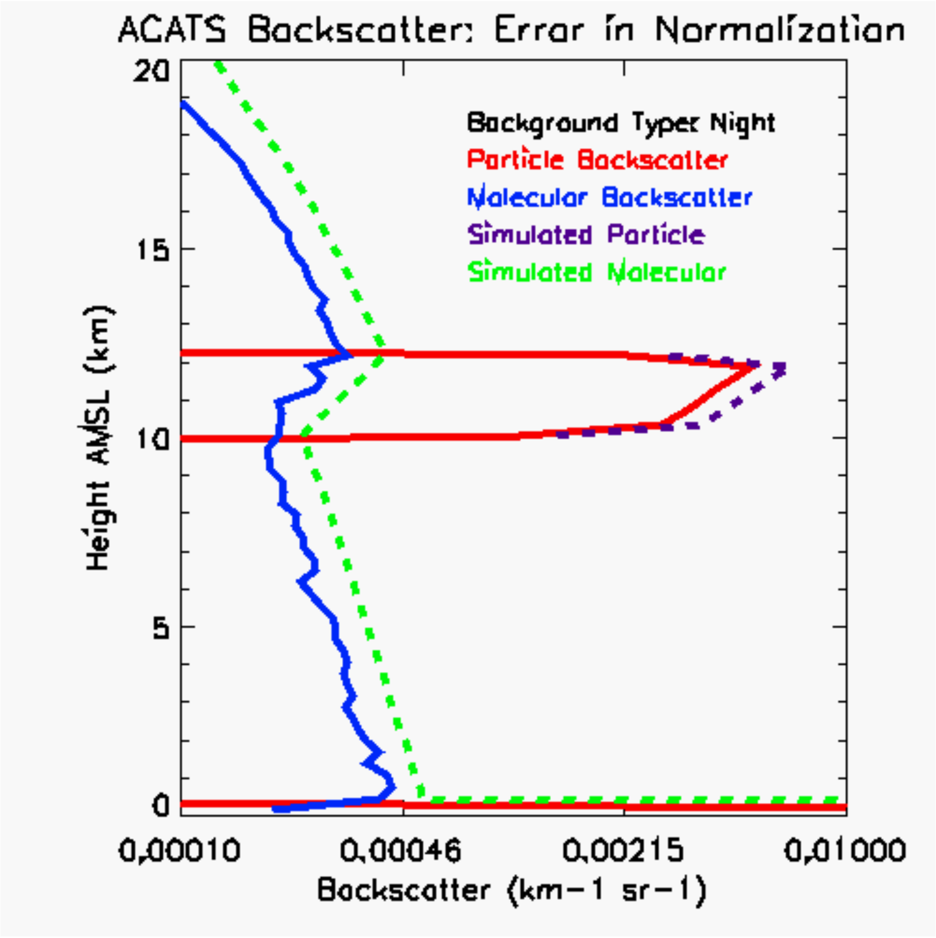

**Figure 2.12.** The ACATS attenuated particulate (red) and molecular (blue) backscatter profiles retrieved from the simulated profiles of attenuated particulate (purple) and molecular (green) backscatter assuming 30% error in the ACATS HOE normalization values.

**Table 2.6**. Relative error (%) in ACATS retrievals for error in HOE normalization.

| ε (Norm) | ε (α) | ε (ω) | ε (βp) | ε (σ) | ε (Sp) |
|---|---|---|---|---|---|
| 5.00 | 5.01 | 6.63 | 9.698 | 20.49 | 22.67 |
| 10.00 | 9.33 | 9.91 | 14.5 | 25.74 | 29.54 |
| 15.00 | 13.27 | 13.52 | 19.593 | 32.26 | 37.74 |
| 20.00 | 16.88 | 16.82 | 24.348 | 38.58 | 45.62 |
| 25.00 | 20.21 | 19.86 | 28.773 | 44.57 | 53.05 |
| 30.00 | 23.28 | 22.82 | 32.98 | 50.51 | 60.32 |

The errors in the ACATS HSRL retrievals demonstrated here due to errors in the defect parameter, HOE normalization values, and detector noise are likely observed in the ACATS HSRL retrievals from the WAVE project, although not to the extreme presented here. The ACATS detector normalization values are determined in the lab using a broad bandwidth white-light source and are known to within 1%. It is assumed that the error in the detector normalization values is very small compared to the signal noise. However, the accuracy of the HOE normalization values and defect parameters are a function of the ACATS etalon stability. Between ground testing in April 2012 and the WAVE flights in Sept. 2012, the ACATS calibration procedure has been performed about 30 times. The defect parameters are determined to within 15% for the ground testing data and to within 20% using the WAVE data. The latter is less accurate due to more instability in the etalon during flight, which will be improved before future flights. The ground testing and WAVE data suggest the errors in the determination of the HOE normalization values are about 2-5%. The 15-20% error in the defect parameter and 2-5% error in the HOE normalization values cause an increase in error of about 2-5% in ACATS HSRL retrievals. Since the ACATS extinction and lidar ratio retrieval error is already slightly higher than 15% due to detector noise, the ACATS extinction and lidar ratio retrievals from the WAVE project have an error of about 20%. Error in the ACATS attenuated particulate and molecular backscatter retrievals from the WAVE project are estimated at 5-10%.

ACATS, a new multi-channel direct-detection Doppler wind lidar for use on the NASA ER-2, employs a Fabry-Perot interferometer to provide the spectral resolution needed to retrieve the Doppler shift, similar to the ground-based University of Michigan Doppler wind lidar (McGill *et al.* 1997a). I advance the technology of a MC direct-detection Doppler wind lidar by demonstrating the utility of ACATS for HSRL retrievals of cloud and aerosol properties. The first ACATS science flights were conducted during the WAVE project in September 2012. I directly retrieve cloud and aerosol optical properties such as extinction and lidar ratio using the HSRL technique outlined in this chapter. Initial results demonstrate the effectiveness of ACATS as an airborne HSRL system. The HSRL ATB retrieval for cirrus observed during the 14 September flight at the 270-degree look angle agrees with the ATB derived using the standard backscatter method to within 10 percent, within the uncertainty of both instruments. Furthermore, I estimate that the ACATS HSRL extinction and lidar ratio retrieval errors due to calibration errors are 15-20 percent.

# Chapter 3: Assessment of ACATS Cloud and Aerosol Retrievals Using Coincident CPL Data

In this chapter, I discuss the validation and evaluation of ACATS cloud and aerosol retrievals for both the standard and HSRL methods using coincident CPL data from the WAVE project in Sept. 2012. A total of 13 flights were conducted during the WAVE campaign, which include ACATS and CPL observations of thin cirrus clouds and smoke layers. These comparisons will also demonstrate the effectiveness of the ACATS HSRL technique in reducing the uncertainties of extinction retrievals from lidar systems. The work I present here has been submitted to the *Journal of Atmospheric and Oceanic Technology* and is currently under the peer-review process (Yorks *et al.* 2014b).

## 3.1 Coincident Measurements

ACATS and CPL collected coincident cloud and aerosol measurements on a total of 8 WAVE flights, which included many observations of thin cirrus clouds and smoke layers. During 4 of the 13 flights, ACATS did not collect science data due to dedicated telescope alignment and etalon scan flights, as well as a hard drive failure. Since the ACATS fore and aft look angles observe nearly the same atmospheric scenes as CPL, data from these look angles can be compared with CPL to assess the performance of the ACATS retrievals. However, ACATS data are not continuous like CPL data since the ACATS telescope was rotating to multiple look angles. CPL attenuated backscatter signals are averaged to 400 m horizontally (2 seconds) for this study to better match the ACATS horizontal spatial resolution of 400 m and vertical resolution of 40 m. Additionally, CPL optical properties are computed at 5 km horizontally and averaged to

450 m vertically to match the ACATS HSRL products. For this study, we restrict the analysis to segments of 25-45 minutes that contain a relatively homogeneous layer top and bottom. Assuming a validation target of cirrus or aerosol layers, a segment of this extent provides enough data points for meaningful statistical analysis, yet minimizes the uncertainties caused by differences in viewing geometries of the instruments.

## 3.2 Similarities and Differences Between ACATS and CPL

There are several fundamental similarities and differences between the ACATS and CPL systems that have an impact in comparing cloud and aerosol properties retrieved by the two instruments. Both CPL and ACATS measure range-resolved backscatter profiles (McGill *et al.* 2002). Thus, "apples-to-apples" comparisons can be performed for measurements over the full extent of the troposphere to the limit of signal attenuation. For ACATS standard backscatter products, a similar calibration method to CPL is employed to compute attenuated total backscatter at 532 nm, as described by McGill *et al.* (2003) and in Chapter 2.3. The HSRL-nature of the ACATS measurements provides added capabilities compared to CPL, such as direct retrievals of extinction. Because ACATS is designed to measure winds, the viewing geometry is different from CPL. Table 3.1 summarizes the hardware specifications of the two instruments. The ACATS FOV is larger than CPL and the ACATS telescope rotates to four different look angles. Also, CPL points nadir while ACATS points off-nadir at an angle of 45 degrees. These differences produce dissimilarities in the timing of the atmospheric layers observed and the SNR of the two instruments, unavoidable given the nature of the ACATS system.

**Table 3.1.** Primary system parameters for the ACATS and CPL lidars.

| **Parameter** | **ACATS** | **CPL** |
|---|---|---|
| Laser type | Nd: YAG, seeded | Nd: YVO4 |
| Wavelengths | 532 nm | 355, 533, 1064 nm |
| Laser repetition rate | 250 Hz | 5000 Hz |
| Laser energy (532) | ~10 mJ/pulse | ~25 μJ/pulse |
| Telescope diameter | 20.3 cm | 20.0 cm |
| Viewing angle | 45 degrees | ~ 0 degrees (nadir) |
| Telescope FOV | 350 μradians | 100 μradians |
| Vertical Res. (raw) | 22 m | 30 m |
| Hori. Res. (raw) | 1 sec / 200 m | 1 sec / 200 m |
| Detector channels | 24 | 4 |

When comparing ACATS to a nadir-pointing lidar such as CPL, the viewing geometry of the ACATS instrument leads to several complications that need to be considered. First, the viewing geometries of the fore (0 degrees) and aft (180 degrees) look angles cause a timing difference compared to CPL that is a function of range. At any given moment, ACATS is looking ahead (0 degrees) or behind (180 degrees) the atmospheric layer observed by CPL. Figure 3.1 illustrates this timing difference for a cloud 10 km below the aircraft. Assuming an ER-2 velocity of 200 ms$^{-1}$, the ACATS 0-degree look angle will view this cloud layer 50 seconds prior to CPL. Therefore, the segment matching is achieved using the proper range-dependent time offset based on the vertical location of the atmospheric layer of interest. The 45 degree off-nadir angle of ACATS also leads to a greater path length compared to CPL, as shown in Figure 3.1.

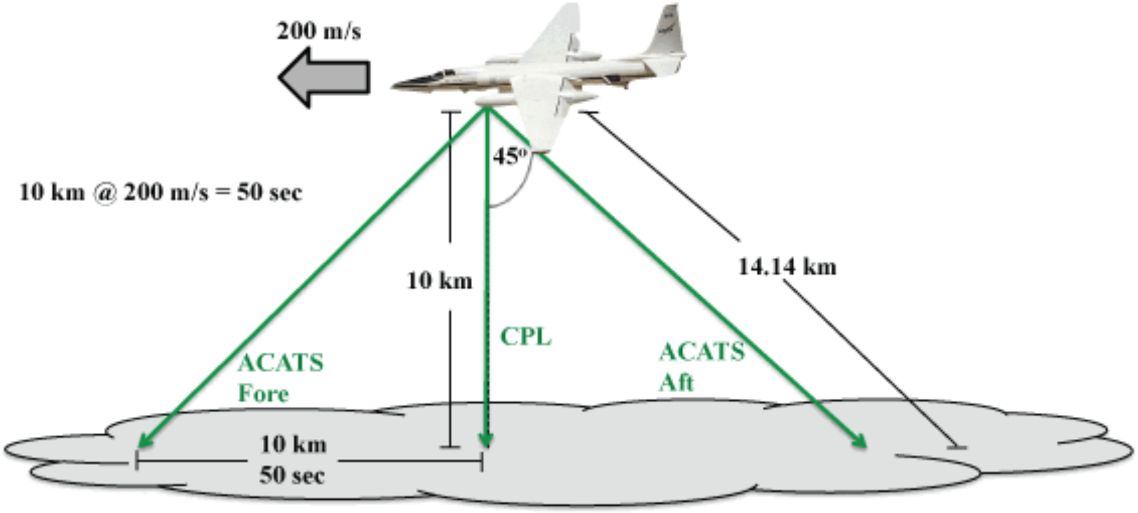

**Figure 3.1**. A schematic demonstrating the timing differences between the ACATS and CPL instruments for a cirrus cloud 10 km below the ER-2 aircraft. In addition to the timing difference, ACATS also has a longer path length than CPL.

The ACATS transmission, if not corrected for the 45 degree slant angle, will be lower than that of CPL. For example, assuming a 2 km thick cloud layer with extinction (σ) of 0.10 km$^{-1}$, the ACATS path length ($\ell$) through the layer would be 2.83 km. Since the equation for the two-way particle transmission is:

$$T_P^2 = e^{-2\sigma\ell} \quad \text{Eq. 3.1}$$

the two-way particle transmission for ACATS is 0.5679, smaller than CPL (0.6703). As shown in Section 2.3.2, the ACATS HSRL-derived optical properties are corrected using $cos\theta$ since the transmission and backscatter variables can be separated using the HSRL technique. However, these two variables cannot be separated when computing standard backscatter products such as the ATB (γ), computed using Eq. 2.3 and rewritten in terms of transmission as:

$$\gamma(r) = \left[\beta_P(r) + \beta_M(r)\right] T_M^2(r) T_P^2(r) \quad \text{Eq. 3.2}$$

Thus, the CPL ATB will be greater than the ACATS ATB for the same scene. ACATS optical properties derived using the HSRL method, such as extinction and lidar ratio, compare more favorably with CPL optical properties since the transmission is corrected for the 45-degree slant path before these variables are computed.

The SNR is fundamentally important to accurate lidar-based retrievals of cloud and aerosol properties and is a function of many instrument parameters, including the telescope alignment and laser energy. For ACATS, the telescope alignment is different at all four look angles. The telescope alignment at the 0, 90, and 180 degree look angles was not ideal for most flights during WAVE. Consequently, the SNR of ACATS is often lower than that of CPL. At 532 nm and resolutions of 5 km horizontal and 60 m vertical, the CPL SNR is four times greater than the ACATS SNR at 15 km for the nighttime 26 September flight. The consequence of this lower SNR is higher ACATS minimum detectable backscatter for optically thin cirrus clouds in comparison to CPL. The latter can inhibit the ACATS layer detection algorithm from distinguishing optically thin cirrus clouds and aerosol layers from the signal noise. The ACATS telescope alignment, and thus SNR, will be improved before future flights.

The ACATS HSRL retrievals for optical properties such as extinction are quite different from the standard backscatter lidar retrievals performed using CPL data. There have been many methods developed to retrieve the particle extinction and particulate backscatter coefficients from a cloud-aerosol lidar return signal. CPL optical properties, such as extinction, are derived using the Klett or Fernald method (McGill *et al.* 2002), which assumes the lidar ratio is known and constant throughout a particulate layer (Fernald *et al.* 1972; Klett 1985). As discussed in Chapter 1, the variability in the lidar ratio for atmospheric layers can create errors in the assumed lidar ratio that propagate to errors in the retrieval of the particle extinction coefficient (Young *et al.* 2013). However, the HSRL technique takes advantage of the difference in spectral distribution of backscattered signal from molecules and particles. As demonstrated by the ACATS HSRL algorithms (Section 2.3.2), ACATS particle extinction and backscatter coefficients can be resolved independently with no assumption about the lidar ratio required. The HSRL method does require coarser resolutions, but reduces the uncertainties in the extinction and backscatter coefficient retrievals.

## 3.3 Assessment of ACATS Data Products

An examination of the ACATS cloud and aerosol properties is performed for both the standard backscatter and HSRL products using CPL data at similar spatial scales. The validation includes an assessment of lidar ratio statistics, as well as a direct comparison of attenuated backscatter, layer boundaries, and extinction retrievals for three case studies. These case studies include an optically thin cirrus layer during the 14 Sept. flight, an elevated smoke plume during the 26 Sept. flight, and a complex scene of cirrus, water clouds, and smoke during the 26 Sept. flight. These cases are chosen because they represent interesting atmospheric layers observed during flights in which ACATS collected data with high SNR in the fore and/or aft look angles due to near optimal telescope alignment. Images of ATB, layer boundaries, and extinction are evaluated for each case and mean profiles of extinction are computed for the coincident data in which ACATS was operating in the fore and/or aft look angle. The CPL layer detection, ATB, and extinction products, with high SNR and high horizontal resolution, will be considered the “true atmospheric scene” for the case studies.

The 14 Sept. case shown in Figure 3.2 is a 28-minute segment obtained over New England during local evening hours as the aircraft flew southward from 43.9 to 41.0 degrees latitude. For the duration of this flight ACATS was operating at two look angles, 180 degrees and 270 degrees, collecting data for 60 seconds before rotating to the next look angle. Thus, the 180-degree look angle is compared to the CPL data with a 43 second time offset, corresponding to a range from the aircraft of 8.6 km (approximate altitude of 11.4 km). Figure 3.2 shows the 532 nm ATB ($km^{-1}$ $sr^{-1}$) from both 400 m CPL data (a) and 400 m ACATS data (b) for the segment. There is considerable structure within this cirrus layer, including a few breaks and possible subvisual cirrus at the cloud top north of 42.4 degrees, which is discernible in the CPL attenuated backscatter image but appear faint or absent in the ACATS attenuated backscatter image (Figure 3.2). CPL ATB is greater in magnitude than ACATS due to the lower ACATS two-way transmission previously discussed in Section 3.2. The CPL and ACATS cloud layer boundaries are plotted for the segment at a horizontal resolution of 400 m in Figure 3.2c. The ACATS cloud boundaries (blue) are in excellent agreement with CPL cloud boundaries (red) at the cloud base. CPL detects the possible subvisual cirrus near the top of the layer between 11 and 12 km, as illustrated in Figure 3.2a. The ACATS layer detection algorithm fails to detect this optically thin portion of the cirrus top boundaries (Figure 3.2c). This disagreement between the two instruments is a consequence of the lower ACATS SNR and ATB at the 180-degree look angle compared to CPL, making these layers difficult to distinguish from the molecular backscatter profile in the ACATS data.

A more “apples-to-apples” comparison of CPL and ACATS data is achieved by correcting the ACATS optical properties for the 45-degree slant path. This process is performed in the ACATS HSRL retrievals and removes any bias in the ACATS data due to the off-nadir view angle. Figure 3.3 shows the extinction coefficient ($km^{-1}$) at 532 nm from both 5 km CPL data (a) and 5 km ACATS HSRL data (b) for the segment, averaged to 450 m vertically. The additional averaging allows ACATS to detect more of the optically thin cirrus top then possible in the standard backscatter products. Higher extinction values are observed near cloud base by both instruments. Mean profiles of 532 nm extinction for ACATS (blue) and CPL (red) for the entire segment, shown in Figure 3.4, demonstrate similar structure and excellent agreement between ACATS and CPL. The mean difference in extinction (CPL - ACATS) for the bins in which both instrument mean profiles are “in cloud” is 22 percent. The integral of the mean extinction through the cirrus layer (i.e. mean cloud optical depth) is 2.373 for ACATS, which agrees with CPL (2.291) to within 3 percent. Additionally, error bars exhibit uncertainties in the ACATS HSRL-derived extinction 25-50 percent lower compared to the CPL extinction retrievals.

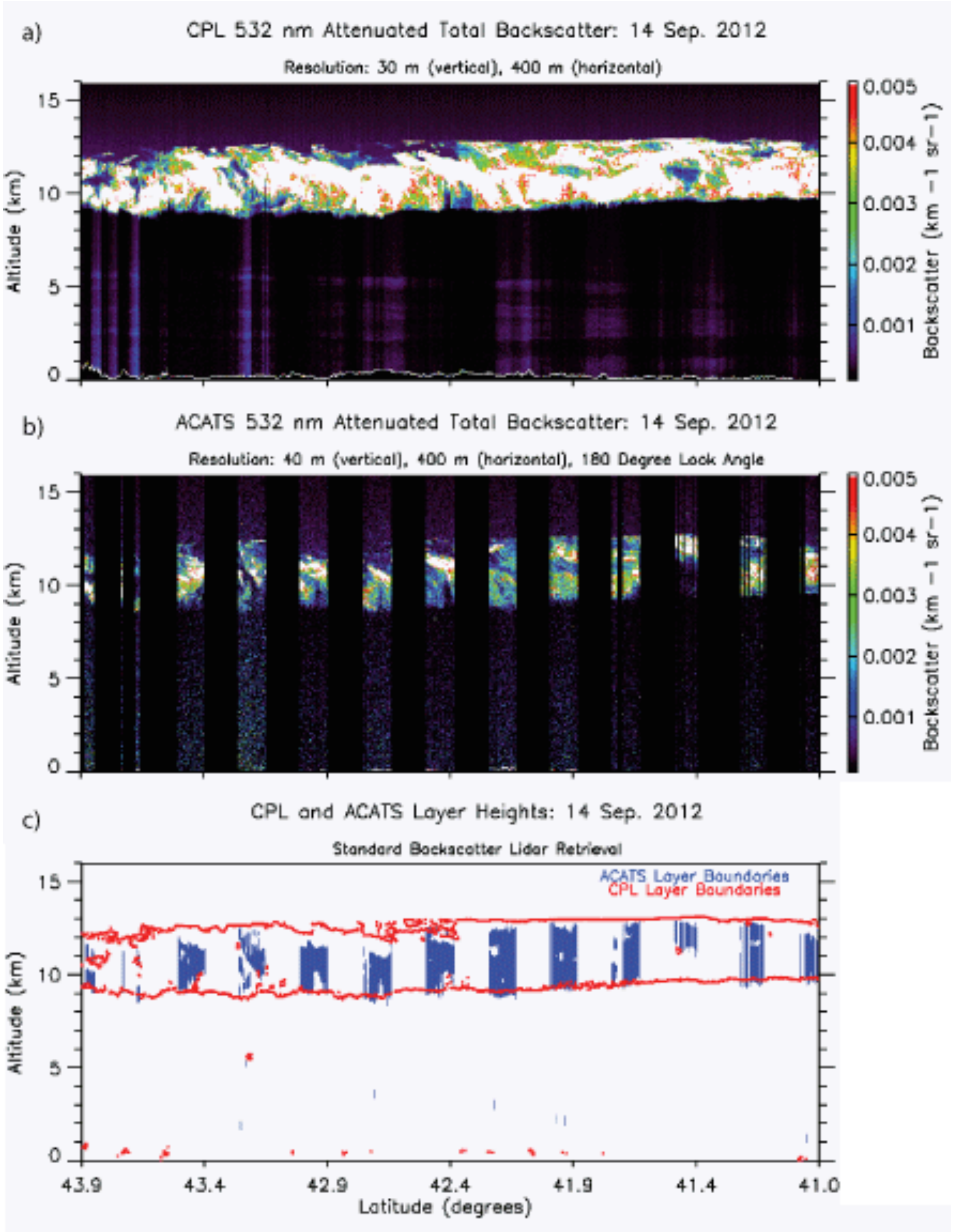

**Figure 3.2**. The 532 nm Attenuated Total Backscatter (km$^{-1}$ sr$^{-1}$) for CPL (a) and ACATS computed using the standard method (b) at the 180-degree look angle for a 27 minute segment of the ER-2 flight on 14 September. The layer boundaries for both instruments (c) show a cirrus layer between 9 and 13 km.

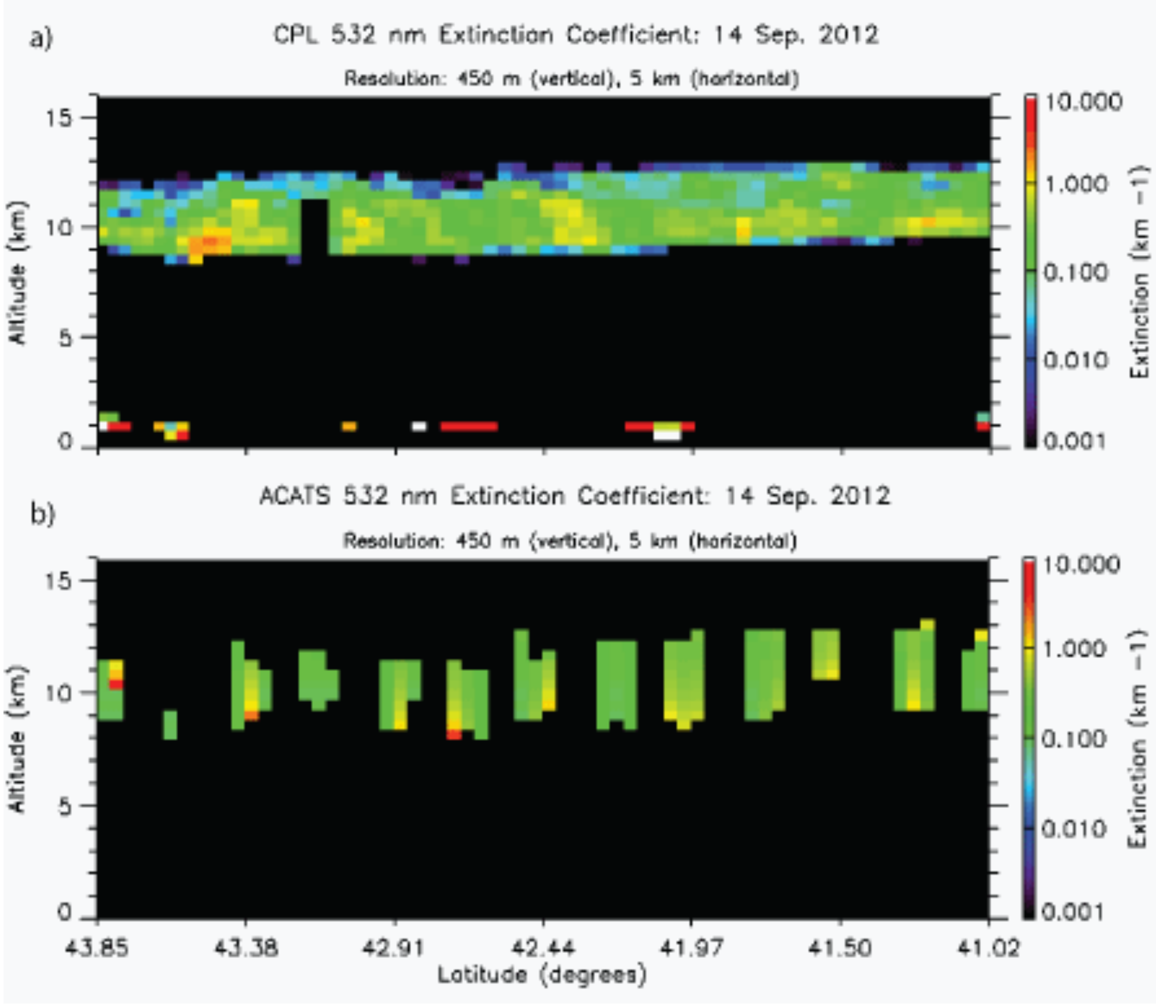

**Figure 3.3**. The 532 nm Extinction Coefficient (km$^{-1}$) for CPL (a) and ACATS computed using the HSRL method (b) at the 180-degree look angle for the same 14 September segment (Figure 3.2). The CPL extinction is averaged to 450 m vertical and 5 km horizontal, to match the ACATS HSRL resolutions.

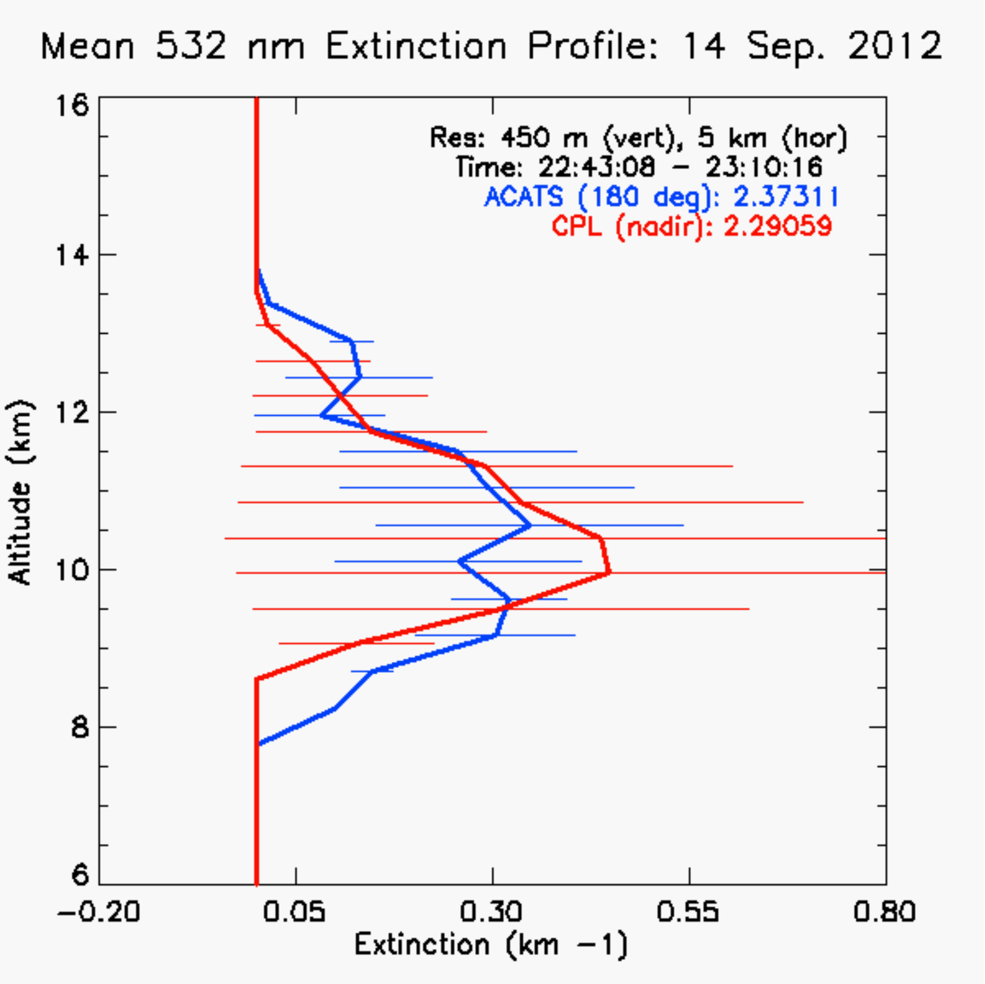

**Figure 3.4**. The mean profiles of 532 nm Extinction Coefficient (km$^{-1}$) for CPL (red) and ACATS computed using the HSRL method (blue) at the 180-degree look angle for the entire 27-minute 14 September cirrus segment in Figure 3.2. The error bars represent the mean uncertainty in extinction for each vertical bin of the mean profile.

The aerosol segment analyzed on 26 Sept. exemplifies good agreement between CPL and ACATS during nighttime for an elevated smoke layer with embedded water clouds. This segment was acquired over Montana between -106.4 and -113.4 degrees longitude as the aircraft flew west during local nighttime hours. ACATS was operating at all four look angles during this flight, collecting data for 60 seconds before rotating to the other look angles and returning 180 seconds later. Only the 0-degree look angle is compared to the CPL data, since the 180-degree ACATS data is of poor quality due to reduced telescope alignment. For this segment a 77 second time offset was used, corresponding to a range from the aircraft of 15.4 km (approximate altitude of 4.6 km). As observed in the CPL (a) and ACATS (b) 532 nm ATB for the segment (Figure 3.5), highly attenuating water clouds are observed near the top of the aerosol layer between -106.4 and -109.9 degrees longitude. The layer boundaries are plotted for the segment in Figure 3.5c. The ACATS layer boundaries (blue) are in good agreement with CPL layer boundaries (red) for both the aerosol layer and the water clouds.

Figure 3.6 shows the extinction coefficient at 532 nm from both 5 km CPL data (a) and 5 km ACATS HSRL data (b) for the 26 Sept. aerosol segment, averaged to 450 m vertically. Both instruments observe a relatively homogeneous aerosol layer, with more variability in extinction when water clouds are observed. The mean extinction profile for ACATS (blue) is 0.10 to 0.20 $km^{-1}$ higher than CPL (red) below 4 km, as shown in Figure 3.7. The higher values of ACATS extinction around 3.5 km are dominated by the high extinction at the bottom of the aerosol layer around -108.5 degrees longitude in Figure 3.6b. The ACATS backscatter image (Figure 3.5b) shows high backscatter in the middle of the aerosol layer around 3.5 to 4 km not present in the CPL backscatter image (Figure 3.5a). It is possible the two instruments are seeing slightly different scenes. Similar to the cirrus case on 14 Sept., the extinction uncertainty in the ACATS HSRL technique is as much as 50 percent lower than the CPL retrievals in the aerosol layer. The integral of the mean extinction for the entire segment (i.e. mean column optical depth) is 2.021 for ACATS, about 16 percent higher than the value of 1.704 for CPL.

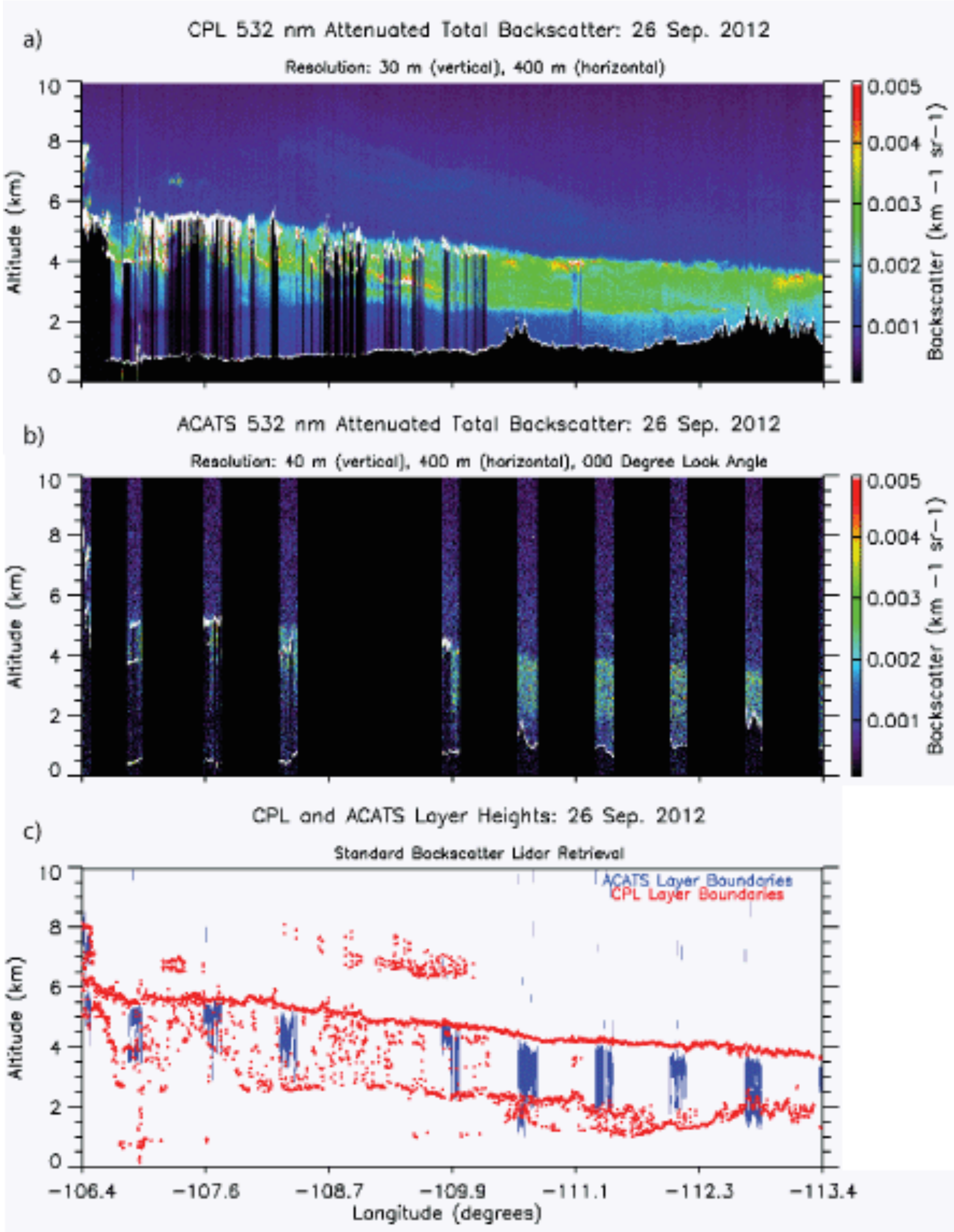

**Figure 3.5**. The 532 nm Attenuated Total Backscatter (km$^{-1}$ sr$^{-1}$) for CPL (a) and ACATS computed using the standard method (b) at the 0-degree look angle for a 44-minute segment of the ER-2 flight on 26 September. The layer boundaries for both instruments (c) show a smoke layer between 2 and 5 km.

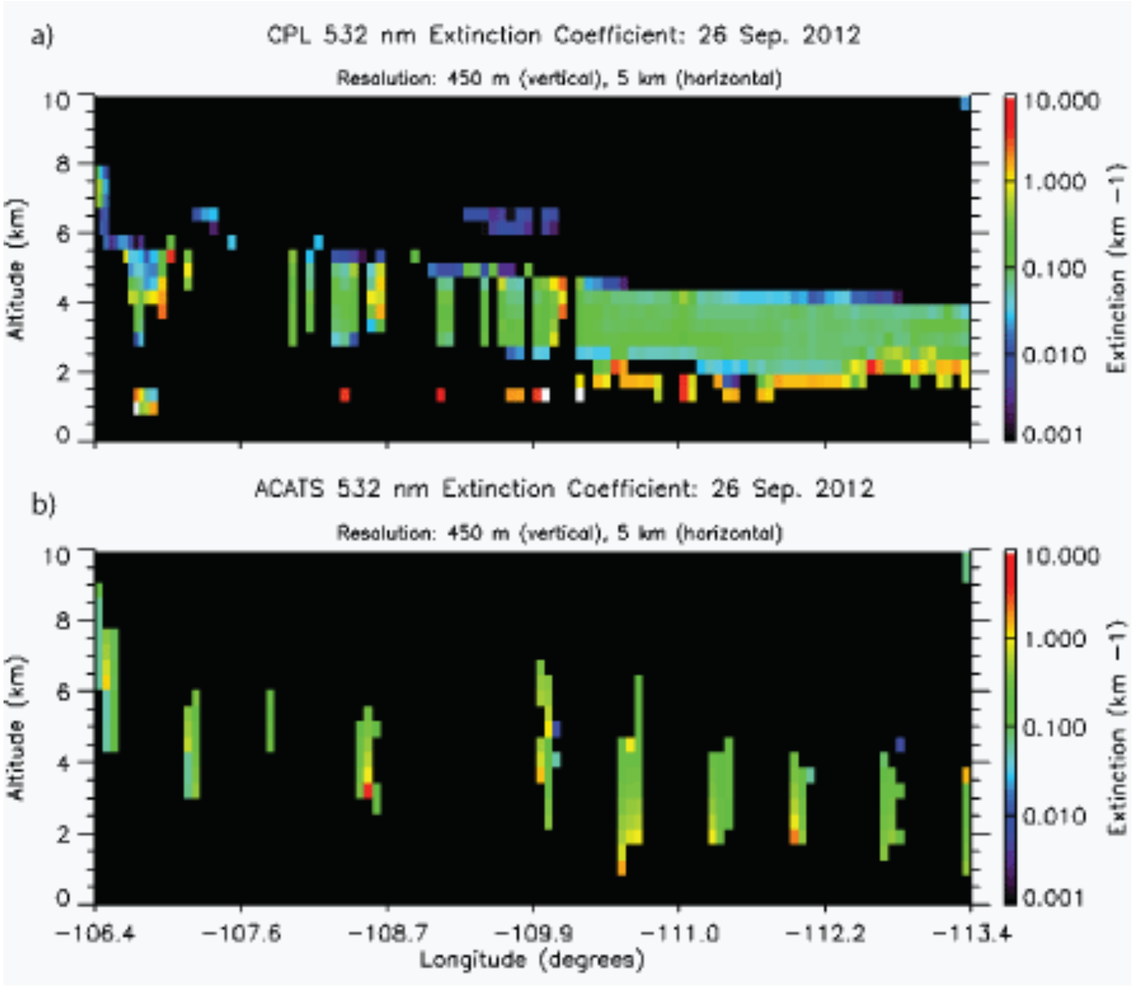

**Figure 3.6**. The 532 nm Extinction Coefficient (km$^{-1}$) for CPL (a) and ACATS computed using the HSRL method (b) at the 0-degree look angle for the same 26 September segment (Figure 3.5). The CPL extinction is averaged to 450 m vertical and 5 km horizontal, to match the ACATS HSRL resolutions.

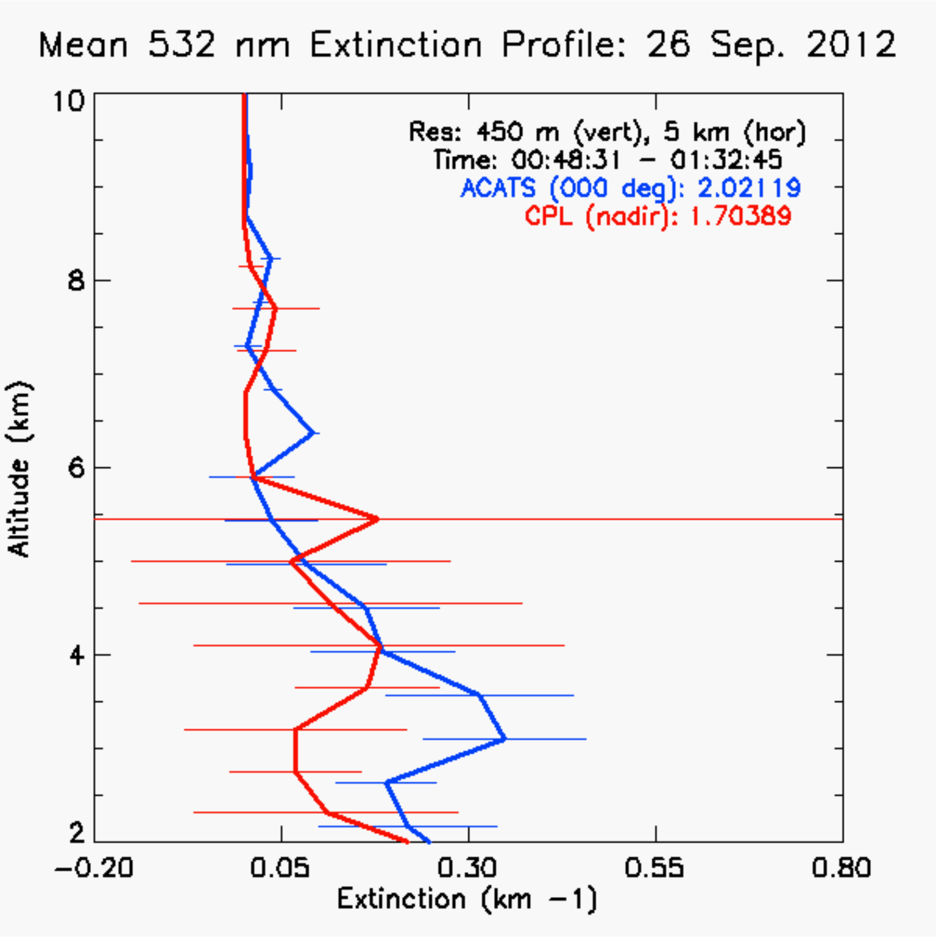

**Figure 3.7**. The mean profiles of 532 nm Extinction Coefficient (km$^{-1}$) for CPL (red) and ACATS computed using the HSRL method (blue) at the 0-degree look angle for the entire 44-minute 26 September smoke segment in Figure 3.5. The error bars represent the mean uncertainty in extinction for each vertical bin of the mean profile.

The final segment analyzed in this study is also from the 26 Sept. flight and characterizes agreement between CPL and ACATS during nighttime for a complex atmospheric scene. This segment was collected over North Dakota and Montana between -100.2 and -105.9 degrees longitude, just prior to the previous case. Similar to the aerosol case, only the 0-degree look angle is compared to the CPL data. For this segment a 55 second time offset was used, corresponding to a range from the aircraft of 11.0 km (approximate altitude of 9.0 km). The CPL 532 nm ATB image (Figure 3.8a) demonstrates the complex nature of this scene. Optically thin cirrus clouds between 8 and 11 km are observed above an elevated smoke layer between -100.23 and -102.12

degrees longitude and a mix of smoke and water clouds between -103.06 and -105.90 degrees. The thin cirrus is often broken in nature, as observed in both the ACATS and CPL ATB images around -101.6 degrees. Despite the complexity of the scene, there is relatively good agreement in layer boundaries for the cirrus clouds (Figure 3.8c). However, the ACATS layer detection algorithms do not detect the more optically thin smoke layer at the standard backscatter resolutions due to the weaker SNR and ATB.

The 532 nm extinction coefficient from this complex scene for both 5 km CPL data (a) and 5 km ACATS HSRL data (b) are plotted in Figure 3.9. The additional averaging allows the ACATS layer detection algorithm to identify the optically thin smoke layer between -100.30 and -102.15 degrees. The mean extinction profile (Figure 3.10) for ACATS (blue) and CPL (red) are in good agreement for most of the profile. However, the mean difference in extinction (CPL – ACATS) is 37 percent largely due to disagreement between 7 and 8 km. The images of CPL ATB (Figure 3.8a) and extinction (Figure 3.9a) show about a 0.5 km vertical separation between the cloud layers observed around -105 degrees longitude. However, due to the averaging required to compute ACATS HSRL properties these layers are combined into one layer of large vertical extent (Figure 3.9b). The more pronounced presence of this effect in the ACATS data is a consequence of the total number of vertical bins averaged to achieve a vertical resolution of 450 m. A total of 20 ACATS vertical bins (about 22 m each) are used to integrate to 450 m as opposed to 15 of the 30 m CPL vertical bins. As a result, the ACATS and CPL extinction profiles are different between 7 and 8 km. The mean ACATS optical depth (2.439) is about 18% higher than CPL (2.013), a consequence of the retrieval uncertainties in a complex atmospheric scene.

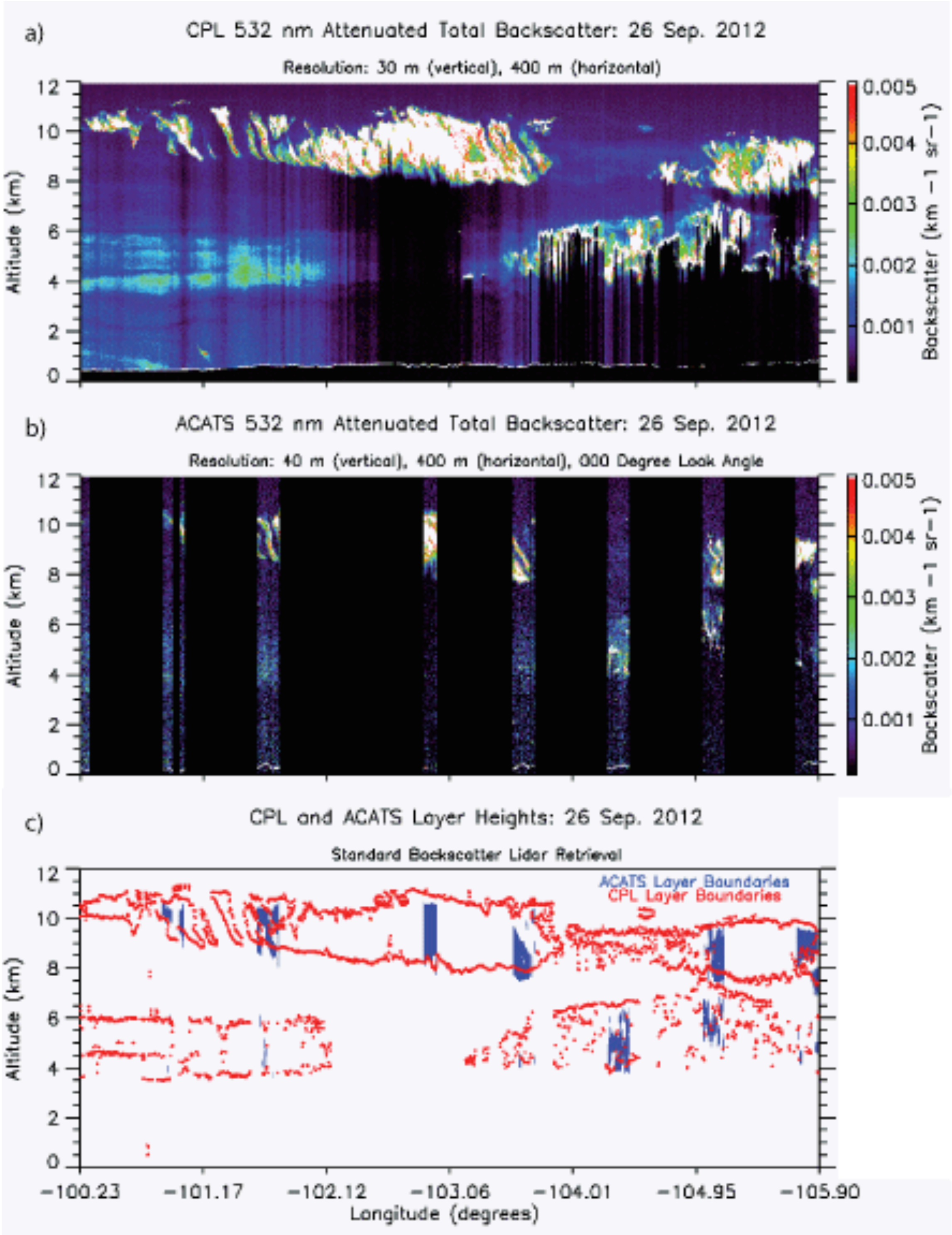

**Figure 3.8**. The 532 nm Attenuated Total Backscatter (km$^{-1}$ sr$^{-1}$) for CPL (a) and ACATS computed using the standard method (b) at the 0-degree look angle for a 34-minute segment of the ER-2 flight on 26 September. The layer boundaries for both instruments (c) show a complex scene with cirrus, water clouds, and smoke.

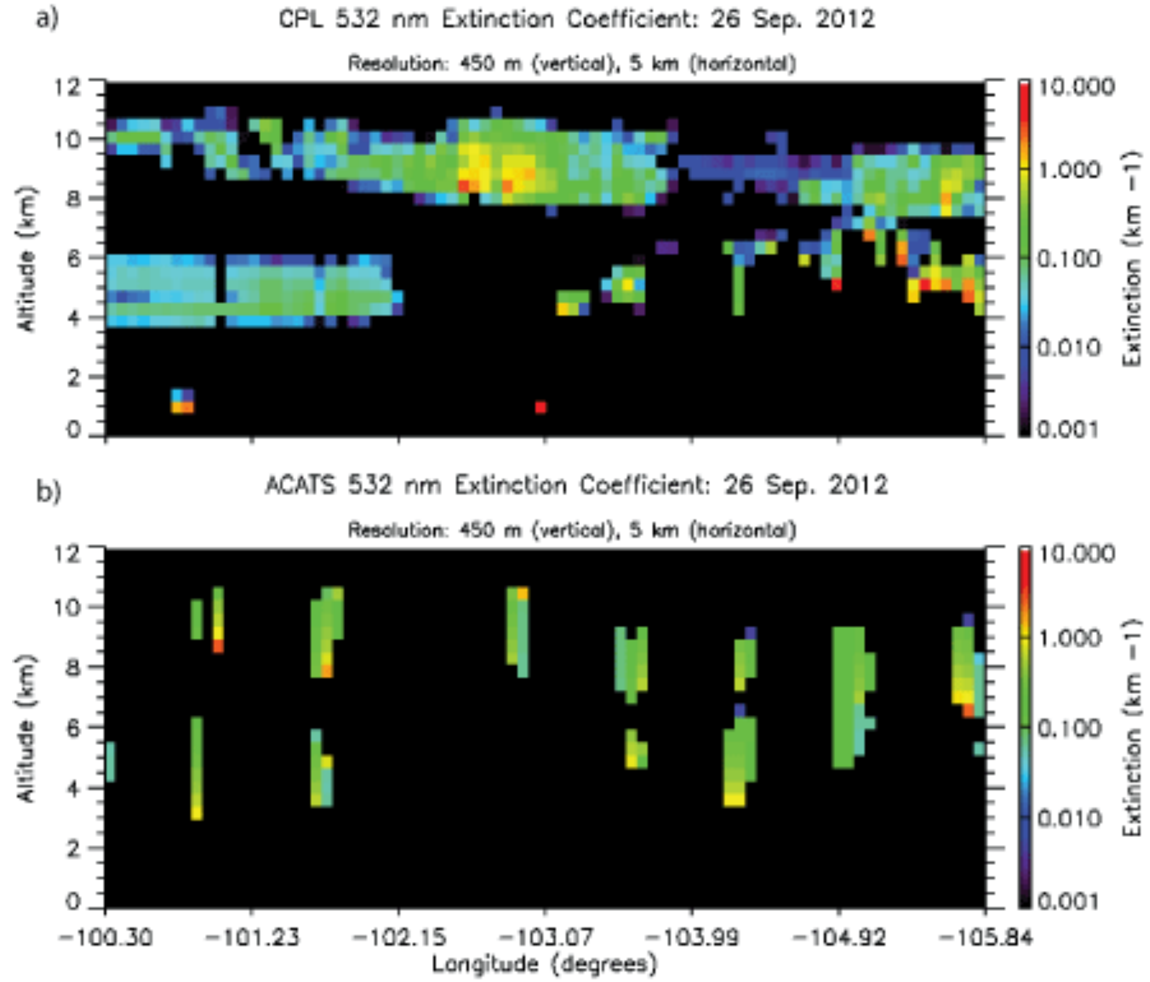

a) CPL 532 nm Extinction Coefficient: 26 Sep. 2012

Resolution: 450 m (vertical), 5 km (horizontal)

b) ACATS 532 nm Extinction Coefficient: 26 Sep. 2012

Resolution: 450 m (vertical), 5 km (horizontal)

**Figure 3.9**. The 532 nm Extinction Coefficient (km$^{-1}$) for CPL (a) and ACATS computed using the HSRL method (b) at the 0-degree look angle for the same 26 September segment (Figure 3.8). The CPL extinction is averaged to 450 m vertical and 5 km horizontal, to match the ACATS HSRL resolutions.

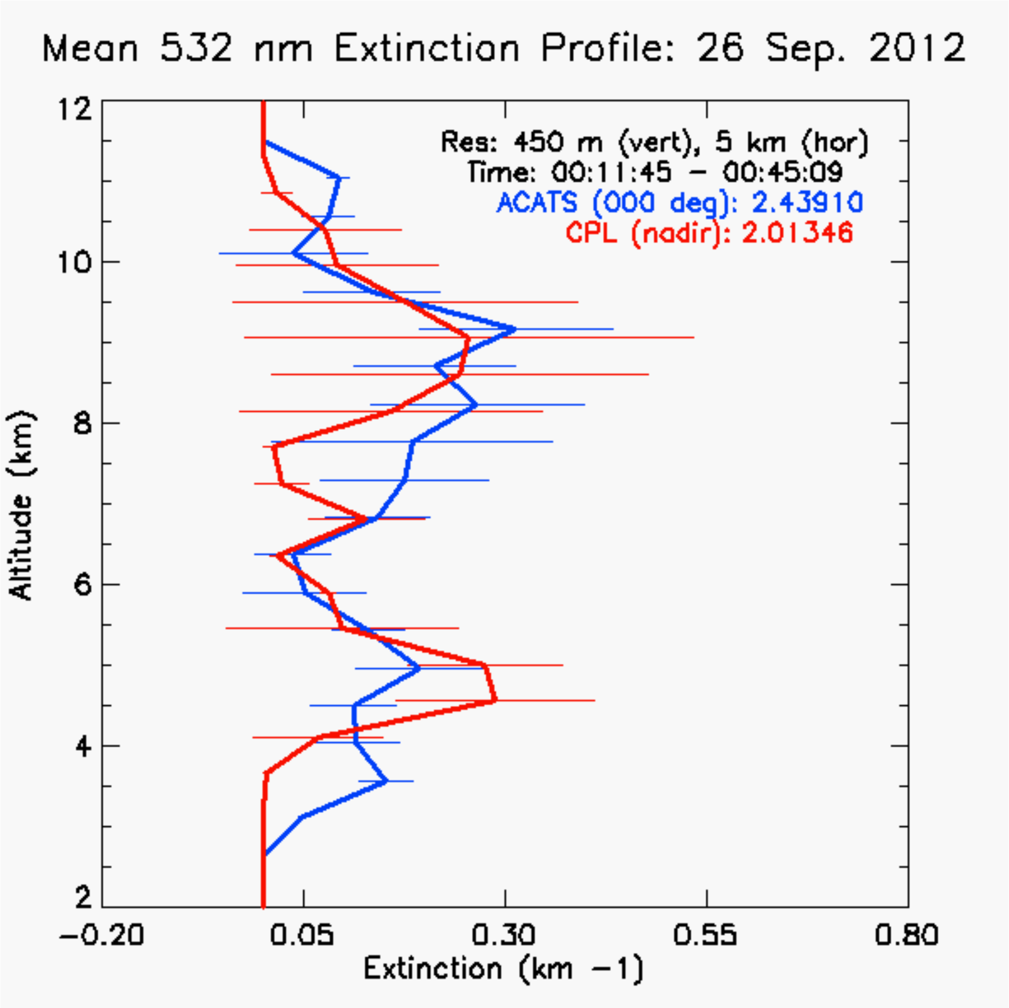

**Figure 3.10**. The mean profiles of 532 nm Extinction Coefficient (km$^{-1}$) for CPL (red) and ACATS computed using the HSRL method (blue) at the 0-degree look angle for the entire 34-minute 26 September complex scene in Figure 3.8. The error bars represent the mean uncertainty in extinction for each vertical bin of the mean profile.

ACATS 532 nm lidar ratios can be resolved independently for each 5 km HSRL profile and range bin, with no assumption about the layer type required. Although the lidar ratio cannot be derived at each range bin using CPL data, the lidar ratio for a transparent cloud or aerosol layers can be estimated at 532 and 1064 nm using optical depth estimates obtained from analysis of clear air regions immediately above and below the cirrus layer (determined from attenuation of Rayleigh and aerosol scattering, and using the integrated backscatter). This approach to directly determining the layer optical depth and lidar ratio without assumption of aerosol climatology is known as the transmission loss method (Young 1995; Yorks *et al.* 2011a). CPL 532 nm layer lidar ratios computed at the standard horizontal (200 m) and vertical (30 m) resolutions using the transmission loss method are compared to ACATS HSRL 532 nm lidar ratios computed for each 5 km profile and 450 m bin for WAVE flights, looking specifically at thin cirrus clouds. Figure 3.11 shows the frequency distributions of 532 nm lidar ratio for ACATS vertical bins (blue) within cirrus clouds and CPL cirrus cloud layers (red) only for flights in which ACATS collected robust cirrus data. The mean, median, and standard deviation for these same flights are shown in Table 3.2. There is more variability in the ACATS lidar ratios compared to CPL, illustrated by the higher tail in the ACATS distribution for lidar ratios greater than 30 sr (Figure 3.11) and higher standard deviation in the ACATS lidar ratios (Table 3.2). This higher variability in the ACATS retrievals is likely due to the variability of cloud physics within the cirrus clouds, since the ACATS lidar ratio is retrieved at every vertical bin.

**Table 3.2.** Lidar ratio statistics at 532 nm for the WAVE project.

| Instrument | Obs | Mean | Median | Std. Dev. |
|---|---|---|---|---|
| **ACATS** | 938 | 26.52 | 24.17 | 13.83 |
| **CPL** | 8581 | 24.55 | 22.00 | 10.19 |

Both the ACATS and CPL frequency distributions have a peak around 18 sr (Figure 3.11). The ACATS and CPL mean lidar ratios are 26.52 ± 13.83 and 24.55 ± 10.19 sr, respectively. Yorks *et al.* (2011a) found a mean lidar ratio of 27.23 ± 10.56 sr and a peak in the frequency distribution centered around 25.0 sr for transparent cirrus layers using all CPL data between 2003 and 2007. The mean and peak of the frequency distribution for the WAVE project derived by both instruments are lower than those previously measured but are similar to those observed during the The Observing System

Research and Predictability Experiment (THORPEX; Shapiro and Thorpe 2004) Atlantic campaign (Yorks *et al.* 2011a), implying lower COD or higher cloud albedo. Since the WAVE and THORPEX-Atlantic flights were over the mid-latitudes and the projects were conducted during fall/winter months, results for these synoptically-generated cirrus clouds are likely different than the other projects in which ice particles formed due to the rapid upward motions of convection.

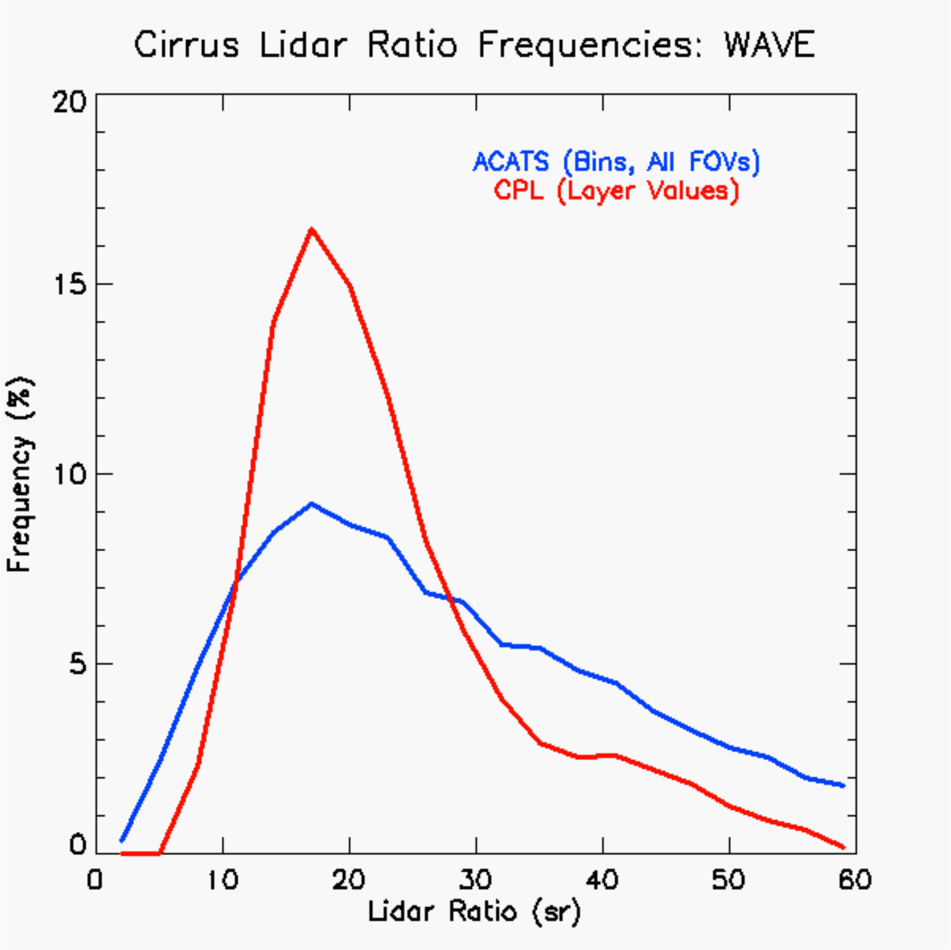

**Figure 3.11**. The frequency distribution of 532 nm lidar ratio (sr) for CPL (red) and ACATS computed using the HSRL method (blue) at the 0-degree look angle for transparent cirrus layers observed during flights in which ACATS collected quality measurements. Only CPL layer lidar ratios computed using the transmission loss method are used in the statistics, while ACATS lidar ratios are computed for each vertical bin.

Coincident ACATS and CPL during the WAVE campaign included observations of thin cirrus clouds and smoke layers, providing an excellent opportunity to assess the performance of the ACATS standard backscatter and HSRL retrievals. Although ACATS points off-nadir at 45 degrees and rotates, the ACATS fore and aft look angles observe nearly the same atmospheric scenes as CPL with a time-offset that is range dependent. I identified three 25-45 minute case study segments with thin cirrus layers, aerosol layers, and complex atmospheric scenes. Attenuated total backscatter derived using the ACATS standard backscatter technique show similar structure compared to the coincident CPL images for all cases. Additionally, layer boundaries are in excellent agreement for cirrus cloud base and more optically thick parts of cirrus clouds. I found excellent agreement between ACATS and CPL extinction profiles (22%) and mean COD (3%) for a homogeneous thin cirrus layer. The ACATS HSRL-derived extinction uncertainties are 25 to 60 percent lower than the extinction uncertainties derived by CPL, demonstrating the advantage of the HSRL technique and the need for more HSRL measurements of cirrus properties. Both the ACATS HSRL-derived and CPL layer-derived 532 nm lidar ratio frequency distributions have a peak around 18 sr, lower than those previously measured but are similar to those observed during the THORPEX-Atlantic campaign (Yorks *et al.* 2011a). Since the WAVE flights were over the mid-latitudes and conducted during September, these lower lidar ratios suggest that there is a relationship between cirrus properties and generation mechanism. This relationship will be explored in the next chapter.

# Chapter 4: Investigation of Cirrus Properties and Formation Mechanisms

A top priority in current climate change research is to provide measurements of cirrus properties to test and improve cloud parameterizations in climate models. There are still lingering questions as to the relationship between cirrus properties and dynamic cloud generation mechanisms. In this chapter, statistics of CPL cirrus layer properties are compiled from more than 700 ER-2 and Global Hawk flight hours over the mid-latitudes and tropics. Statistics of CPL cirrus clouds properties, such as lidar ratio, depolarization ratio, backscatter color ratio, and COD are compiled for clouds formed in the mid-latitudes, especially cirrus formed as a result of synoptic-scale uplift. The trends and values of synoptically-generated cirrus properties are compared to those formed due to the rapid vertical motions of convection in the tropics. Similar statistics are computed using CALIOP data to determine if the relationships between cirrus optical properties and dynamic generation mechanisms determined from CPL are observed on a global scale.

## 4.1 Cirrus Data Sources

In this study, I analyzed CPL data from 11 field campaigns that cover a range of meteorological seasons and geographic locations throughout North and Central America. A full list of the projects included in this study is found in Table 4.1. The flights over mid-latitudes include cases from the Polarimeter Definition Experiment (PODEX), Studies of Emissions and Atmospheric Composition, Clouds and Climate Coupling by Regional Surveys (SEAC$^4$RS), THORPEX-Atlantic, and WAVE field campaigns, which occurred between September and April, providing opportunity to investigate synoptically-generated cirrus using CPL data. The CPL retrieved properties of synoptically-generated cirrus are compared to convectively-generated and tropical tropopause layer (TTL) cirrus. Many recent field campaigns dedicated individual flights to observations of tropical cirrus formed through convection, such as the Tropical Composition, Cloud and Climate Coupling mission (TC4; Toon *et al.* 2010), the Airborne Tropical Tropopause Experiment (ATTREX; Jensen *et al.* 2013), and SEAC$^4$RS. Additionally, the Hurricane and Severe Storms Sentinel (HS3) flights over Atlantic Ocean tropical storm systems provide additional observations of tropical cirrus formed through the rapid upward motions of convection. Other projects, such as the Cloud and Land Surface Interaction Campaign (CLASIC; Miller 2008) and the CALIPSO-CloudSat Validation Experiment (CC-VEX; McGill *et al.* 2007) were conducted in the lower mid-latitudes (30-35 N) with the purpose of observing cumulus convection and cirrus clouds.

The CPL cirrus layer properties analyzed in this study include layer-integrated values of depolarization ratio and backscatter color ratio, as well as layer lidar ratio and optical depth. As discussed in Chapter 3, the CPL lidar ratios can be directly derived for transmissive cloud/aerosol layers using the transmission loss method (Yorks *et al.* 2011a). Young *et al.* (2013) demonstrated that for layers in which the ratio of particulate backscatter coefficient to molecular backscatter coefficient is large, the uncertainty in the constrained lidar ratio is equal to the uncertainty in the calibration constant. The layer-integrated depolarization ratio ($\delta_{\text{layer}}$) was calculated separately from the standard CPL data products using the equation:

$$\delta_{layer} = \frac{\sum_{\text{top}}^{\text{base}} \gamma'_{1064\perp}(z)}{\sum_{\text{top}}^{\text{base}} \gamma'_{1064\parallel}(z)} \qquad \text{Eq. 4.1}$$

which can be described as the ratio of perpendicular polarized 1064 nm layer-integrated total attenuated backscatter coefficient to parallel polarized 1064 nm layer-integrated total attenuated backscatter coefficient. There are two main sources of error in the CPL layer-integrated depolarization ratio. The first source is a result of the determination of the relative calibration for the individual 1064 nm detectors, known as the depolarization gain ratio (Liu *et al.* 2004; Hu *et al.* 2006), estimated to be less than 3% (Liu *et al.* 2004). Another source of error is the 3% cross-talk measured in the CPL receiver subsystem. The layer-integrated backscatter color ratio ($\chi_{\text{layer}}$) is also calculated separately from the standard CPL data products using the ratio of 1064 nm layer-integrated particulate backscatter coefficient to 532 nm layer-integrated particulate backscatter coefficient with the equation:

$$\chi_{layer} = \frac{\sum_{\text{top}}^{\text{base}} \beta_p^{1064}(z)}{\sum_{\text{top}}^{\text{base}} \beta_p^{532}(z)} \qquad \text{Eq. 4.2}$$

The uncertainties in the color ratio result from uncertainties in the calibration constant that arise from a combination of signal noise and the assumption of clear-air molecular scatter (Campbell *et al.* 2008; Vaughan *et al.* 2010). The layer-integrated depolarization ratio and color ratio are computed for each transparent cloud layer detected in the CPL data in which the lidar ratio was calculated using the transmission loss technique, with a horizontal resolution of 200 m.

Two case studies are presented here in which coincident measurements of cirrus microphysical properties from the Research Scanning Polarimeter (RSP; Cairns *et al.*

2003) are used to complement the CPL data. RSP is an airborne polarimeter capable of measuring the total and polarized reflectance simultaneously using 9 bands in the visible and shortwave infrared (Cairns *et al.* 2003). The instrument scans 152 different view angles at intervals of 0.8 degrees along the aircraft track. RSP simultaneously flew aboard the ER-2 with the CPL during multiple projects, including PODEX and SEAC$^4$RS. Cirrus microphysical properties including optical thickness, effective ice crystal size, particle aspect ratio (ratio of length to width), and particle roughness parameter are retrieved from the RSP multi-angle reflectance (van Diendenhoven *et al.* 2013). The RSP retrievals of aspect ratio and particle roughness parameter can be used to estimate the first moment of the scattering phase function, known as the asymmetry parameter (van Diendenhoven *et al.* 2012). The asymmetry parameter (g) is defined as (Macke *et al.* 1996):

$$g = \int_0^{\pi} P_{tot}(\Theta)\cos(\Theta)\sin(\Theta)d\Theta \qquad \text{Eq. 4.3}$$

where $P_{tot}$ is the normalized scattering phase function and $\Theta$ is scattering angle. Recently, van Diendenhoven *et al.* (2013) compared RSP retrievals of asymmetry parameter to the Cloud Integrating Nephelometer (CIN) and found an accuracy of about 5 %. Furthermore, RSP ice particle shape and roughness retrievals are correctly identified (van Diendenhoven *et al.* 2012).

In situ measurements are also available for case study analysis from the 2D-S ice particle probe (Lawson *et al*. 2006b) and a CPI (Lawson *et al.* 2001) that flew as payloads on the SPEC Learjet during the SEAC$^4$RS project. The 2D-S instrument is an optical imaging probe capable of measuring particles as small as 8 μm at aircraft speeds of over 200 $ms^{-1}$ with the ability to remove large ice particle shattering effects (Lawson *et al.* 2006b). Since the Learjet did not fly the exact same track as the ER-2, these measurements are not exactly coincident with the CPL and RSP measurements, but were collected within minutes of the ER-2 data for specific flights. Parameters such as ice water content (IWC), ice particle concentration, ice particle extinction, and size distributions from the 2D-S complement the remote sensing retrievals. The CPI provides high-resolution digital images of ice particles as they pass through the instrument during flight, with a pixel resolution of 2.3 μm. The particle size and habits types identified in the CPI images are shown in Figure 1.1 (Lawson *et al.* 2006a) and will be referenced throughout this section.

**Table 4.1.** List of CPL field campaign data to be used in this study.

| Project | Dates | Latitude Range |
|---|---|---|
| THORPEX-Atlantic | Nov - Dec 2003 | 32 to 53 |
| CC-VEX | Jul - Aug 2006 | 23 to 39 |
| CLASIC | Jun 2007 | 28 to 40 |
| TC4 | Jul - Aug 2007 | 0 to 39 |
| ATTREX11 | Nov 2011 | 6 to 28 |
| IceAx | Apr 2012 | 31 to 80 |
| WAVE | Sep 2012 | 33 to 48 |
| PODEX | Jan - Feb 2013 | 28 to 38 |
| ATTREX13 | Feb - Mar 2013 | -10 to 33 |
| HS3 | Aug - Sep 2013 | 10 to 38 |
| SEAC$^4$RS | Aug - Sep 2013 | 15 to 49 |

## 4.2 Cirrus Case Studies

Optically thin cirrus generated from synoptic scale uplift was observed on 22 Jan. 2013 during the PODEX project. The ER-2 flew a race-track pattern around the Central Valley of California targeting this cirrus, which formed due to synoptic-scale uplift ahead of an upper-level trough approaching the Pacific Northwest. This cloud was not associated with any deep convection. Figure 4.1 shows the CPL 1064 nm depolarization ratios for the second half of the 22 Jan. flight (20:38:53 to 23:35:43 UTC). Values of 1064 nm depolarization ratio for the optically thin cirrus between 10 and 13 km are less than 0.42 for almost all of the range bins within the cloud and the segment mean layer-integrated depolarization ratio is 0.38 ± 0.02. The mean cloud top temperature for the segment is -68 C. The mean layer-integrated backscatter color ratio for this case is 0.95 ± 0.08 (Table 4.2), showing that the backscatter at 532 nm is nearly the same as 1064 nm. The frequency distribution of CPL 532 nm lidar ratios for cirrus observed during this case is shown in Figure 4.2a and illustrates a normal distribution with very few values above 35 sr. The mean lidar ratio for this synoptically-generated cirrus over the mid-latitudes is 23.2 ± 4.7 sr, similar to the values found for the WAVE campaign using CPL and ACATS (Figure 3.11). Hereinafter, this case will be referred to as the "Mid-Latitude Case".

**Table 4.2.** Statistics of Cirrus Properties from CPL and RSP for the Mid-Latitude Case.

| Variable | Mean | Median | Std. Dev. | Min | Max |
|---|---|---|---|---|---|
| CPL Observations: | 8480 | | | | |
| Lidar Ratio (sr) | 23.23 | 22.84 | 4.73 | 8.09 | 58.74 |
| Depol. Ratio | 0.375 | 0.375 | 0.023 | 0.281 | 0.508 |
| COD (532) | 0.343 | 0.334 | 0.130 | 0.100 | 0.878 |
| COD (1064) | 0.349 | 0.339 | 0.143 | 0.057 | 2.241 |
| Color Ratio | 0.953 | 0.948 | 0.087 | 0.734 | 3.115 |
| Latitude | 36.16 | 36.20 | 0.85 | 34.56 | 37.87 |
| Longitude | -119.60 | -119.70 | 0.75 | -120.94 | -118.03 |
| Cloud Top Hgt (km) | 13.49 | 13.52 | 0.24 | 10.16 | 13.94 |
| Cloud Top Temp (C) | -68.24 | -68.60 | 1.66 | -69.20 | -43.20 |
| RSP Observations: | 376 | | | | |
| COD | 6.85 | 6.53 | 1.25 | 5.02 | 9.68 |
| Asymmetry Par. | 0.790 | 0.790 | 0.014 | 0.758 | 0.810 |
| Aspect Ratio | 0.436 | 0.435 | 0.047 | 0.363 | 0.560 |
| Roughness | 0.554 | 0.567 | 0.068 | 0.450 | 0.650 |
| Reff (2.25, μm) | 9.96 | 9.64 | 1.72 | 0.13 | 33.39 |
| Reff (1.59, μm) | 6.87 | 7.14 | 1.98 | 0.71 | 31.32 |

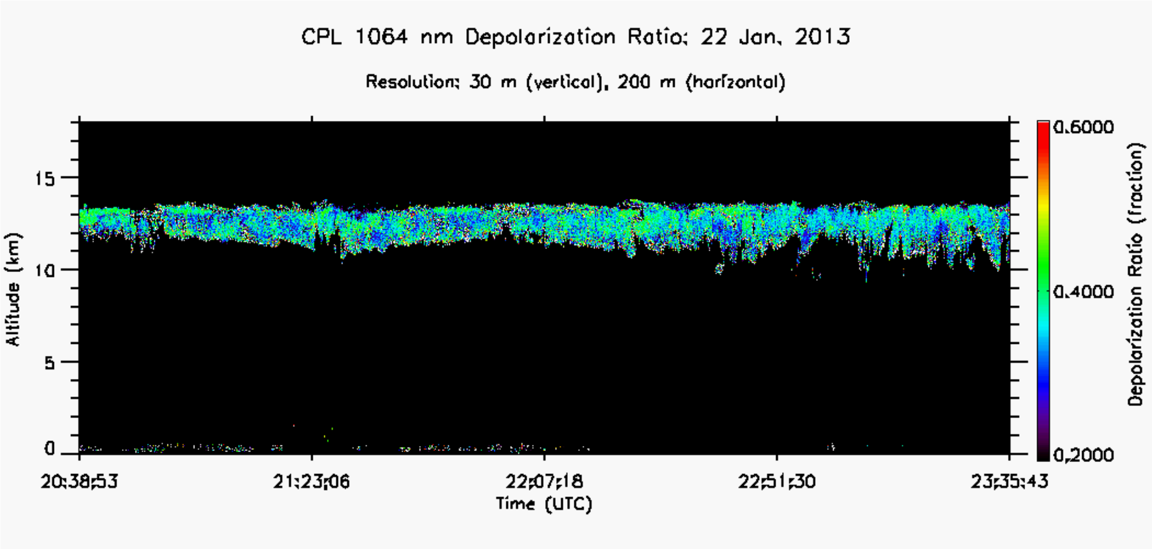

**Figure 4.1**. The CPL 1064 nm depolarization ratio for a cirrus cloud between 10 and 13 km observed during the 22 Jan. 2013 PODEX flight over the Central Valley of California. This cirrus is optically thin with COD less than 3.0.

Coincident measurements from RSP on 22 Jan. yield a median particle aspect ratio near 0.44 (Table 4.2). The particle habit can be generalized from the RSP retrieved aspect ratio and roughness into plate-like aggregates and column-like aggregates. These generalized habits are then used as a proxy for the retrieval of the asymmetry parameter (van Diendenhoven *et al.* 2012). For the Mid-Latitude Case, the RSP data demonstrate a mix of plate-like aggregates (45 percent) and rosettes/column aggregates (55 percent). Assuming most of the latter population consists of rosette shapes, these particle habits are consistent with Lawson *et al.* (2006), who found that irregulars and rosette shapes dominate mid-latitude cirrus habits. Unfortunately, the CPI and 2D-S instruments did not participate in the PODEX project. In situ measurements of mid-latitude cirrus indicate a high fraction of ice concentrations in the small (sub-100 μm) diameter size range (Heymsfield *et al.* 2002; Lawson *et al*. 2006a). Recent studies suggest that forward scattering spectrometer probe (FSSP; Knollenberg 1981) measurements of small ice particles in the presence of large ice particles are often contaminated with shattering artifacts (Field *et al.* 2003). However, RSP estimates of particle effective radius at the 1.59 and 2.25 micron bands, shown in Figure 4.2b, yield small particle sizes for Mid-Latitude Case. Most particles have an effective radius of less than 10 μm, consistent with the small particle mode (sub-100 μm size range) found by Heymsfield *et al.* (2002) and Lawson *et al.* (2006) for mid-latitude cirrus, suggesting that the shattering artifact does not substantively impact the results.

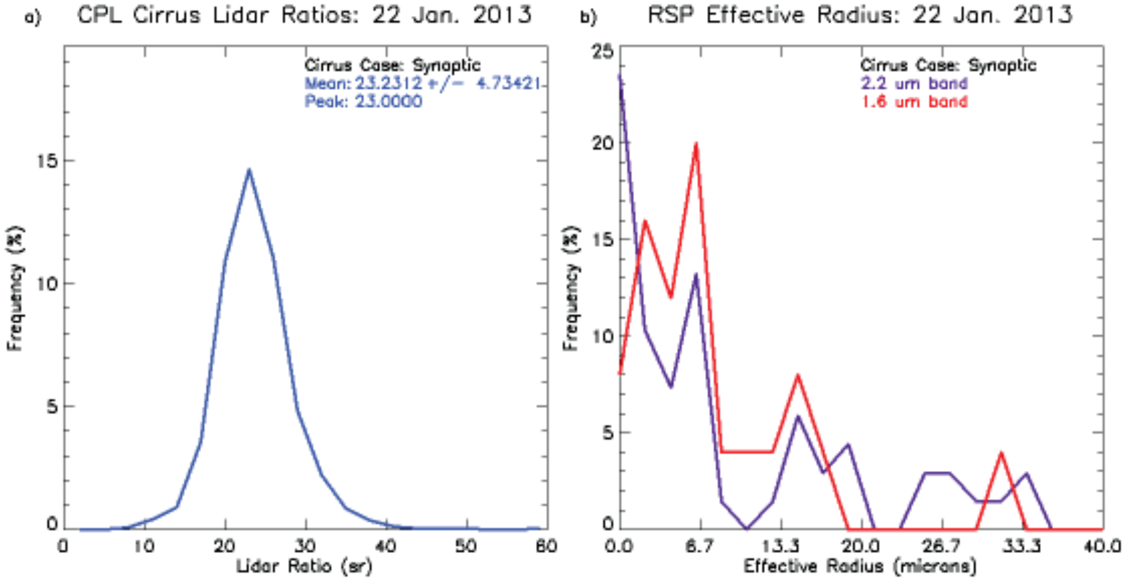

**Figure 4.2**. The CPL 532 nm lidar ratio frequency distribution (a) and RSP effective radius at the 2.2 micron (purple) and 1.6 micron (red) bands for the cirrus cloud observed during the 22 Jan. 2013 PODEX flight.

On 18 September 2013 the ER-2 targeted tropical cirrus associated with convective anvils as part of the SEAC$^4$RS campaign. The DC-8 (yellow) and Learjet (green) flew a pattern similar to the ER-2 (red) over the Gulf of Mexico, which included a racetrack pattern over cirrus between 15:40 and 16:43 UTC as demonstrated in Figure 4.3. Figure 4.4 shows the CPL 1064 nm depolarization ratios for the first part of the 18 Sept. flight, up to 16:43 UTC. CPL observed transparent cirrus between 9 and 13 km with a mean layer-integrated depolarization ratio of 0.40 ± 0.05 and values as high as 0.55 (Figure 4.4). These depolarization ratios are higher than the Mid-Latitude Case, despite a mean cloud top temperature for the segment (-52 C) warmer than the Mid-Latitude Case. Previous work has demonstrated an inversely proportional relationship between cirrus depolarization ratio and cloud temperature, meaning the depolarization ratio increases with decreasing temperature (Sassen and Benson 2001; Platt *et al.* 2002; Reichardt *et al.* 2002; Yorks *et al.* 2011a). This relationship exists because the depolarization ratio is related to ice particle shape, a function of cloud temperature (Mason *et al.* 1963). The mean color ratio (0.96 ± 0.13) for the 18 Sept. segment is nearly identical to the Mid-Latitude Case. However, the lidar ratio, as shown in Figure 4.5a, has a mean of 33.2 ± 12.1 sr, 10 sr higher than the Mid-Latitude Case and similar to the results of Yorks *et al.* (2011a) for the CLASIC and CC-VEX projects. Hereinafter, this 18 Sept. case will be referred to as the "Tropical Case".

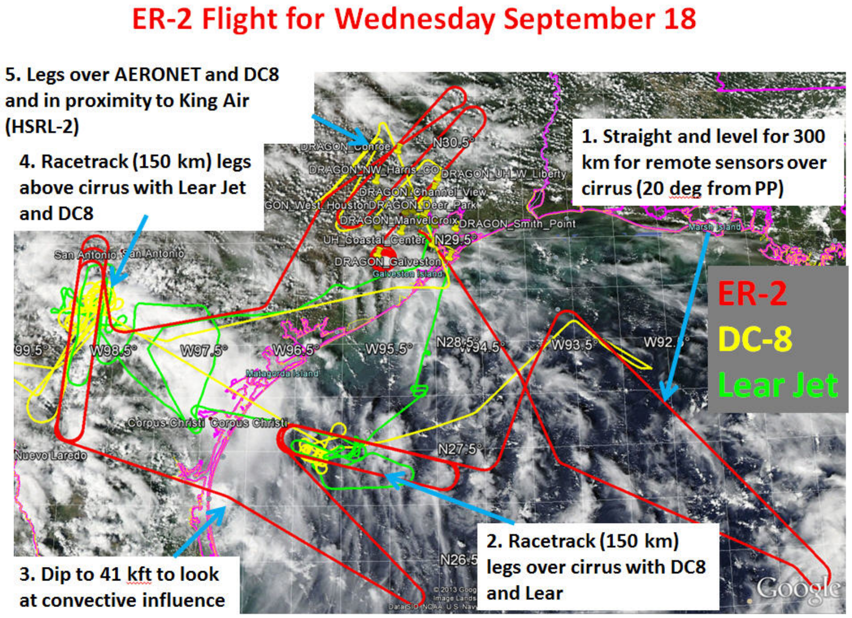

**Figure 4.3**. The aircraft flight tracks for the ER-2 (red), DC-8 (yellow) and Learjet (green) for the 18 September 2013 SEAC$^4$RS flight overlaid on top of the visible satellite imagery. All three aircraft observed anvil cirrus clouds.

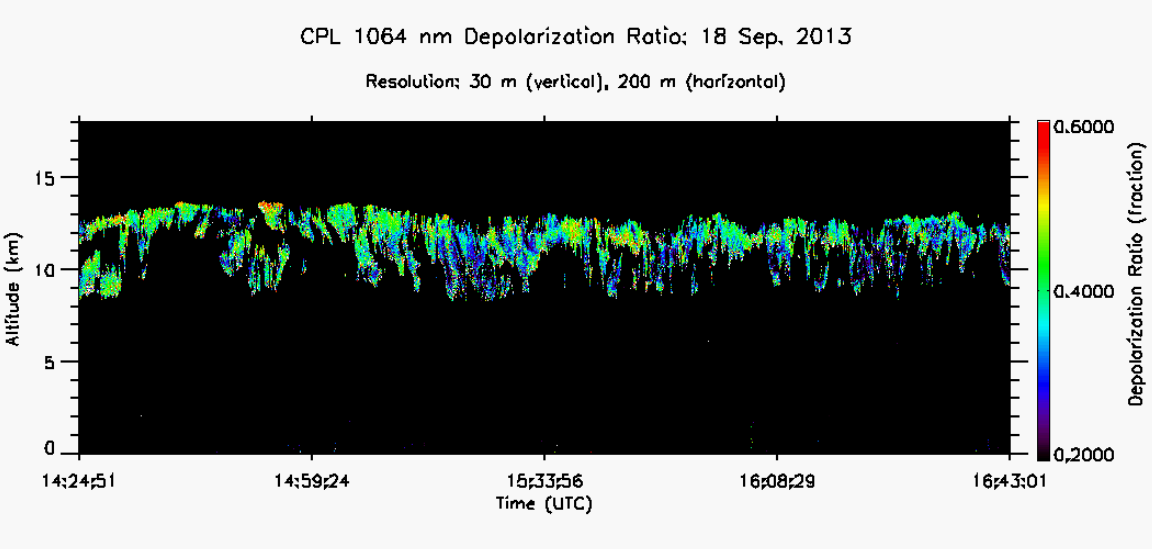

**Figure 4.4**. The CPL 1064 nm depolarization ratio for a cirrus cloud between 9 and 14 km observed during the 18 Sept. 2013 SEAC$^4$RS flight over the Gulf of Mexico.

Coincident measurements from RSP for the Tropical Case show a much higher frequency of plate-like aggregates (74 percent) than rosettes/column aggregates (26 percent) and nearly 30 percent more plate-like aggregates than the Mid-Latitude Case. Statistics of aspect ratio, roughness, and asymmetry parameter are shown in Table 4.3. Furthermore, RSP estimates of particle effective radius demonstrate the larger particle sizes observed in these convectively-generated cirrus, as shown in Figure 4.5b. Most particles have an effective radius greater than 10 μm, with a mean effective radius of 27 μm at the 2.25-micron channel (purple). CPI measurements in the same vicinity as the ER-2, shown in Figure 4.6, illustrates particle habits for a cloud at 15:38 UTC comprised mostly of large columns (a) and a cloud at 15:54 UTC comprised mostly of plate-like aggregates or irregulars (b). Figure 4.7 shows the CPI ice particle habit frequencies for the entire Tropical Case. Overall, columns/rosettes are found in 26 percent of observations, with most of the population dominated by large columns (22 percent). This is consistent with the RSP habit retrievals. Table 4.4 shows the mean ice concentrations, extinction and IWC for the entire Tropical Case. These anvil cirrus clouds exhibit mean ice concentrations (397 $L^{-1}$), extinction (1.65 $km^{-1}$) and IWC (0.044 g $m^{-3}$) similar to the results of Lawson *et al.* (2010) for fresh and aged anvil cirrus.

**Table 4.3.** Statistics of Cirrus Properties from CPL and RSP for the Tropical Case.

| Variable | Mean | Median | Std. Dev. | Min | Max |
|---|---|---|---|---|---|
| CPL Observations: | 2626 | | | | |
| Lidar Ratio (sr) | 33.18 | 31.13 | 12.08 | 8.04 | 60.00 |
| Depol. Ratio | 0.401 | 0.403 | 0.057 | 0.270 | 0.586 |
| COD (532) | 0.406 | 0.350 | 0.234 | 0.100 | 1.108 |
| COD (1064) | 0.398 | 0.344 | 0.241 | 0.042 | 1.818 |
| Color Ratio | 0.963 | 0.957 | 0.128 | 0.574 | 2.794 |
| Latitude | 27.42 | 27.49 | 0.67 | 26.15 | 28.70 |
| Longitude | -93.08 | -92.88 | 1.33 | -96.40 | -91.08 |
| Cloud Top Hgt (km) | 12.37 | 12.71 | 1.15 | 9.05 | 13.79 |
| Cloud Top Temp (C) | -52.42 | -55.70 | 9.41 | -63.10 | -25.25 |
| RSP Observations: | 5318 | | | | |
| COD | 10.43 | 8.21 | 6.81 | 5.00 | 100.00 |
| Asymmetry Par. | 0.787 | 0.784 | 0.034 | 0.710 | 0.956 |
| Aspect Ratio | 0.413 | 0.389 | 0.231 | 0.024 | 1.000 |
| Roughness | 0.561 | 0.595 | 0.135 | 0.000 | 0.700 |
| Reff (2.25, μm) | 27.26 | 27.52 | 8.82 | 1.25 | 58.87 |
| Reff (1.59, μm) | 23.14 | 23.96 | 8.91 | 1.07 | 53.76 |

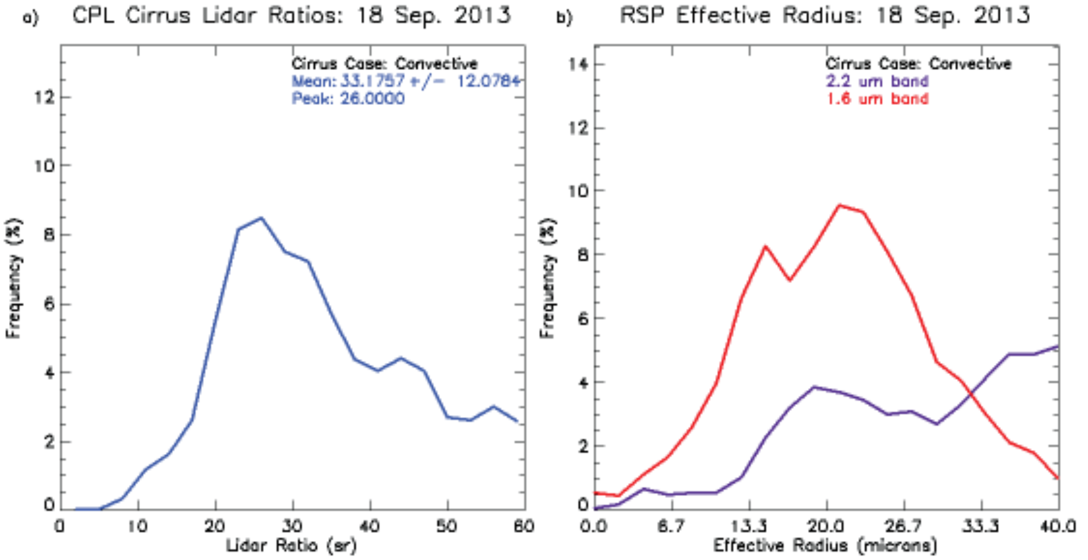

**Figure 4.5**. The CPL 532 nm lidar ratio frequency distribution (a) and RSP effective radius at the 2.2 micron (purple) and 1.6 micron (red) bands for the cirrus cloud observed during the 18 Sept. 2013 SEAC$^4$RS flight.

**Table 4.4.** Statistics of Cirrus Properties from the 2D-S for the Tropical Case.

| | **Concentration ($L^{-1}$)** | **Extinction ($km^{-1}$)** | **IWC ($g\ m^{-3}$)** |
|---|---|---|---|
| Mean | 397 | 1.652 | 0.044 |
| Median | 241 | 0.434 | 0.008 |
| Std. Dev. | 492 | 3.967 | 0.119 |
| Min | 0 | 0.001 | 0.000 |
| Max | 8488 | 38.290 | 1.180 |

I also analyzed other cases during the SEAC$^4$RS project with coincident RSP and CPI measurements. CPL and RSP cirrus properties for the SEAC$^4$RS flight over the Ozarks on 11 Sept. 2013 (blue) are nearly identical to the California Mid-Latitude Case (Table 4.5), and CPI retrievals for 11 Sept. indicate a high frequency of rosette shaped particles (not shown). These size and shape retrievals are consistent with previous in situ measurements of mid-latitude cirrus and the Mid-Latitude Case (Lawson *et al.* 2006a). The cirrus from 11 Sept. formed as a result of continental convection over the Ozark Plateau ahead of an approaching cold front, so the formation mechanism is likely a combination of synoptic-scale uplift and convective uplift. CPL and RSP cirrus properties for the SEAC$^4$RS flights on 2, 4, 13, and 16 September 2013 (red) are nearly identical to the Tropical Case (Table 4.5), with high mean lidar ratios and depolarization ratios. However, it is not clear whether these trends are due to the maritime/continental environment of this cirrus or dynamic formation mechanism.

**Table 4.5.** Statistics of Cirrus Properties from CPL and RSP for other SEAC$^4$RS cases.

| **Case** | **δ** | **Sp** | **T (C)** | **Reff (μm)** | **Plates (%)** | **Columns (%)** | **Flight Notes** |
|---|---|---|---|---|---|---|---|
| 2-Sep | 0.41 | 29 | -52 | > 10 | 58 | 42 | Fresh convection over SE US |
| 4-Sep | 0.37 | 29 | -51 | > 10 | 67 | 33 | Anvil cirrus over Gulf of Mexico |
| 11-Sep | 0.37 | 26 | -52 | < 10 | 46 | 54 | Fresh convection over Ozarks |
| 13-Sep | 0.45 | 37 | -71 | > 10 | 79 | 21 | Anvil cirrus over Gulf of Mexico |
| 16-Sep | 0.45 | 29 | -73 | > 10 | 76 | 24 | Tropical system over Gulf of Mexico |

a) CPI Cirrus Particle Images: 18 September 2013 15:38:59 UTC

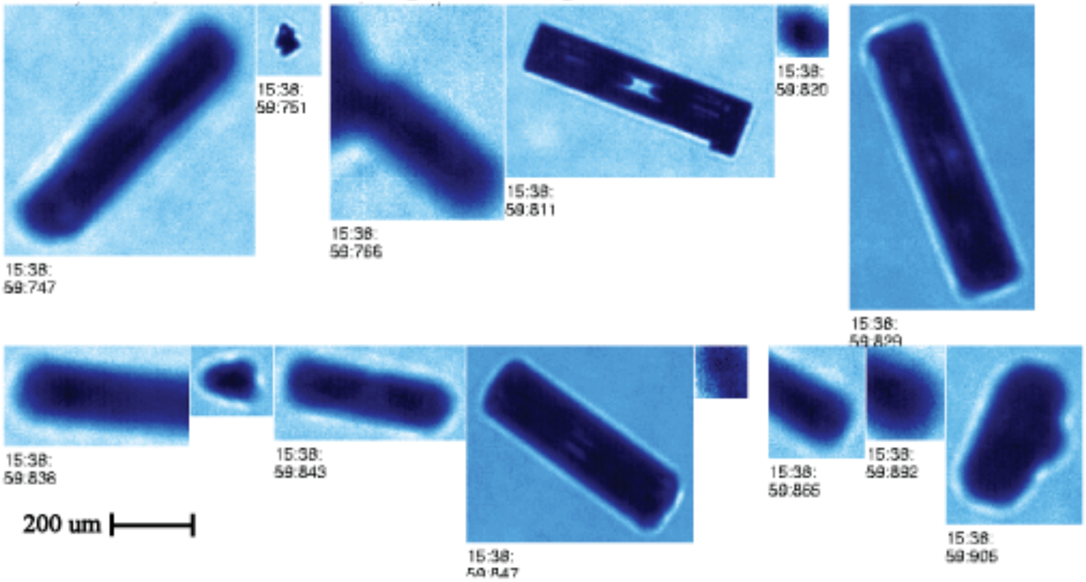

b) CPI Cirrus Particle Images: 18 September 2013 15:54:00 UTC

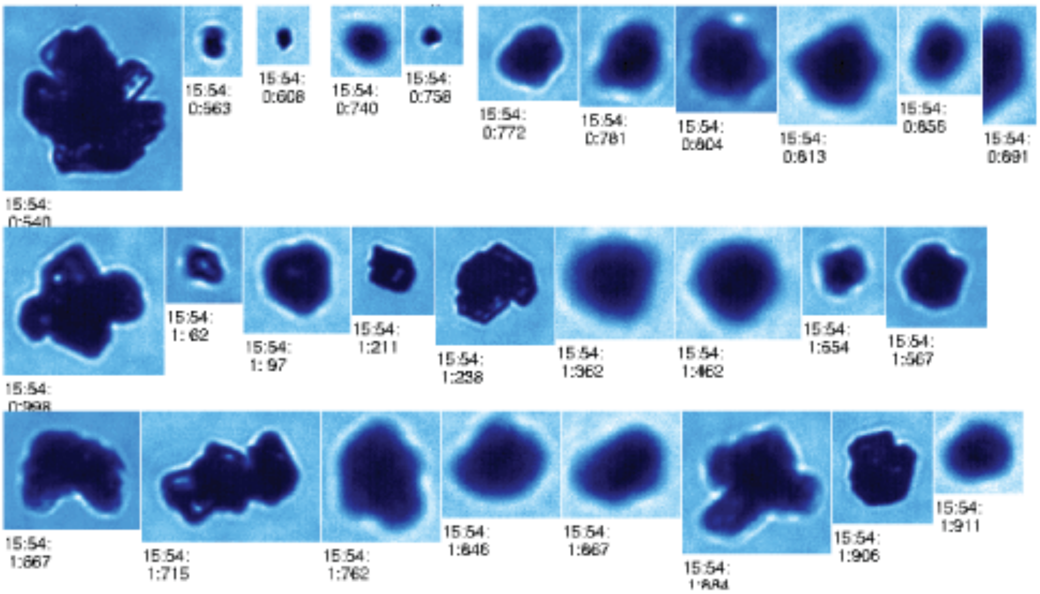

**Figure 4.6**. The CPI ice particle images for the SEAC$^4$RS flight on 18 Sept. 2013 from within a fresh anvil cirrus cloud (a) and an aged anvil cirrus clouds (b). The fresh anvil was observed around 15:38:39 UTC and the aged anvil was observed around 15:54:00 UTC.

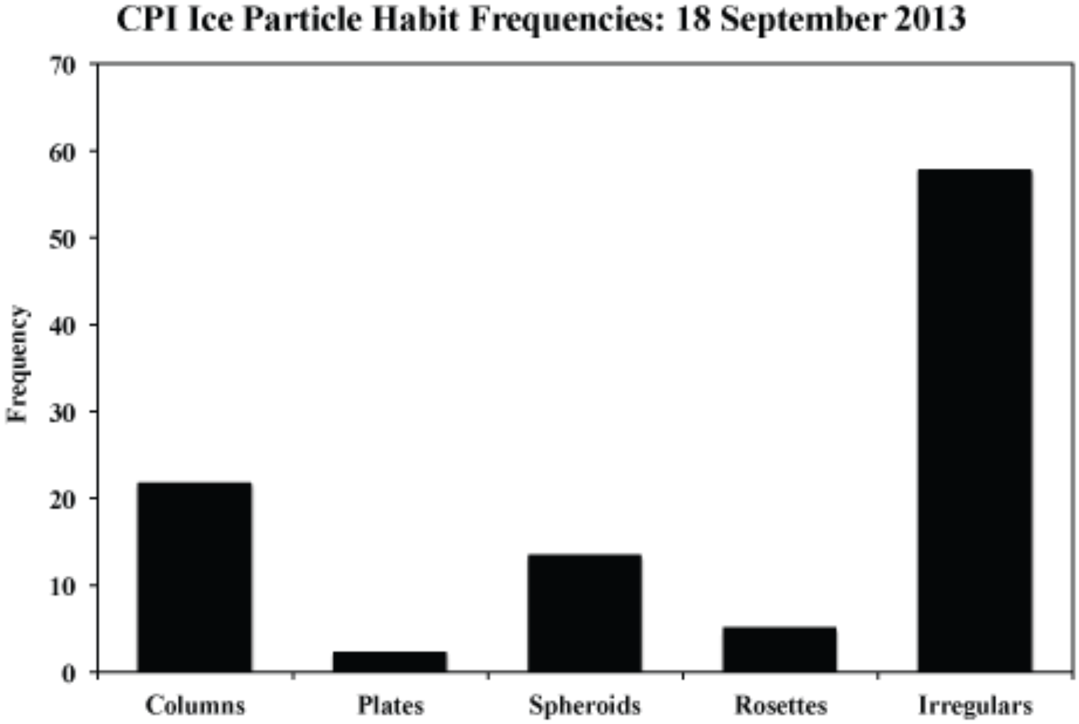

**Figure 4.7**. A histogram of ice particle habit as determined manually using CPI data for the SEAC$^4$RS flight on 18 Sept. 2013 from 14:43 to 15:54 UTC.

The cirrus properties retrieved during the Mid-Latitude cases are very different compared to the Tropical cases. The Mid-Latitude cases are characterized by:

- Lower lidar ratios (mean of 23 sr)
- Lower depolarization ratios (mean of 0.37)
- Smaller ice particle sizes
- A mix of rosette and irregular particle habits

The Tropical cases are characterized by:

- Higher lidar ratios (mean of 33 sr)
- Higher depolarization ratios (mean of 0.40)
- Larger ice particle sizes
- Ice particle shapes dominated by irregular plates

The higher depolarization ratios for the Tropical Case are not a consequence of colder cloud temperatures, as the mean cloud top temperatures is 16 C warmer than the Mid-Latitude Case, but are a consequence of the presence of large columns (Figure 4.6). Large columns were more frequently observed during the Tropical Case than the Mid-Latitude Case (Figure 4.7). Noel *et al.* (2004) showed that columns, with aspect ratios of greater than 1.0, are associated with depolarization ratios higher than 0.50. The ice concentrations, extinction and IWC, for the Tropical Case are similar to the results of Lawson *et al.* (2010) for fresh and aged anvils and higher than previous in situ measurements of mid-latitude cirrus (Lawson *et al.* 2006). Although these case studies suggest cirrus properties are related to cloud formation mechanism or geographic location, more statistics are needed to support these findings.

## 4.3 CPL Statistics of Cirrus Properties

Lidar ratio retrievals using the transmission loss technique can be unreliable for weakly scattering layers (i.e., low COD). Thus, the following requirements are enforced on all cirrus layers selected for this study to ensure robust data:

1. Only the uppermost atmospheric layer in any profile is analyzed.
2. A layer-integrated depolarization ratio of greater than 0.27 is required to ensure the uppermost layer is a cirrus cloud (Yorks *et al.* 2011a).
3. A minimum value of 0.10 COD at 532 nm is imposed to eliminate weakly scattering layers and low SNR.

Using these requirements, I examine over 150,000 observations (at the native horizontal resolution of 200 m) of transparent cirrus in this study. The mean optical depth of these transparent layers is 0.35 ± 0.24, with the majority of the layers classified as thin cirrus

(COD < 0.30). It is possible the size distributions of the ice crystals within transparent cirrus could be skewed toward smaller mean values (Vaughan *et al.* 2010). The standard deviations presented throughout this study represent both uncertainties in the CPL measurements and the natural variability of cirrus cloud properties.

The CPL data is broken up into 5 clusters for analysis that will be referenced throughout the paper as:

- **Mid-Latitude**: All cirrus layers between 35 N and 50 N regardless of season and formation mechanism.
- **Tropical**: All cirrus layers between 10 S and 25 N regardless of season or cloud top altitude.
- **Synoptic**: All cirrus layers over the mid-latitudes (35 N and 50 N) occurring between the months of September and April.
- **Convective**: All cirrus layers over the tropics (10 S and 25 N) and cases over the lower mid-latitudes (25 N to 35 N) observed in the Northern Hemisphere summer months (June to August) deemed convective in nature.
- **TTL**: All cirrus layers over the tropics (10 S and 25 N) with a COD less than 0.30 and a cloud top altitude greater than 15 km.

The number of observations for each cluster is shown in Table 4.6. A total of 62 individual Synoptic cirrus clouds were observed for over 32,000 layers (about 61 degrees of freedom). The Convective cirrus cluster has 109,000 layer observations with over 250 individual cirrus clouds sampled. Figure 4.8 shows the latitude (a) and cloud top temperature (b) frequency distributions for the Synoptic (blue), Convective (red), and TTL (black) clusters. The Synoptic cluster represents cirrus formed through synoptic-scale uplift over the mid-latitudes (30 N to 50 N). The Convective cluster represents convective anvil and turret cirrus formed over the tropics and sub-tropics (10 S to 32 N), while the TTL cluster represent the thinnest and coldest tropical cirrus within the tropopause layer, with cloud top temperatures colder than -70 C.

**Table 4.6.** Number of observations for each cirrus cluster.

| Cluster | Observations |
|---|---|
| All Data | 176,715 |
| Mid-Latitude | 49,346 |
| Tropical | 73,781 |
| Synoptic | 32,603 |
| Convective | 109,534 |
| TTL | 14,480 |

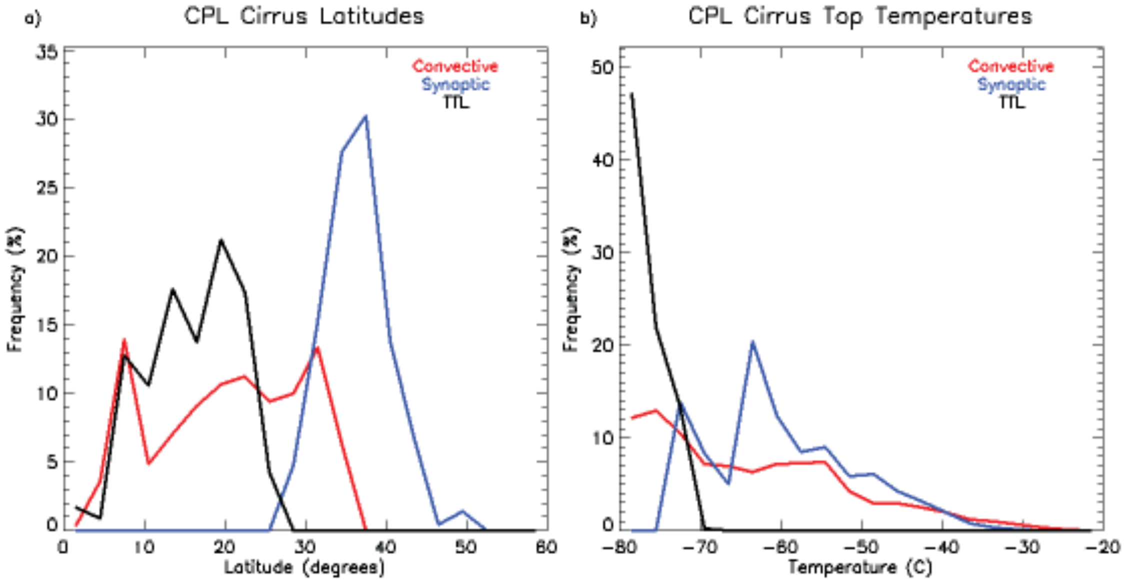

**Figure 4.8**. The CPL frequency distributions of latitude (a) and cloud top temperature (b) for the Synoptic (blue), Convective (red) and TTL (black) clusters.

Tropical cirrus formed through the rapid upward motions of convection have higher lidar ratios than synoptically-generated cirrus over mid-latitudes. The mean CPL 532 nm lidar ratio for the Convective cluster (29.47 ± 10.71 sr) is about 5 sr (~ 20 %) higher than the Synoptic cluster (24.28 ± 9.23 sr), as shown in Table 4.7. Furthermore, the lidar ratio frequency distribution for the Convective cluster (red) peaks at about 28 sr and shows a tail at higher lidar ratios, while the peak of the Synoptic cluster (blue) is 23 sr and shows lower frequencies at higher lidar ratios (Figure 4.9b). The distribution for Mid-Latitude cirrus (Figure 4.9a) is nearly identical to the Synoptic cluster, since nearly 70% of mid-latitude cirrus in this study are deemed to be solely synoptically-generated. These trends in lidar ratio are similar to those found in the Mid-Latitude and Tropical Cases and by Yorks *et al.* (2011a). The 5 sr differences in lidar ratio is statistically significant, since over 50 individual cirrus clouds are observed in both the Synoptic and Convective clusters. Currently, CALIPSO version 3 extinction retrieval algorithms for cirrus clouds too optically thick to constrain a lidar ratio assume a lidar ratio of 25 sr for all types of cirrus clouds, about 5 sr less than the value for convectively-generated cirrus clouds found in this study. An error in the assumed lidar ratio of 5 sr using the Klett/Fernald method will cause about a 20% error in the retrieval of the extinction coefficient from backscatter lidars (Young *et al.* 2013).

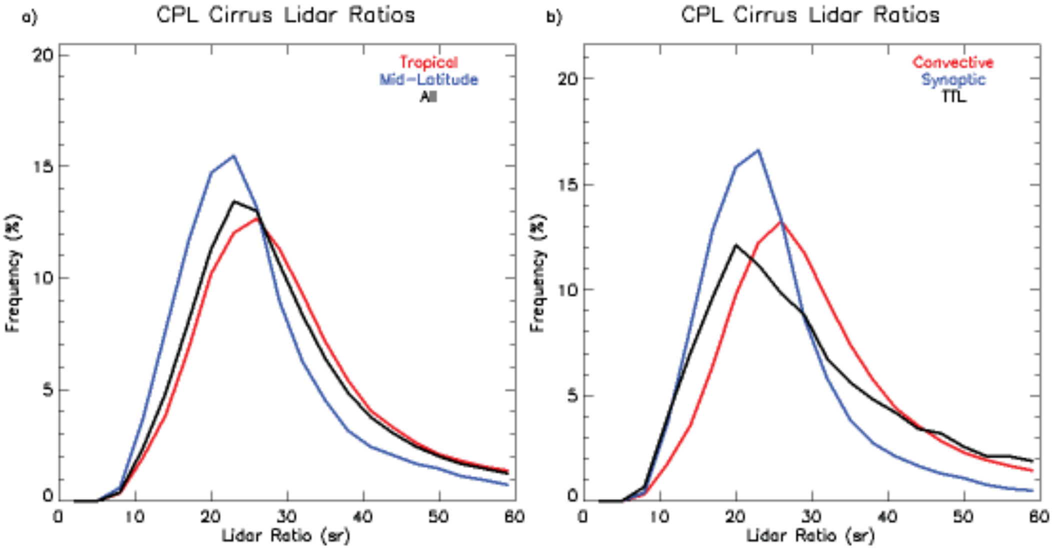

**Figure 4.9**. The CPL 532 nm lidar ratio frequency distributions for various regions (a) such as mid-latitudes (blue), tropical (red) and all data (black). Also plotted are CPL 532 nm lidar ratio frequency distributions for other clusters (b), such as Synoptic (blue), Convective (red) and TTL (black) representing various formation mechanisms.

**Table 4.7.** CPL constrained cirrus lidar ratio statistics.

| Cluster | Mean | Median | Std. Dev. |
|---|---|---|---|
| All Data | 27.82 | 25.98 | 10.98 |
| Mid-Latitude | 25.23 | 23.27 | 9.99 |
| Tropical | 28.38 | 26.99 | 11.42 |
| Synoptic | 24.28 | 22.55 | 9.23 |
| Convective | 29.47 | 27.66 | 10.71 |
| TTL | 28.12 | 25.62 | 12.08 |

Cirrus depolarization ratios appear to be more dependent on formation mechanism than geographic location. Figure 4.10a shows the CPL 1064 nm layer-integrated depolarization ratio frequency distributions for the Mid-Latitude (blue) and Tropical (red) clusters. The distributions are very similar to the distribution for all data (black) and the mean depolarization ratios (Table 4.8) for the Mid-Latitude and Tropical clusters are within 0.01 of the overall mean (0.411 ± 0.084). However, depolarization ratios are very different for Synoptic (blue), Convective (red), and TTL (black) clusters (Figure 4.10b). Synoptically-generated cirrus have a mean layer-integrated depolarization ratio of 0.38 ± 0.06 and are infrequently observed with depolarization ratios greater than 0.47. The low values of depolarization ratio are consistent with the Mid-Latitude Case and warmer cloud top temperatures (mean of -57 C). Convectively-generated cirrus have a mean layer-integrated depolarization ratio of 0.42 ± 0.07 and demonstrate a more normal distribution. These higher depolarization ratios are attributed to colder cloud top temperatures (mean of -61 C), as well as more frequent observations of columns in the tropics, as suggested by the Tropical Case and previous in situ data (Noel *et al.* 2004; Lawson *et al.* 2010). TTL cirrus have a mean layer-integrated depolarization ratio of 0.47 ± 0.05 and are infrequently observed with depolarization ratios less than 0.38. The colder temperatures (colder than -70 C) of TTL cirrus cause the high depolarization ratios observed by CPL. Figure 4.11 shows a probability density function (PDF) plot of the layer-integrated depolarization ratio versus cloud top temperature. For all CPL data, a decrease in cloud top temperature of 10 C leads to increase in depolarization ratio of 0.12. This relationship between cloud top temperature and depolarization ratio is well documented in the literature (Sassen and Benson 2001; Platt *et al.* 2002; Reichardt *et al.* 2002; Yorks *et al.* 2011a).

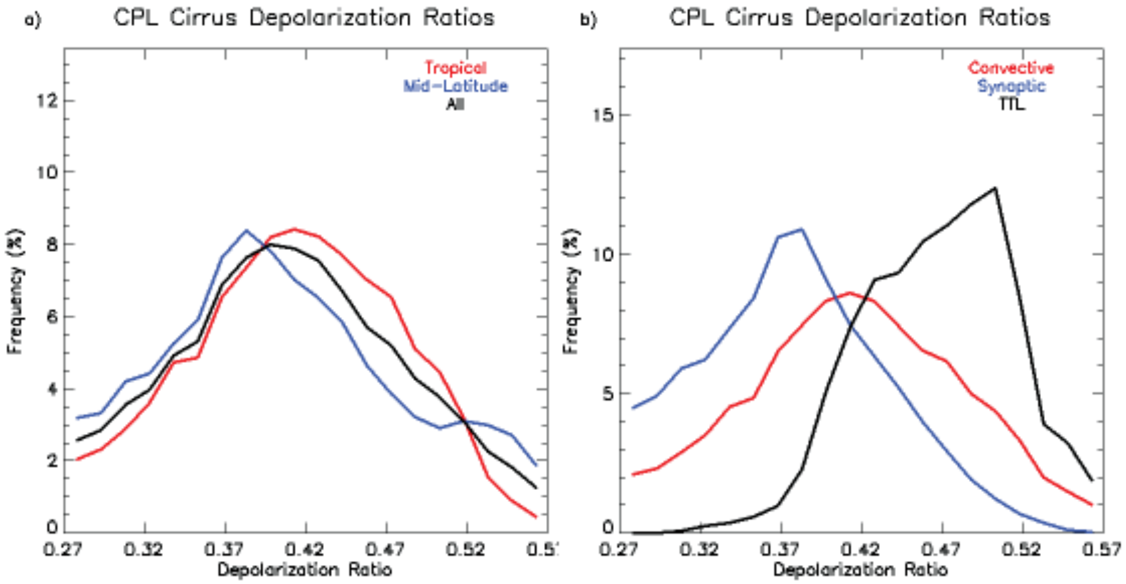

**Figure 4.10**. The CPL 1064 nm layer-integrated depolarization ratio frequency distributions for various regions (a) such as mid-latitudes (blue), tropical (red) and all data (black). The same frequency distributions are also plotted for other clusters (b), such as Synoptic (blue), Convective (red) and TTL (black) representing various formation mechanisms.

**Table 4.8.** CPL cirrus layer-integrated depolarization ratio statistics.

| **Cluster** | **Mean** | **Median** | **Std. Dev.** |
|---|---|---|---|
| All Data | 0.411 | 0.410 | 0.084 |
| Mid-Latitude | 0.413 | 0.403 | 0.080 |
| Tropical | 0.404 | 0.413 | 0.089 |
| Synoptic | 0.378 | 0.376 | 0.057 |
| Convective | 0.418 | 0.417 | 0.070 |
| TTL | 0.468 | 0.470 | 0.047 |

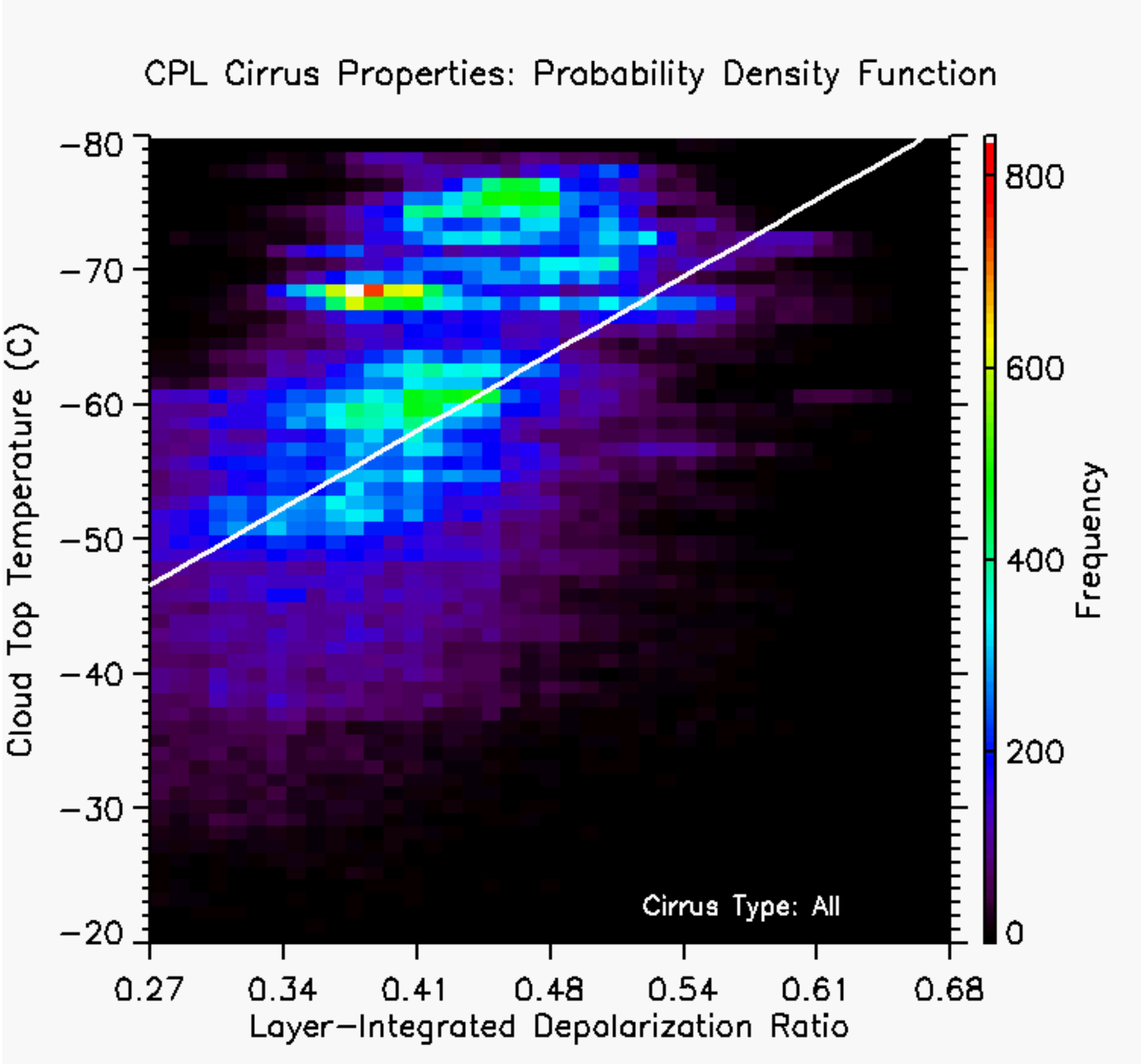

**Figure 4.11**. A probability density function (PDF) plot of the layer-integrated depolarization ratio versus cloud top temperature for all 176,000 cirrus layers observed. The white line represents a linear fit to the data.

Cirrus formed through synoptic-scale uplift have slightly higher backscatter color ratios than convectively-generated cirrus. The median CPL color ratio for the Convective cluster (0.881) is slightly lower than the Synoptic cluster (0.918), as shown in Table 4.9. Results for the Mid-Latitude and Tropical clusters are similar (within 0.03). These results yield higher color ratios than the mean color ratio of 0.83 ± 0.19 determined by Vaughan *et al.* (2010) for strongly scattering cirrus layers (mostly opaque). The transparent layers studied here have slightly higher color ratios (mean of 0.90 ± 0.35) than opaque layers for the same projects (mean of 0.87 ± 0.30). Perhaps the most interesting relationship between color ratio and generation mechanism occurs for the TTL cluster. The median CPL color ratio for the TTL cluster is 0.853 and the frequency distribution (Figure 4.12b) shows a high occurrence of color ratios less than 0.80. It has been determined using aircraft measurements and air parcel back trajectories that thin cirrus near the tropical tropopause can form in situ due to cold air in the tropopause layer (Pfister *et al.* 2001; Gettelman *et al.* 2002; Jensen *et al.* 2005). These in situ TTL cirrus can often be classified as subvisible (COD < 0.03) and tend to have a large population of small ice particles (Lawson *et al.* 2008; 2010). As particle sizes become smaller than the geometric optics regime (~1 μm), the spectral dependence of the backscatter coefficients will become more prevalent.

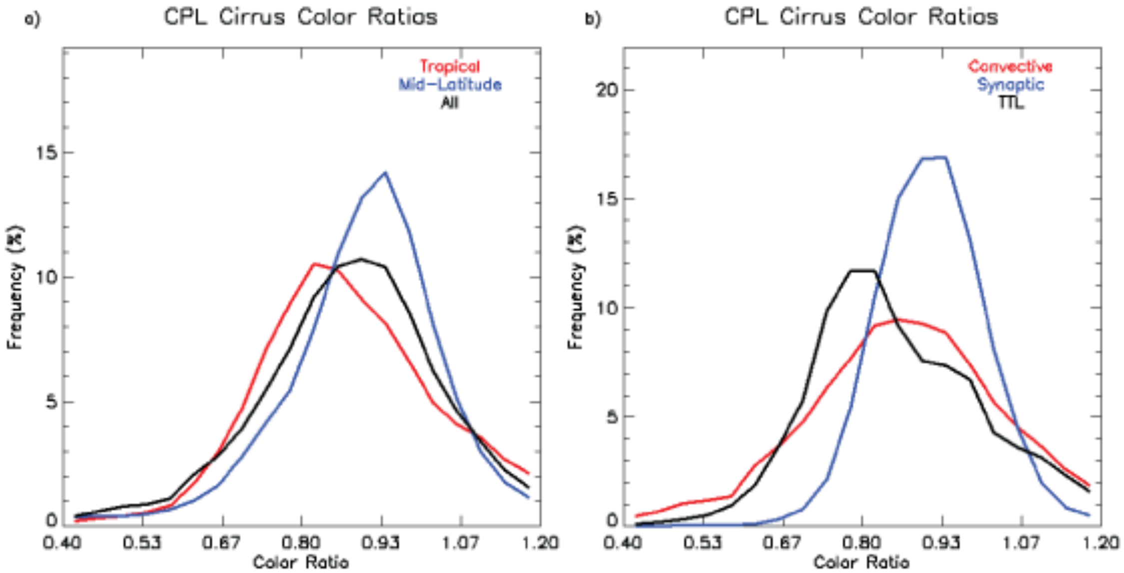

**Figure 4.12**. The CPL backscatter color ratio frequency distributions for various regions (a) such as mid-latitudes (blue), tropical (red) and all data (black). The same frequency distributions are also plotted for other clusters (b), such as Synoptic (blue), Convective (red) and TTL (black) representing various formation mechanisms.

**Table 4.9.** CPL cirrus layer-integrated color ratio statistics.

| Cluster | Mean | Median | Std. Dev. |
|---|---|---|---|
| All Data | 0.914 | 0.892 | 0.357 |
| Mid-Latitude | 0.926 | 0.919 | 0.242 |
| Tropical | 0.909 | 0.874 | 0.467 |
| Synoptic | 0.945 | 0.918 | 0.227 |
| Convective | 0.910 | 0.881 | 0.401 |
| TTL | 0.929 | 0.853 | 0.457 |

The analysis of CPL color ratio also yields an interesting relationship between color ratio and depolarization ratio for cirrus formed due to synoptic-scale uplift. Figure 4.13 shows the PDF for depolarization ratio versus color ratio for the Synoptic (a), and Convective (b) clusters. Color ratio appears to be related (directly proportional) to depolarization ratio for synoptically-generated cirrus, but not for any other type of cirrus. Since a color ratio of 1.0 represents larger particles (> 10 μm) and a color ratio of zero represents smaller particles, this suggests the depolarization ratio increases as the particle size increases. This supports the findings of Lawson *et al.* (2006) that particles in mid-latitude cirrus can be classified into crystal habit categories that are a function of particle size. They found that spheroids dominate the smallest size regimes, followed by small irregulars for slightly larger particles. The particles greater than 100 μm are composed mostly of columns and rosette shapes. Convectively-generated cirrus tend to contain more particles larger than 10 μm and plate-like aggregates, as was observed in Tropical Case. This relationship is not observed in any of the other four clusters analyzed, and is not observed in opaque synoptically-generated cirrus, the type of cloud that CALIPSO uses to calibrate the 1064 nm channel (Vaughan *et al.* 2010).

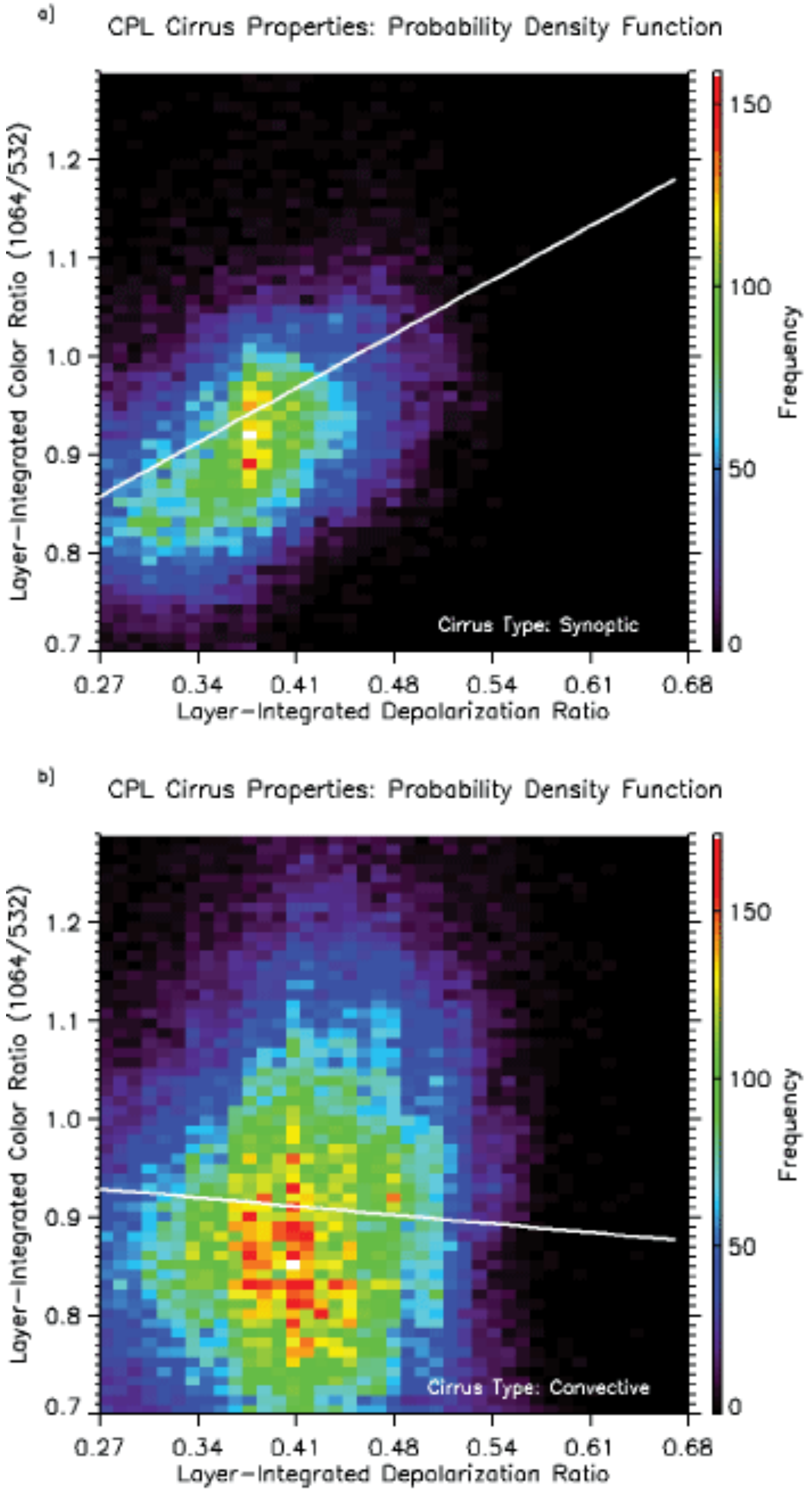

**Figure 4.13**. A probability density function (PDF) plot of the layer-integrated depolarization ratio versus layer-integrated color ratio for the Synoptic (a) and Convective (b) clusters. The white line represents a linear fit to the data.

## 4.4 CALIPSO Statistics of Cirrus Properties

Statistics of CALIOP cirrus retrievals yield similar results to the CPL resolved regional trends in cirrus lidar ratios and dynamic generation mechanisms, but on a global scale. Figure 4.14 shows the CALIOP global distribution of nighttime constrained 532 nm lidar ratio retrievals for cirrus layers with the South American Anomaly (SAA) removed during the years 2006 to 2010. The lidar ratios over ocean between the latitudes of 20 N and 20 S are typically greater than 35 sr (yellow and red colors). However, the lidar ratios over the mid-latitude continents, where synoptically-generated cirrus are typically observed, are as low as 22 sr. These results support the CPL findings that cirrus formed due to synoptic-scale uplift have lower lidar ratios than cirrus formed due to rapid motions of convection over the tropics. The CALIOP data also suggests the lidar ratio for cirrus observed over ocean is greater than cirrus observed over land. If the CPL data is subset into cases over ocean (83,834 observations) and over land (47,586 observations), the mean lidar ratio for cirrus over ocean is 29.6 ± 10.9 sr, while over land the mean lidar ratio is 26.3 ± 10.4 sr. In most cases, the cirrus observed over ocean is formed due to rapid upward motions of maritime convection and the synoptically-generated cirrus are typically observed over land in the Northern Hemisphere.

Another possible explanation for the higher lidar ratios over ocean is that cirrus in these regions are formed in more pristine conditions, with ice nuclei (IN) from mid-tropospheric aerosols (Fridlind *et al.* 2004). Cirrus observed over land in the Northern Hemisphere can be exposed to high aerosol loading from continental pollution sources. The aerosol indirect radiative effect occurs when clouds contain more numerous but smaller particles that can increase cloud albedo due to the presence of high aerosol concentrations (Twomey 1977; Albrecht 1989; Morrison and Grabowski 2011). An increase in cloud albedo decreases the lidar ratio. Direct measurements of IN in cirrus ice crystals have been few, but recently Cziczo *et al.* (2013) analyzed chemical and physical properties of cirrus cloud particles collected during four field campaigns from 2002 to 2011 over North and Central America. They found that only about 10 percent of ice particles contained evidence of sulfate or organic carbon particles. Mineral dust and metallic particles are the dominant IN in the heterogeneous freezing process, even in cirrus observed over the continental United States (Cziczo *et al.* 2013). In regions of highest dust or metallic aerosol loading, such as the Atlantic Ocean just west of the Saharan Desert, cirrus cloud lidar ratios are between 30 and 35 sr, similar to pristine areas of the Pacific Ocean (Figure 4.14). This suggests that dynamic formation mechanism, not continental aerosol loading, is the source of lower cirrus lidar ratios observed over the Northern Hemisphere continents.

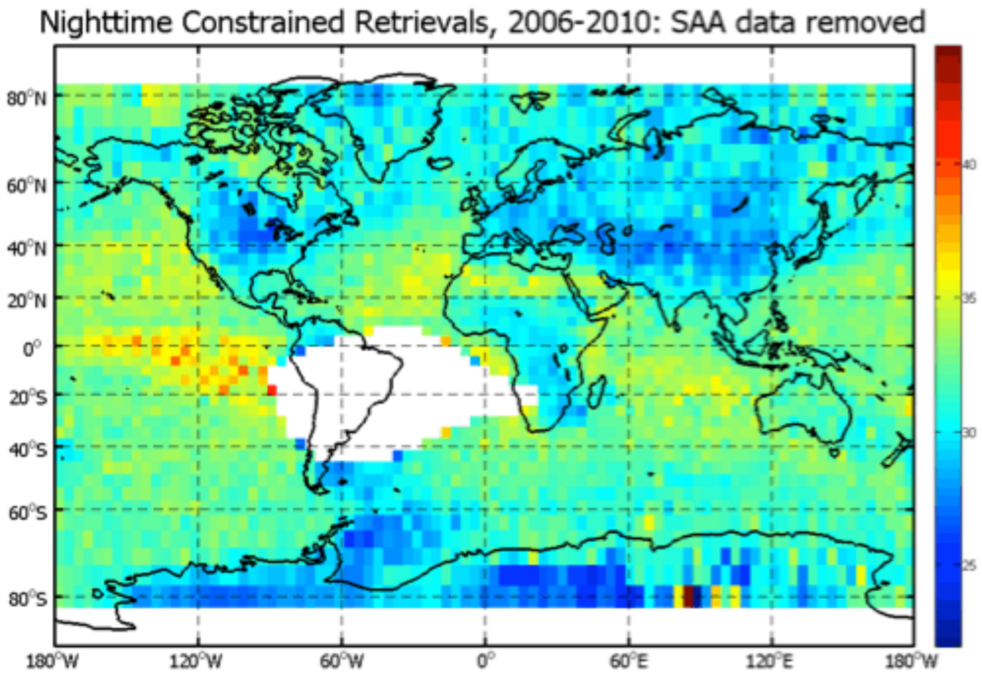

**Figure 4.14**. The CALIOP global distribution of nighttime constrained 532 nm lidar ratio retrievals for cirrus layers with the South American Anomaly (SAA) removed during the years 2006 to 2010 using the CALIOP version 3 algorithms.

The relationship between color ratio and depolarization ratio is also detected when analyzing statistics of CALIOP cirrus retrievals. Figure 4.15 shows a PDF of layer-integrated color ratio (1064/532) and layer-integrated 532 nm total depolarization ratio (particle plus molecular) from CALIOP data during December 2009 for mid-latitude cirrus (a) and tropical cirrus (b). These plots are computed using the CALIPSO version 3 algorithms and the mid-latitude cirrus are restricted to the Northern Hemisphere. The CALIOP data in Figure 4.15 is not restricted to layers in which the lidar ratio is constrained, so this data likely comprises both transparent and opaque cirrus layers. The color ratio is directly proportional to depolarization ratio for winter mid-latitude cirrus formed due to synoptic-scale uplift, similar to the results found using CPL data. No relationship between CALIOP color ratio and depolarization ratio can be discerned for tropical cirrus. More coincident in situ and lidar measurements are necessary to determine the strength of this relationship and its influence on the 1064 nm calibration technique used for space-based lidar retrievals of calibrated backscatter from instruments such as CALIOP and CATS.

In this chapter, I examine the relationship between cirrus cloud properties and dynamic formation mechanism through statistics of CPL cirrus properties from more than 100 ER-2 and Global Hawk flights. Many of these flights include coincident measurements of cirrus microphysical properties from the RSP instrument and in situ measurements available from the 2D-S and CPI probes. The lidar ratios and depolarization ratios retrieved from CPL for cirrus clouds formed by synoptic-scale uplift over land are lower than convectively-generated cirrus over tropical oceans. These higher depolarization ratios for tropical cirrus are a consequence of colder cloud temperatures and the presence of more column-shaped ice particles compared to mid-latitude cirrus. Furthermore, the CPL color ratio is directly proportional to depolarization ratio for synoptically-generated cirrus, but not for any other type of cirrus.

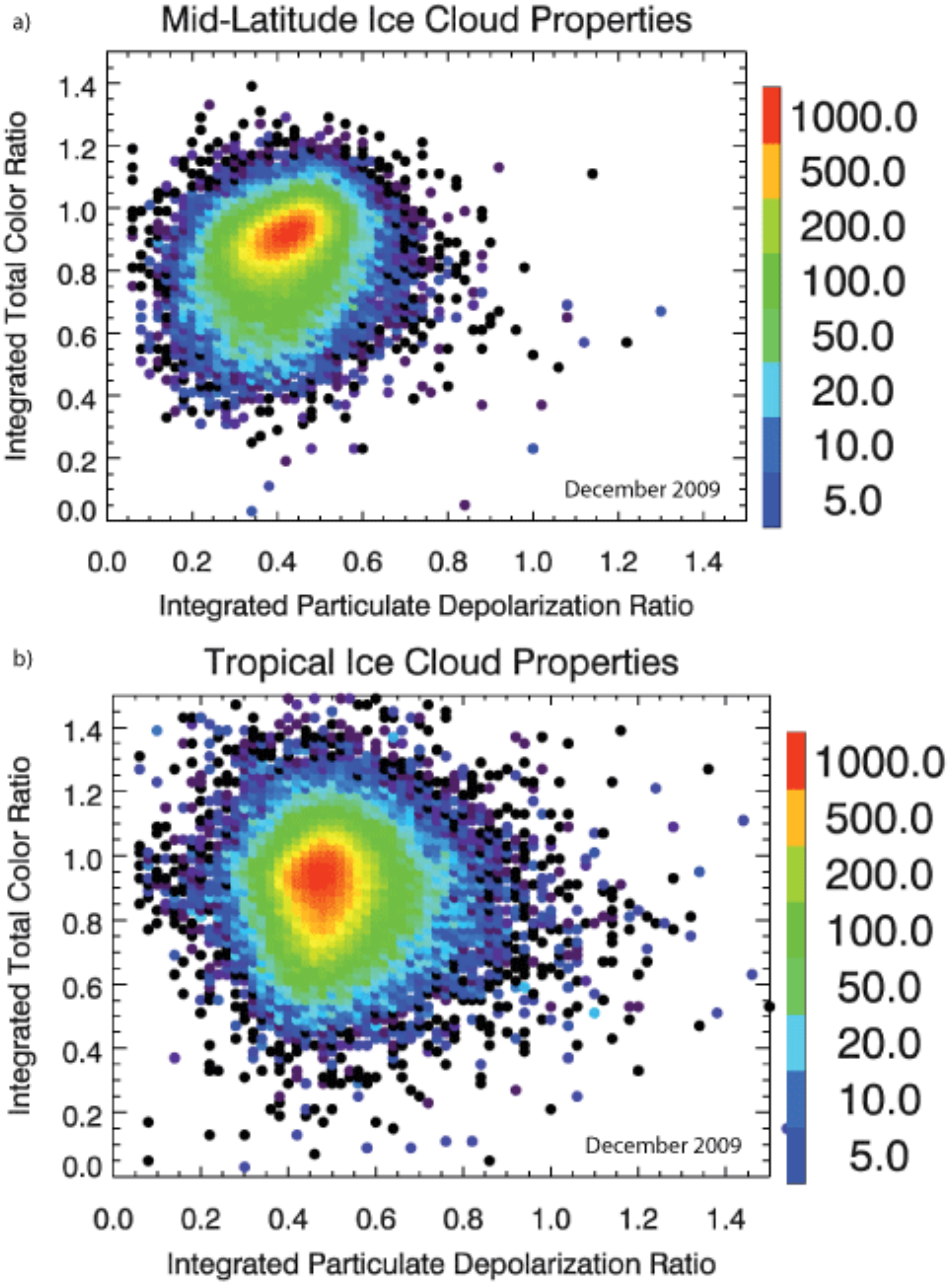

**Figure 4.15**. A probability density function (PDF) plot of the CALIOP layer-integrated 532 nm depolarization ratio versus layer-integrated color ratio for Mid-Latitude (a) and Tropical (b) cirrus clouds.

# Chapter 5: Future Work

The ACATS telescope was rotated to more than one look angle for the first time during the WAVE project. Due to an unstable telescope bearing and limited time before the project, the telescope alignment was optimized only at the 270-degree look angle. The telescope alignment for the other three look angles was performed in the field using a new and untested in-flight telescope alignment procedure. Until the telescope alignment at all four look angles could be optimized, only two look angles were used for most flights. The telescope alignment at the 0, 90, and 180 degree look angles was often acceptable but not optimal, causing lower SNR and higher uncertainty in the ACATS retrievals at these look angles. The proper telescope alignment was not achieved at all four look angles until the 26 September ferry flight back to Palmdale, CA (Figure 2.6).

In addition to the telescope alignment issues, the software to maintain the etalon stability during flight was not optimized, causing the peak in the measured aerosol spectrum to drift across detector channels more than anticipated. Although this etalon instability introduces little uncertainty in the cloud and aerosol retrievals, LOS wind retrievals are unreliable because the peak has drifted away from the location of the outgoing laser spectrum. Cloud and aerosol particles have a very narrow velocity distribution relative to the frequency of laser transmitters, and are shifted by the same spectral width. A particle velocity of 425 $ms^{-1}$ results in a Doppler shift of 1 picometer or 2.4 GHz. Thus, Doppler lidar transmitters and receivers must be controlled to sub-picometer accuracy. The ACATS detector has a spectral width of about 1.5 picometers, with each channel spanning 0.060 picometers. A shift in the peak transmission by 2 channels can introduce an error of greater than 30 $ms^{-1}$ to the LOS wind retrieval. Due to these limitations, this study focuses on ACATS retrievals cloud and aerosol properties from the WAVE project, particularly those at the 270-degree look angle and high quality data from the other look angles. The statistics from the WAVE project, especially from the 26 Sept. 2012 flight, provide the optimal telescope alignment for future flights. The software to maintain the etalon stability will be improved and a new telescope bearing will be installed before future ACATS flights, providing an opportunity to examine the wind retrieval algorithms developed for the ACATS system.

To determine the horizontal wind velocity, the ACATS points 45 degrees off-nadir and measures the LOS component of the return signal. The horizontal wind velocity vector is computed using an appropriate scanning scheme, assuming that the wind field over the sensed volume is horizontally homogeneous (Schwiesow *et al.* 1985). If a conical scan is performed with the apex of the cone at the system telescope, the LOS velocity is a function of azimuth angle for a given range. The equations for computing the horizontal wind velocity using two orthogonal LOS measurements are given in Schwiesow *et al.* (1985), McGill *et al.* (1997b) and Werner (2005) for ground-based systems. These equations are further complicated for airborne systems, which must be corrected for aircraft motion (Lee *et al.* 1994; Leon and Vali 1998).

The method for computing the horizontal wind velocity and correcting the LOS wind measurement for aircraft motion is adapted from Lee *et al.* (1994) and Leon and Vali (1998). The equation for the LOS Doppler velocity measured from the aircraft is:

$$U_{LOS} = b \bullet V - b \bullet (V_{ac} + V_a) \qquad \text{Eq. 5.1}$$

where V is the three-dimensional velocity of the scatterers relative to the platform (i.e. horizontal wind velocity vector) and is defined as:

$$V = ui + vj + wk \qquad \text{Eq. 5.2}$$

The aircraft velocity ($V_{ac}$) is measured from the ACATS GPS/IMU and is defined as:

$$V_{ac} = VG_{ac} \sin Ti + VG_{ac} \cos Tj + WG_{ac} k \qquad \text{Eq. 5.3}$$

where T is the track azimuth angle, equal to the sum of the drift (D) and heading (H). This can also be estimated by computing the horizontal wind at the surface of the earth. Assuming the surface is stationary, there should be no contribution from particles (V=0). Thus the LOS velocity is equal to the aircraft velocity. The apparent antenna motion ($V_a$) can contribute to the LOS velocity if the GPS antenna is located far from the IMU and the pitch and heading change significantly with time. $V_a$ is defined as:

$$V_a = -\Omega_{ac} \times L_{GPS} = -L_{GPS}\left(\frac{dH}{dt} + \frac{dP}{dt}\right) \qquad \text{Eq. 5.4}$$

where $L_{GPS}$ is the distance between the antenna and GPS, H is the aircraft heading and P is the aircraft pitch. The beam vector (b) is the unit vector pointing along the lidar beam in earth-relative coordinates. To compute b in earth-relative coordinates, we must first convert from aircraft-relative coordinates and track-relative coordinates.

We start by considering the laser pointing angles of the ACATS instrument relative to the aircraft using the aircraft-relative coordinate system. In this coordinate system, Z is the vertical coordinate with +Z pointing up. Positive Y points towards the nose of the aircraft, while +X points toward the right wing. In this coordinate system, we define the following angles:

1) tilt angle ($\tau_{ac}$): the off-nadir angle of the laser beam
    a. for ACATS $\tau_{ac} = 45$
2) rotation angle ($\theta_{ac}$): the “look angle of the telescope, $0 < \theta_{ac} < 360$

a. for ACATS $\theta_{ac}$ = 0, 90, 180, 270

3) azimuth angle ($\alpha_{ac}$): equal to the rotation angle ($\alpha_{ac} = \theta_{ac}$)

4) elevation angle ($\phi_{ac}$): following the system Lee *et al.* (1994) created, it is defined:

$$\phi_{ac} = -(90^o - \tau_{ac}) \qquad \text{Eq. 5.5}$$

Using these angles, we define the ACATS beam vector in aircraft-relative coordinates ($b^{ac}$) as:

$$b^{ac} = \begin{pmatrix} b_x^{ac} \\ b_y^{ac} \\ b_z^{ac} \end{pmatrix} = \begin{pmatrix} \cos\phi_{ac}\sin\alpha_{ac} \\ \cos\phi_{ac}\cos\alpha_{ac} \\ \sin\phi_{ac} \end{pmatrix} \qquad \text{Eq. 5.6}$$

Note that these components are different from those defined in Lee *et al.* (1994) because the pointing geometry of the Doppler radar EDORA and ACATS are different. This vector can then be used with the matrices for heading ($M_H$), pitch ($M_P$), and roll ($M_R$) defined in Lee *et al.* (1994) to compute the earth-relative beam vector:

$$b = M_H M_P M_R b^{ac} \qquad \text{Eq. 5.7}$$

This yields the following components of the beam vector:

$$b_x = r\begin{bmatrix} \cos H(\cos R\cos\phi_{ac}\sin\alpha_{ac} + \sin R\sin\phi_{ac}) \\ +\sin H\cos P\cos\phi_{ac}\cos\alpha_{ac} \\ +\sin H\sin P(\sin R\cos\phi_{ac}\sin\alpha_{ac} - \cos R\sin\phi_{ac}) \end{bmatrix} \qquad \text{Eq. 5.8}$$

$$b_y = r\begin{bmatrix} -\sin H(\cos R\cos\phi_{ac}\sin\alpha_{ac} + \sin R\sin\phi_{ac}) \\ +\cos H\cos P\cos\phi_{ac}\cos\alpha_{ac} \\ +\cos H\sin P(\sin R\cos\phi_{ac}\sin\alpha_{ac} - \cos R\sin\phi_{ac}) \end{bmatrix} \qquad \text{Eq. 5.9}$$

$$b_z = r\begin{bmatrix}\sin P\cos\phi_{ac}\cos\alpha_{ac} \\ -\cos P(\sin R\cos\phi_{ac}\sin\alpha_{ac} - \cos R\sin\phi_{ac})\end{bmatrix} \qquad \text{Eq. 5.10}$$

Only profiles with minimal aircraft motion are used for ACATS wind retrievals, which include aircraft pitch and roll angles less than 3 degrees. For the along-track look angles, the small angles of P and R reduce $b_x$ and $b_y$ to:

$$b_x = r\left[\sin H\cos\phi_{ac}\right] \qquad \text{Eq. 5.11}$$

$$b_y = r\left[\cos H\cos\phi_{ac}\right] \qquad \text{Eq. 5.12}$$

For the cross-track look angles, $b_x$ and $b_y$ reduce to:

$$b_x = r\left[\cos H\cos\phi_{ac}\right] \qquad \text{Eq. 5.13}$$

$$b_y = r\left[-\sin H\cos\phi_{ac}\right] \qquad \text{Eq. 5.14}$$

To compute the aircraft velocity, earth-relative angles are needed. These angles are computed using a track-relative beam vector ($b^t$). This beam vector is computed similar to the aircraft-relative beam vector, but using the matrix for the aircraft drift ($M_D$) instead of the aircraft heading. This yields the following components of the beam vector:

$$b_x^t = r\begin{bmatrix}\cos D(\cos R\cos\phi_{ac}\sin\alpha_{ac} - \sin R\sin\phi_{ac}) \\ -\sin D\cos P\cos\phi_{ac}\cos\alpha_{ac} \\ +\sin D\sin P(-\sin R\cos\phi_{ac}\sin\alpha_{ac} + \cos R\sin\phi_{ac})\end{bmatrix} \qquad \text{Eq. 5.15}$$

$$b_y^t = r\begin{bmatrix}\sin D(\cos R\cos\phi_{ac}\sin\alpha_{ac} + \sin R\sin\phi_{ac}) \\ +\cos D\cos P\cos\phi_{ac}\cos\alpha_{ac} \\ +\cos D\sin P(\sin R\cos\phi_{ac}\sin\alpha_{ac} - \cos R\sin\phi_{ac})\end{bmatrix} \qquad \text{Eq. 5.16}$$

$$b_z^t = r\begin{bmatrix} \sin P\cos\phi_{ac}\cos\alpha_{ac} \\ -\cos P(\sin R\cos\phi_{ac}\sin\alpha_{ac} + \cos R\sin\phi_{ac}) \end{bmatrix} \qquad \text{Eq. 5.17}$$

Using these beam vector components, we can compute the earth-relative elevation angle as:

$$\phi = \sin^{-1}\frac{b_z}{r} \qquad \text{Eq. 5.18}$$

The apparent antenna motion term ($V_a$) is shown in Equation 5.19 and is assumed negligible for ACATS. The ACATS GPS and ER-2 aircraft navigation data yield small values of dH/dt and dP/dt over the 25-second average $U_{LOS}$ retrieval for WAVE data.

$$V_a = \frac{L_{GPS}}{r}\begin{bmatrix} (1+\cos P)(b_x\cos H - b_y\sin H)\dfrac{dH}{dt} \\ -\left[\sin P(b_x\sin H - b_y\cos H) - b_z\cos P\right]\dfrac{dP}{dt} \end{bmatrix} \qquad \text{Eq. 5.19}$$

The mean change in pitch over 25 seconds is 0.020 degrees, with a maximum change of 0.413 degrees. The mean change in heading over 25 seconds is 0.1586 degrees, with a maximum change of 8.51 degrees. Although the change in heading can be large, this typically occurs during a turn when the roll and pitch angles are greater than 3 degrees and ACATS wind retrievals are not derived. Additionally, $L_{GPS}$ (about 7 meters) is smaller than the range to the highest cirrus clouds measured (~4000 m). Thus the equation for the Doppler velocity for each look angle can be reduced to:

$$\begin{aligned} U_{LOS} &= \frac{1}{r}\left(ub_x + vb_y\right) + \left(w - v_t - WG_{ac}\right)\sin\phi \\ &- \frac{VG_{ac}}{r}\left(b_x\sin T + b_y\cos T\right) \end{aligned} \qquad \text{Eq. 5.20}$$

If we combine the aircraft velocity terms back into one term and assume the vertical velocity (w) and terminal fall speed ($\nu_t$) of the scatterers is negligible, the above equation can be reduced to:

$$U_{LOS} = \frac{1}{r}\left(ub_x + vb_y\right) - V_{ac} \qquad \text{Eq. 5.21}$$

where:

$$V_{ac} = \frac{VG_{ac}}{r}\left(b_x \sin T + b_y \cos T\right) + WG_{ac} \sin\phi \qquad \text{Eq. 5.22}$$

Since Equation 5.21 has two unknowns (u and v), at least two look angles are necessary to compute the u and v components of the atmospheric wind from ACATS profiles. Thus, the ACATS telescope rotates 90 degrees to accommodate these measurement needs. The telescope points fore and aft (positive and negative $y_{ac}$) which will be referred to as parallel (or along-track), and toward the right and left (positive and negative $x_{ac}$) which will be referred to as perpendicular (or cross-track). The aircraft velocity term is zero for the cross-track look angles, since there is no component to the aircraft velocity in these directions. However, the aircraft velocity term has a magnitude of about 150 ms$^{-1}$ in the along-track look angles, a function of the nearly 200 ms$^{-1}$ ground speed of the ER-2 aircraft. Two separate equations for the LOS Doppler velocity at two orthogonal look angles are rewritten for the u and v components of the particle wind for the earth-relative coordinate system as:

$$v = \frac{r^{ll}\left(U_{LOS}^{ll} + V_{ac}^{ll}\right)}{\cos H \cos\phi_{ac}} \qquad \text{Eq. 5.23}$$

$$u = \frac{r^{\perp}\left(U_{LOS}^{\perp}\right)}{\cos H \cos \phi_{ac}}$$ Eq. 5.24

The horizontal vector wind velocity (V) of the particles is estimated using the equation:

$$V = \sqrt{u^2 + v^2}$$ Eq. 5.28

The horizontal wind direction ($D_{MET}$) in meteorological coordinates is a set of three equations, shown below:

For v > 0: $$D_{MET} = \frac{180}{\pi}\tan^{-1}(\frac{u}{v}) + 180$$ Eq. 5.29

For v < 0 and u < 0: $$D_{MET} = \frac{180}{\pi}\tan^{-1}(\frac{u}{v})$$ Eq. 5.30

For v < 0 and u > 0: $$D_{MET} = \frac{180}{\pi}\tan^{-1}(\frac{u}{v}) + 360$$ Eq. 5.31

The vector horizontal wind velocity and direction within a cirrus or aerosol layer are provided at a vertical resolution of 450 m and horizontal area of 25 km$^2$. Once more accurate measurements of LOS wind velocity are collected in future ACATS flights, the ACATS wind products will be evaluated.  The u and v components of the velocity, horizontal wind velocity and horizontal wind direction will be compared to nearby radiosonde wind profiles and radar-based wind profiler data. This data will also provide the opportunity to demonstrate the aerosol transport and convective anvil outflow capabilities of the ACATS instrument.

# Chapter 6: Summary and Conclusions

I helped develop a new multi-channel direct-detection Doppler wind lidar at NASA GSFC for use on the NASA ER-2 called the Airborne Cloud-Aerosol Transport System (ACATS). ACATS employs a Fabry-Perot interferometer to provide the spectral resolution needed to retrieve the Doppler shift, similar to the ground-based University of Michigan MC direct-detection Doppler wind lidar (McGill *et al*. 1997a). The ACATS instrument design includes a seeded laser and circle-to-point converter, as well as a heating/cooling loop for stable laser performance during airborne operation. The ACATS telescope rotates to four look angles to permit the retrieval of the horizontal wind velocity within atmospheric layers. An etalon calibration procedure was created to determine the instrument defect parameter and HOE normalization values. In this dissertation, I demonstrate the utility of ACATS for HSRL retrievals of cloud and aerosol properties, advancing the technology of MC direct-detection Doppler wind lidars and HSRLs.

The nature of a MC direct-detection Doppler wind lidar such as ACATS permits three types of cloud and aerosol lidar retrievals:

- Standard backscatter lidar products such as ATB and layer boundaries
- Directly retrieved cloud and aerosol optical properties such as extinction and lidar ratio using the HSRL technique
- Horizontal wind velocity of the cloud or aerosol particles within an atmospheric layer

In this dissertation, I outline the retrieval algorithms for all three of these types of ACATS data products, focusing on the development of the HSRL derived cloud and aerosol properties. The first ACATS science flights were conducted during the WAVE project in September 2012. Initial results demonstrate the effectiveness of ACATS as an airborne HSRL system. The HSRL ATB retrieval for cirrus observed during the 14 September flight at the 270-degree look angle agreed with the ATB derived using the standard backscatter method to within 10 percent, well within the combined uncertainty of the two retrieval techniques. Since the ISS CATS HSRL receiver is designed similar to ACATS, the algorithms and data products I developed for ACATS have direct application to this future spaceborne mission. Furthermore, the ACATS HSRL and wind products can be used for science applications such as aerosol transport, smoke plume properties and convective outflow in tropical storms.

The ACATS and CPL instruments both flew as payloads on the NASA ER-2 during the WAVE campaign. Although ACATS points off-nadir at 45 degrees and rotates, the ACATS fore and aft look angles observe nearly the same atmospheric scenes as CPL with a range dependent time-offset. I assess the performance of the ACATS standard backscatter and HSRL retrievals using the coincident CPL cloud and aerosol measurements from the WAVE flights, which include observations of thin cirrus clouds and smoke layers. Three 25-45 minute case study segments were identified with thin cirrus layers, aerosol layers, and complex atmospheric scenes. Attenuated total backscatter derived using the ACATS standard backscatter technique show similar structure compared to the coincident CPL images for all cases. The layer boundaries are in excellent agreement for cirrus cloud base and more optically thick parts of cirrus clouds.

I also compare the ACATS HSRL-derived extinction and lidar ratio at 532 nm to coincident CPL retrievals. For a homogeneous thin cirrus layer, the ACATS and CPL extinction profiles agreed to within 22 percent and the mean cloud optical depth agreed to within 3 percent, well within the combined uncertainty for both instruments. The ACATS and CPL mean column optical depth agree to within 17 percent for the more complex scenes including aerosol layers, cirrus, and water clouds. Some disagreement can be attributed to the instruments viewing slightly different scenes due to the differences in viewing geometries. The ACATS HSRL-derived extinction uncertainties due to detector noise and calibration errors are 15 to 20 percent; significantly lower than the extinction uncertainties derived by CPL (greater than 50 percent), demonstrating the advantage of the HSRL technique and the need for more HSRL measurements of cirrus properties. The mean ACATS HSRL-derived lidar ratio at 532 nm for the entire WAVE campaign was about 26 sr, just 2 sr higher than the lidar ratio estimated for thin cirrus layers using CPL data. Both the ACATS and CPL frequency distributions of 532 nm lidar ratio have a peak around 18 sr, lower than those previously measured but are similar to those observed during the THORPEX-Atlantic campaign (Yorks *et al.* 2011a). Since the WAVE flights were over the mid-latitudes and conducted during September, these lower lidar ratios suggest a possible relationship between cirrus properties and dynamic formation mechanism.

The relationship between cirrus cloud properties and dynamic formation mechanism is examined through statistics of CPL cirrus observations from more than 100 ER-2 and Global Hawk flights. Many of these flights include coincident measurements of cirrus microphysical properties from the RSP instrument and in situ measurements available from the 2D-S and CPI probes during the SEAC$^4$RS project. The CPL retrieved cirrus properties for transparent cirrus layers in which the lidar ratio is estimated using the transmission loss method (Yorks *et al.* 2011a) are separated into five cirrus-type clusters that include mid-latitude, tropical, synoptically-generated cirrus, convectively-generated cirrus and TTL cirrus. CALIPSO data are used to determine if the relationships between cirrus optical properties and dynamic generation mechanisms determined using CPL are observed on a global scale. I have concluded there are three important relationships between cirrus properties and dynamic formation mechanisms determined from this dissertation.

1) The CPL and CALIOP lidar ratios for cirrus clouds formed by synoptic-scale uplift over land (24 sr) are *lower* than convectively-generated cirrus over tropical oceans (29 sr). Heymsfield *et al.* (2002) and Lawson *et al.* (2006) found a high concentration of ice crystals less than 100 μm in diameter for mid-latitude cirrus, similar to the Mid-Latitude cases presented here. Furthermore, these clouds typically have low IWC (Lawson *et al.* 2006). Clouds with a higher concentration of small particles have been shown to increase cloud albedo (Morrison and Grabowski 2011), which would decrease the lidar ratio. Since sulfate and black carbon aerosols are not frequently observed as IN (Cziczo *et al.* 2013), I put forward the hypothesis that the difference in lidar ratios for these two types of cirrus clouds are not likely a consequence of aerosol loading but of formation dynamics. The difference in CPL 532 nm lidar ratio for synoptically-generated and convectively-generated cirrus clouds can be as high as 10 sr, which can lead to error in the extinction retrieval from space-based lidar systems of 40 percent.

2) The CPL 1064 nm layer-integrated depolarization ratios for synoptically-generated cirrus over land are lower than cirrus formed due to rapid upward motions of tropical convection. These higher depolarization ratios for tropical cirrus are a

consequence of colder cloud temperatures and the presence of more column-shaped ice particles compared to mid-latitude cirrus. Depolarization ratio increases as cloud top temperature decreases, since they are both related to ice crystal shape (Sassen and Benson 2001; Platt *et al.* 2002; Reichardt *et al.* 2002; Yorks *et al.* 2011a). Ice crystals with aspect ratios of greater than 1.0 (i.e., columns) are associated with depolarization ratios higher than 0.50 (Noel *et al.* 2004).

3) The backscatter color ratio is directly proportional to depolarization ratio for synoptically-generated cirrus, but not for any other type of cirrus. A similar relationship is demonstrated with CALIOP data. Particles in mid-latitude cirrus formed through synoptic-scale uplift are frequently less than 100 μm and can be classified into crystal habit categories that are a function of particle size, as observed in the Mid-Latitude Case and by Lawson *et al.* (2006). This relationship between cirrus color ratio and depolarization ratio is likely attributed to the relationship between ice particle size and shape. In situ instruments can provide critical measurements of cirrus microphysical properties, but they do not provide vertical profiles of these measurements. Given that uncertainties in particle shape parameterizations can produce errors in the cirrus bidirectional reflectance and optical depth estimates greater than 30 percent, more coincident in situ and lidar measurements are necessary to better characterize the relationship between lidar retrievals of depolarization ratio and backscatter color ratio with microphysical properties such as ice particle shape and size. This will ultimately lead to more accurate space-based lidar retrievals, as well as the ability to use space-based lidar data as a proxy for ice particle habit.

The impact of cirrus clouds on the Earth's radiative balance depends on the microphysical properties of the ice crystals, and these in turn depend on the dynamics of formation. The relationship between cirrus properties and dynamic formation mechanism needs to be considered when studying the impact of cirrus on the Earth's climate system. The difference in lidar ratios for synoptically-generated and convectively-generated cirrus presented in this dissertation suggest multiple values should be used to parameterize the lidar ratio in the retrieval algorithms of standard backscatter lidars and improve the accuracy of extinction retrievals. Additionally, ice particle shape and size parameterizations used in cloud models and passive remote sensing retrievals (radiometers and polarimeters) should account for differences in cirrus dynamic formation mechanism. Studies that assess the influence of aerosol loading on cloud properties should also consider cirrus formation mechanism to properly diagnose the cause of changes in cloud microphysical properties. Finally, collecting coincident in situ and lidar data of cirrus properties should be a priority for future field campaigns to decrease uncertainties in relating lidar parameters such as depolarization ratio and backscatter ratio to ice particle shape and size. Decreasing the uncertainty in retrievals of cirrus extinction, perhaps the most important parameter in estimating cirrus shortwave radiative forcing, will improve our understanding of cirrus radiative impacts.

# APPENDIX A:  ACATS HSRL Retrieval Errors

The error associated with each ACATS parameter retrieved using the HSRL technique, as outlined in Section 2.3.2, is determined using propagation of errors and reported in the ACATS data files. Propagation of errors states that the error associated with a variable x, where x = f (y,z) can be written as:

$$\delta_x = \sqrt{\delta_y^2 \left( \frac{\partial f}{\partial y} \right)^2 + \delta_z^2 \left( \frac{\partial f}{\partial z} \right)^2} \qquad \text{Eq. A.1}$$

The error in the attenuated particulate backscatter ($\delta\alpha$) and attenuated molecular backscatter ($\delta\omega$) are determined from the least-square fitting technique and shown in Eq. 2.8 as $\alpha_0$ and $\omega_0$, respectively. The error in the molecular backscatter ($\delta_{\beta m}$) is a consequence of the error in the temperature and pressure profiles determined from the radiosonde instruments, and is assumed to be 5% (Luers and Eskridge 1998). The equation for the molecular optical depth error is then:

$$\delta_{\tau_m} = \sqrt{\delta_{\tau_m}^2 + \delta_{\beta_m}^2 \left( \frac{8}{3} \pi \Delta r \right)^2 + \delta_{\Delta r}^2 \left( \frac{8}{3} \pi \beta_m \right)^2} \qquad \text{Eq. A.2}$$

where the error in $\Delta r$ is assumed to be negligible. The error in the two-way molecular transmission ($\delta_{T_m}$) is:

$$\delta_{T_m^2} = \sqrt{\delta_{\tau_m}^2 \left( -2\exp(-2\tau_m) \right)^2} \qquad \text{Eq. A.3}$$

The equations for the error in the total two-way transmission (A.4), particulate backscatter (A.5), particle two-way transmission (A.6), particle optical depth (A.7), particle extinction (A.8), and particle lidar ratio (A.9) are shown below:

$$\delta_{T_{tot}^2} = \sqrt{\delta_\omega^2\left(\frac{1}{\beta_m}\right)^2 + \delta_{\beta_m}^2\left(-\frac{\omega}{\beta_m^2}\right)^2} \qquad \text{Eq. A.4}$$

$$\delta_{\beta_p} = \sqrt{\delta_\alpha^2\left(\frac{1}{T_{tot}^2}\right)^2 + \delta_{T_{tot}^2}^2\left(-\frac{\alpha}{\left(T_{tot}^2\right)^2}\right)^2} \qquad \text{Eq. A.5}$$

$$\delta_{T_p^2} = \sqrt{\delta_{T_{tot}^2}^2\left(\frac{1}{T_m^2}\right)^2 + \delta_{T_m^2}^2\left(-\frac{T_{tot}^2}{\left(T_m^2\right)^2}\right)^2} \qquad \text{Eq. A.6}$$

$$\delta_{\tau_p} = \sqrt{\delta_{T_p^2}^2\left(-\frac{1}{2T_p^2}\right)^2} \qquad \text{Eq. A.7}$$

$$\delta_{\sigma_p} = \sqrt{\delta^2_{\tau_{p(r)}} - \delta^2_{\tau_{p(r0)}}\left(\frac{1}{\Delta r}\right)^2} \qquad \text{Eq. A.8}$$

$$\delta_{S_p} = \sqrt{\delta_{\sigma_p}^2\left(\frac{1}{\beta_p}\right)^2 + \delta_{\beta_p}^2\left(-\frac{\sigma_p}{\beta_p^2}\right)^2} \qquad \text{Eq. A.9}$$

The errors in the determination of each of these variables are computed at each 450 m range bin and 400 m profile.

# References

Abreu, V. J., J. E. Barnes, and P. B. Hays, 1992: Observations of winds with an incoherent lidar detector, *Appl. Opt*., **31**, 4509–4514.

Ackerman, T. P., K. N. Liou, P. J. Valero, and L. Pfister, 1988: Heating rates in tropical anvils. *J. Atmos. Sci*., **45**, 1940–1948.

Alvarez II, R. J., L. M. Caldwell, Y. H. Li, D. A. Krueger, and C. Y. She, 1990: High-spectral-resolution lidar measurement of tropospheric backscatter-ratio with barium atomic blocking filters. *J. Atmos. Oceanic Technol*., **7**, 876–881.

Benedetti-Michelangeli, G., F. Congeduti, and G. Fiocco, 1972: Measurement of aerosol motion and wind velocity in the lower troposphere by Doppler optical lidar, *J. Atmos. Sci*., **29**, 906–910.

Bloom, S. H., R. Kremer, P. A. Searcy, M. Rivers, J. Menders, and E. Korevaar, 1991: Long-range, noncoherent laser Doppler velocimeter, *Opt. Lett*., **16**, 1794–1796.

Bucholtz, A., D. L. Hlavka, M. McGill, K. S. Schmidt, P. Pilewskie, S. M. Davis, E. A. Reid, and A. L. Walker, 2010: Directly measured heating rates of a tropical subvisible cirrus cloud, *J. Geophys. Res*., **115**, D00J09, doi:10.1029/2009JD013128.

Cairns, B., Russell, E. E., LaVeigne, J. D., & Tennant, P. M., 2003: Research scanning polarimeter and airborne usage for remote sensing of aerosols. In *Proceedings of SPIE* (Vol. 5158, pp. 33-44).

Campbell, J. R., K. Sassen, and E. J. Welton, 2008: Elevated cloud and aerosol layer retrievals from micropulse lidar signal profiles, J. Atmos. Oceanic. Technol., 25, 685-700.

Chanin, M. L., A. Garnier, A. Hauchecorne, and J. Porteneuve, 1989: A Doppler lidar for measuring winds in the middle atmosphere, *Geophys. Res. Lett*., **16**, 1273–1276.

Comstock, J. M., T. P. Ackerman, and G. G. Mace, 2002: Groundbased lidar and radar remote sensing of tropical cirrus clouds at Nauru Island: Cloud statistic and radiative impacts. *J. Geophys. Res*., **107**, 4714, doi:10.1029/2002JD002203.

Cziczo, D. J., Froyd, K. D., Hoose, C., Jensen, E. J., Diao, M., Zondlo, M. A., Smith, J. B., Twohy, C. H., and Murphy, D. M., 2013: Clarifying the dominant sources and mechanisms of cirrus cloud formation., Science, 340, 1320–1324, doi:10.1126/science.1234145.

Davis, S., and Coauthors, 2010: In situ and lidar observations of tropopause subvisible cirrus clouds during TC4, *J. Geophys. Res*., **115**, D00J17, doi:10.1029/2009JD013093.

Del Genio, A. D., 2002: GCM simulations of cirrus for climate studies. *Cirrus*, D. K. Lynch et al., Eds., Oxford University Press, 310–326.

Del Guasta, M., 1998: Errors in the retrieval of thin-cloud optical parameters obtained with a two-boundary algorithm, Appl. Opt., 37, 5522–5540.

Del Guasta, M., and K. Niranjan, 2001: Observation of Low‐Depolarization Contrails at Florence (Italy) using a 532–1064 nm Polarization LIDAR, Geophys. Res. Lett., 28(21), 4067–4070.

Del Guasta, M., 2001: Simulation of LIDAR returns from pristine and deformed hexagonal ice prisms in cold cirrus clouds by means of ‘‘face tracing.’’ J. Geophys. Res. 106, 12,589–12,602.

Dvortsov, V. L., and S. Solomon, 2001: Response of the stratospheric temperatures and ozone to past and future increases in stratospheric humidity, *J. Geophys. Res*., **106(D7)**, 7505–7514, doi:10.1029/2000JD900637.

Eloranta, E. W., 2005: High spectral resolution lidar. *Lidar: Range-Resolved Optical Remote Sensing of the Atmosphere*, C. Weitkamp, ed. (Springer), 143-163.

Esselborn, M., M. Wirth, A. Fix, M. Tesche, and G. Ehret, 2008: Airborne high spectral resolution lidar for measuring aerosol extinction and backscatter coefficients. *Appl. Opt*, **47**, 346– 358.

Fernald, F.G., B. M. Herman and J. A. Reagan, 1972: “Determination of aerosol height distributions with lidar”, *Journal of Applied Meteorology*, **11**, 482-489.

Field, P. R., R. Wood, P. R. A. Brown, P. H. Kaye, E. Hirst, and R. Greenaway, 2003: Ice particle interarrival times measured with a fast FSSP, J. Atmos. Oceanic Technol., 20, 249–261, doi:10.1175/1520-0426(2003)020<0249:IPITMW>2.0.CO;2.

Fiocco, G., G. Beneditti-Machelangeli, K. Maschberger, and E. Madonna, 1971: *Nature Phys. Sci*., **229**, 78.

Fischer, K. W., V. J. Abreu, W. R. Skinner, J. E. Barnes, M. J. McGill, and T. D. Irgang, 1995: Visible wavelength Doppler lidar for measurement of wind and aerosol profiles during day and night, *Opt. Eng*., **34**, 499–511.

Fridlind, A.M., et al., 2004: Evidence for the predominance of mid-tropospheric aerosols as subtropical anvil nuclei, Science, 304, 718-722, doi:10.1126/science.1094947.

Garnier, A. and M. L. Chanin, 1992: Description of a Doppler Rayleigh LIDAR for measuring winds in the middle atmosphere, *Appl. Phys*., **55**, 35–40.

Garrett, T. J., A. J. Heymsfield, M. J. McGill, B. A. Ridley, D. G. Baumgardner, T. P. Bui, and C. R. Webster, 2004: Convective generation of cirrus near the tropopause, *J. Geophys. Res*., **109**, D21203, doi:10.1029/2004JD004952.

Gentry, B. and C. L. Korb, 1994: Edge technique for high accuracy Doppler velocimetry, *Appl. Opt*., **33**, 5770–5777.

Gentry, B. M., Chen, H., and Li, S. X., 2000: Wind measurements with 355-nm molecular Doppler lidar, *Opt. Lett*., **25**, 1231–1233, doi:10.1364/OL.25.001231.

Gettelman, A., Randel, W. J., Wu, F., and Massie, S. T., 2002: Transport of water vapor in the tropical tropopause layer, *Geophys. Res. Lett.*, ***29*(1)**, 1009, doi:10.1029/2001GL013818.

Grund C. J., and E.W. Eloranta, 1991: University of Wisconsin high spectral resolution lidar. *Opt. Eng*., **30**, 6–12.

Hair, J. W., and Coauthors, 2008: Airborne High Spectral Resolution Lidar for profiling aerosol optical properties. *Appl. Opt.*, **47,** 6734–6752.

Hall Jr., F. F., R. M. Huffaker, R. M. Hardesty, M. E. Jackson, T. R. Lawrence, M. J. Post, R. A. Richter, and B. F. Weber, 1984: Wind measurement accuracy of the NOAA pulsed infrared Doppler lidar, *Appl. Opt*., **23**, 2503–2506.

Hernandez, G., 1986: Fabry-Perot Interferometers, Cambridge Studies in Modern Physics, Cambridge University Press, New York.

Heymsfield, A. J.,A. Bansemer, P. R. Field, S. L. Durden, J. Stith, J. E. Dye, W. Hall, and T. Grainger, 2002: Observations and parameterizations of particle size distributions in deep tropical cirrus and stratiform precipitating clouds: Results from in situ observations in TRMM field campaigns. *J. Atmos. Sci*., **59**, 3457–3491.

Hlavka, D. L., J. E. Yorks, S. A. Young, M. A. Vaughan, R. E. Kuehn, M. J. McGill, and S. D. Rodier, 2012: Airborne validation of cirrus cloud properties derived from CALIPSO lidar measurements: Optical properties. *J. Geophys. Res*., **117**, D09207, doi:10.1029/2011JD017053.

Hovis, F.E. , M. Rhoades, R. L. Burnham, J. D. Force, T. Schum, B. M. Gentry, H. Chen, S. X. Li, J. W. Hair, A. L. Cook, and C. A. Hostetler, 2004: Single-frequency lasers for remote sensing. Proc. SPIE 5332, 263–270.

Hu, Y., Z. Liu, D. Winker, M. Vaughan, V. Noel, L. Bissonnette, G. Roy, and M. McGill, 2006: A simple relation between lidar multiple scattering and depolarization for water clouds. Optics Letters, 31, 1809-1811.

Huffaker, R. M., T. R. Lawrence, M. J. Post, J. T. Priestly, F. F. Hall Jr., R. A. Richter, and R. J. Keeler, 1984: Feasibility studies for a global wind measuring satellite system Windsat: analysis of simulated performance, *Appl. Opt.,* **23**, 2532–2536.

Huffaker, R. M. and R. M. Hardesty, 1996: Remote sensing of atmospheric wind velocities using solid-state and CO2 coherent laser systems, *Proc. IEEE*, **84**, 181–204.

Jensen, E. J., and Coauthors, 1996a: Dehydration of the upper troposphere and lower stratosphere by subvisible cirrus clouds near the tropical tropopause, *Geophys. Res. Lett*., **23**, 825–828, doi:10.1029/96GL00722.

Jensen, E. J., and Coauthors, 1996b: On the formation and persistence of subvisible cirrus clouds near the tropical tropopause, *J. Geophys. Res*., **101(D16)**, 361–375, doi:10.1029/95JD03575.

Jensen, E., and L. Pfister, 2004: Transport and freeze-drying in the tropical tropopause layer, J. Geophys. Res., 109, D02207, doi:10.1029/2003JD004022.

Jensen, E., L. Pfister, T. Bui, A. Weinheimer, E. Weinstock, J. Smith, J. Pittman, D. Baumgardner, P. Lawson, and M. J. McGill, 2005: Formation of a tropopause cirrus layer observed over Florida during CRYSTAL-FACE, *J. Geophys. Res*., **110**, D03208, doi:10.1029/2004JD004671.

Jensen, E. J., Lawson, P., Baker, B., Pilson, B., Mo, Q., Heymsfield, A. J., Bansemer, A., Bui, T. P., McGill, M., Hlavka, D., Heymsfield, G., Platnick, S., Arnold, G. T., and Tanelli, S., 2009: On the importance of small ice crystals in tropical anvil cirrus, Atmos. Chem. Phys., 9, 5519-5537, doi:10.5194/acp-9-5519-2009.

Jensen, E. J., G. Diskin, R. P. Lawson, S. Lance, T. Paul Bui, D. Hlavka, M. McGill, L. Pfister, O. B. Toon, and R. Gao, 2013: Ice nucleation and dehydration in the Tropical Tropopause Layer, PNAS, 110, 6, 2041-2046, doi:10.1073/pnas.1217104110.

Khvorostyanov, V. I.,and J. A. Curry, 2008: Analytical solutions to the stochastic kinetic equation of liquid and ice particle size spectra. Part I: Small-size fraction. *J. Atmos. Sci*., **65**, 2025–2043.

Klett, J. D., 1981: Stable analytical inversion solution for processing lidar returns. *Appl. Opt*, **20**, 211–220.

Klett, J. D., 1985: Lidar inversion with variable backscatter/extinction ratios. *Appl. Opt*, **24**, 1638–1643.

Knollenberg, R. G., 1981: Techniques for probing cloud microstructure, in Clouds, Their Formation, Optical Properties, and Effects, edited by P.V. Hobbs, pp. 15-91, Academic, San Diego, Calif.

Korb, C. L., B. Gentry, and C. Weng, 1992: The edge technique: theory and application to the lidar measurement of atmospheric winds, *Appl. Opt*., **31**, 4202–4213.

Korb, C. L., B. M. Gentry, S. X. Li, and C. Flesia, 1998: Theory of the double edge technique for Doppler lidar wind measurements, *Appl. Opt*., **37**, 3097–3104.

Lawson, R. P., B. A. Baker, C. G. Schmitt, and T. L. Jensen, 2001: An overview of microphysical properties of Arctic clouds observed in May and July 1998 during FIRE ACE, J. Geophys. Res., 106, 14,989–15,014, doi:10.1029/2000JD900789.

Lawson, R. P., B. A. Baker, B. Pilson, and Q. Mo, 2006a: In Situ observations of the microphysical properties of wave, cirrus and anvil clouds. Part II: Cirrus clouds, J. Atmos. Sci., 63, 3186–3203, doi:10.1175/JAS3803.1.

Lawson, R. P., D. O’Connor, P. Zmarzly, K. Weaver, B. A. Baker, Q. Mo, and H. Jonsson, 2006b: The 2D-S (Stereo) probe: Design and preliminary test of a new airborne, high-speed, high-resolution imaging probe, J. Atmos. Oceanic Technol., 23, 1462-1477, doi: 10.1175/JTECH1927.1.

Lawson, R. P., B. Pilson, B. Baker, Q. Mo, E. Jensen, L. Pfister, and P. Bui, 2008: Aircraft measurements of microphysical properties of subvisible cirrus in the tropical tropopause layer, Atmos. Chem. Phys., 8, 1609–1620, doi:10.5194/acp-8-1609-2008.

Lawson, R. P., E. Jensen, D. L. Mitchell, B. Baker, Q. Mo, and B. Pilson, 2010: Microphysical and radiative properties of tropical clouds investigated in TC4 and NAMMA, J. Geophys. Res., 115, D00J08, doi:10.1029/2009JD013017.

Lee, W.C., P. Dodge, F.D. Marks, P.H. Hildebrand, 1994: Mapping of airborne Doppler radar data, *J. Atmos. Oceanic Technol.*, **11**, 572–578.

Leon, D., and G. Vali, 1998: Retrieval of Three-Dimensional Particle Velocity from Airborne Doppler Radar Data, *J. Atmos. Oceanic Technol.*, **15**, 860–870.

Liu, Z., M. McGill, Y. Hu, C.A. Hostetler, M. Vaughan, and D. Winker, 2004: Validating lidar depolarization calibration using solar radiation scattered by ice clouds. Geoscience Remote Sensing Letters, 1, doi: 10.1109/LGRS.2004.829613.

Luers, James K., Robert E. Eskridge, 1998: Use of Radiosonde Temperature Data in Climate Studies. *J. Climate*, **11**, 1002–1019. doi: 10.1175/1520-0442(1998)011<1002:UORTDI>2.0.CO;2

Mace, G. G., Q. Zhang, M. A. Vaughan, R. Marchand, G. Stephens, C. R. Trepte, and D. M. Winker, 2009: A description of hydrometeor layer occurrence statistics derived from the first year of merged CloudSat and CALIPSO data, *J. Geophys. Res.*, **114**, D00A26, doi:10.1029/2007JD009755

Macke, A., Mueller, J., and Raschke, E., 1996: Single scattering properties of atmospheric ice crystals, J. Atmos. Sci., 53, 2813–2825.

Massie, S., A. Gettelman, W. Randel, and D. Baumgarder, 2002: Distribution of tropical cirrus in relation to convection, *J. Geophys. Res.*, **107(D21)**, 4591, doi:10.1029/2001JD001293.

Martins, E., V. Noel, and H. Chepfer, 2011: Properties of cirrus and subvisible cirrus from nighttime Cloud-Aerosol Lidar with Orthogonal Polarization (CALIOP), related to atmospheric dynamics and water vapor, *J. Geophys. Res.*, **116**, D02208, doi:10.1029/2010JD014519.

Mason, B. J., G. W. Bryant, and A. P. van den Heuvel, 1963: The growth habits and surface structure of ice crystals, Philos. Mag., 8, 505–526.

McFarquhar, G. M., and A. J. Heymsfield, 1996: Microphysical characteristics of three cirrus anvils sampled during the Central Equatorial Pacific Experiment. *J. Atmos. Sci.*, **53**, 2401–2423.

McFarquhar, G. M., and Coauthors, 2000: Thin and subvisual tropopause tropical cirrus: Observations and radiative impacts, *J. Atmos. Sci.*, **57(12)**, 1841– 1853, doi:10.1175/1520-0469(2000)057<1841:TASTTC>2.0.CO;2.

McGill, M.J., 1996: Recovery and Validation of Wind and Aerosol Profiles from Incoherent Doppler Lidar Measurements. PhD Thesis, University of Michigan (Ann Arbor, MI).

McGill, M. J., W. R. Skinner, and T. D. Irgang, 1997a: Analysis techniques for the recovery of winds and backscatter coefficients from a multiple channel incoherent Doppler lidar, *Appl. Opt.*, **36**, 1253–1268.

McGill, M. J., W. R. Skinner, and T. D. Irgang, 1997b: Validation of wind profiles measured using incoherent Doppler lidar, *Appl. Opt.*, **36**, 1928–1939.

McGill, M. J., M. Marzouk, V. S. Scott, and J. D. Spinhirne, 1997c: Holographic circle-to-point converter with particular applications for lidar work, *Opt. Eng.*, **36**, 2171–2175.

McGill, M.J., and J.D. Spinhirne, 1998: Comparison of two direct-detection Doppler lidar techniques, *Opt. Eng*., **37**, 2675–2686.

McGill, M.J., and R.D. Rallison, 2001: Holographic optics convert rings to points for Detection. *Laser Focus World*, **37**, 131-136.

McGill, M. J., D. Hlavka, W. Hart, V. S. Scott, J. Spinhirne, and B. Schmid, 2002: Cloud Physics Lidar: instrument description and initial measurement results. *Applied Optics*, **41**, 3725-3734.

McGill, M.J., 2003: Lidar – Remote Sensing. *Encyclopedia of Optical Engineering*, (Dekker, New York) 1103-1113.

McGill, M.J., D.L. Hlavka, W.D. Hart, E.J. Welton, and J.R. Campbell, 2003: Airborne lidar measurements of aerosol optical properties during SAFARI-2000. *Journal of Geophysical Research*, 108, doi: 10.1029/2002JD002370.

McGill, M.J., L. Li, W.D. Hart, G.M. Heymsfield, D.L. Hlavka, P.E. Racette, L. Tian, M.A. Vaughan, and D.M. Winker, 2004: Combined lidar-radar remote sensing: initial results from CRYSTAL-FACE. *J. Geophys. Res.*, **109**, doi: 10.1029/2003JD004030.

McGill, M. J., M. A. Vaughan, C. R. Trepte, W. D. Hart, D. L. Hlavka, D. M. Winker, and R. Kuehn, 2007: Airborne validation of spatial properties measured by the CALIPSO lidar. *J. Geophys. Res*., **112**, D20201, doi:10.1029/2007JD008768.

McGill, Matthew, Thorsten Markus, V. Stanley Scott, Thomas Neumann, 2013: The Multiple Altimeter Beam Experimental Lidar (MABEL): An Airborne Simulator for the ICESat-2 Mission. *J. Atmos. Oceanic Technol.*, 30, 345–352. doi: http://dx.doi.org/10.1175/JTECH-D-12-00076.1

Measures, R. M., 1984: Laser Remote Sensing: Fundamentals and Applications, Kreiger Publishing, New York.

Miller, M. A., 2008: The Cloud and Land Surface Interaction Campaign (CLASIC), Eos Trans. AGU, 89(23), Jt. Assem. Suppl., Abstract H43D-03.

Mishchenko, M. I., W. B. Rossow, A. Macke, and A. A. Lacis, 1996: Sensitivity of cirrus cloud albedo, bidirectional reflectance and optical thickness retrieval accuracy to ice particle shape, J. Geophys. Res., 101,16,973–16,985.

Morrison, H. and Grabowski, W. W., 2011: Cloud-system resolving model simulations of aerosol indirect effects on tropical deep convection and its thermodynamic environment, Atmos. Chem. Phys., 11, 10503-10523, doi:10.5194/acp-11-10503-2011.

Noel, V., D. M. Winker, M. McGill, and P. Lawson, 2004: Classification of particle shapes from lidar depolarization ratio in convective ice clouds compared to in situ observations during CRYSTAL-FACE, J. Geophys. Res., 109, D24213, doi:10.1029/2004JD004883.

Nowottnick, E., Colarco, P., da Silva, A., Hlavka, D., and McGill, M. (2011), The fate of Saharan dust across the Atlantic and implications for a Central American dust barrier, Atmos. Chem. Phys. Discuss., 11, 8337-8384, doi:10.5194/acpd-11-8337-2011.

Pfister, L., and Coauthors, 2001: Aircraft observations of thin cirrus clouds near the tropical tropopause, *J. Geophys. Res*., **106(D9)**, 9765–9786, doi:10.1029/2000JD900648.

Piironen P. and E.W. Eloranta, 1994: Demonstration of a high-spectral-resolution lidar based on an iodine absorption filter. *Opt. Lett*., **19**, 234–236.

Platt, C. M. R. and Coauthors, 2002: LIRAD observations of tropical cirrus clouds in MCTEX. Part I: Optical properties and detection of small particles in cold cirrus. J. Atmos. Sci., 59, 3145– 3162.

Potter, B. E., and J. R. Holton, 1995: The role of monsoon convection in the dehydration of the lower tropical stratosphere, *J. Atmos. Sci*., **52**, 1034–1050.

Poulida, O., Dickerson, R.R. and Heymsfield, A., 1996: Stratosphere-troposphere exchange in a midlatitude mesoscale convective complex: 1. Observations. *Journal of Geophysical Research 101: doi: 10.1029/95JD03523. issn: 0148-0227.*

Powell, Scott W., Robert A. Houze, Anil Kumar, Sally A. McFarlane, 2012: Comparison of Simulated and Observed Continental Tropical Anvil Clouds and Their Radiative Heating Profiles. *J. Atmos. Sci.*, **69**, 2662–2681. doi: http://dx.doi.org/10.1175/JAS-D-11-0251.1

Reichardt, J., S. Reichardt, A. Behrendt, and T. J. McGee, 2002: Correlations among the optical properties of cirrus-cloud particles: Implications for spaceborne remote sensing. *Geophys. Res. Lett*., **29(14)**, 1668, doi:10.1029/2002GL014836.

Rickenbach, T. M., 1999: Cloud top evolution of tropical oceanic squall lines from radar reflectivity and infrared satellite data. *Mon. Wea. Rev*., **127**, 2951–2976.

Rogers, R. R., Hair, J. W., Hostetler, C. A., Ferrare, R. A., Obland, M. D., Cook, A. L., Harper, D. B., Burton, S. P., Shinozuka, Y., McNaughton, C. S., Clarke, A. D., Redemann, J., Russell, P. B., Livingston, J. M., and Kleinman, L. I., 2009: NASA LaRC airborne high spectral resolution lidar aerosol measurements during MILAGRO: observations and validation. *Atmos. Chem. Phys*., 9, 4811-4826, doi:10.5194/acp-9-4811-2009.

Russell, P. B., T. J. Swissler, and M. P. McCormick, 1979: Methodology for error analysis and simulation of lidar aerosol measurements, Appl. Opt., 18, 3783–3797.

Santacesaria, V., and Coatuhors, 2003: Clouds at the tropical tropopause: A case study during the APE-THESEO campaign over the western Indian Ocean, *J. Geophys. Res*., **108(D2)**, 4044, doi:10.1029/2002JD002166.

Sassen, K., and S. Benson, 2001: A midlatitude cirrus cloud climatology from the Facility for Atmospheric Remote Sensing. Part II: Microphysical properties derived from lidar depolarization. J. Atmos. Sci., 58, 2103– 2112.

Sassen, K., 2002: Cirrus: A modern perspective. *Cirrus*, D. K. Lynch et al., Eds., Oxford University Press, 11–40.

Schwiesow, R.L., F. Köpp, and C. Werner, 1985: Comparison of Lidar-Measured Wind Values Obtained by Full Conical Scan, Conical Sector Scan, and Two Point Techniques, *J. Atmos. Oceanic Technol*., **2**, 3.

Seifert, P., Ansmann, A., Müller, D., Wandinger, U., Althausen, D., Heymsfield, A. J., Massie, S. T., and Schmitt, C., 2007: Cirrus optical properties observed with lidar, radiosonde, and satellite over the tropical Indian ocean during the aerosol-polluted northeast and clean maritime southwest monsoon, J. Geophys. Res., 112, D17205, doi:10.1029/2006JD008352.

Shapiro, M. A., and A. J. Thorpe, 2004: THORPEX: A global atmospheric research program for the beginning of the 21st century, WMO Bull., 53, 222– 226.

She, C. Y., R. J. Alvarez II, L. M. Caldwell, and D. A. Krueger, 1992: High-spectral-resolution Rayleigh–Mie lidar measurement of aerosol and atmospheric profiles. *Opt. Lett*., **17**, 541–543.

Shipley, S. T., D. H. Tracy, E. W. Eloranta, J. T. Tauger, J. T. Sroga, F. L. Roesler, and J. A. Weinman, 1983: High spectral resolution lidar to measure optical scattering properties of atmospheric aerosols. 1: Theory and instrumentation. *Appl. Opt*., **22**, 3716–3724.

Souprayen, C., Garnier, A., Hertzog, A., Hauchecorne, A., and Porteneuve, J., 1999: Rayleigh-Mie Doppler wind lidar for atmospheric measurements. I. Instrumental setup, validation, and first climatological results, *Appl. Optics*, **38**, 2410–2421, doi:10.1364/AO.38.002410.

Spinhirne J. D., J. A. Reagan, and B. M. Herman, 1980: Vertical distribution of aerosol extinction cross section and inference of aerosol imaginary index in the troposphere by lidar technique. *J. Appl. Meteor*., **19**, 426–438.

Stephens, G. L., S. C. Tsay, J. P. W. Stackhouse, and P. J. Flatau, 1990: The relevance of the microphysical and radiative properties of cirrus cloud on climate and climatic feedback. *J. Atmos. Sci*., **47**, 1742–1753.

Stephens, G. L., 2005: Cloud feedbacks in the climate system: A critical review, *J. Climate*, **18**, 237-273

Tenti, G., C. D. Boley, and R. C. Desai, 1974: On the kinetic model description of Rayleigh–Brillouin scattering from molecular gases. *Can. J. Phys*, **52**, 285–290.

Toon, O. B., et al., 2010: Planning, implementation, and first results of the Tropical Composition, Cloud and Climate Coupling Experiment (TC4), *J. Geophys. Res.*, **115**, D00J04, doi:10.1029/2009JD013073.

Twomey, S., 1977: The influence of pollution on the shortwave albedo of clouds, J. Atmos. Sci., 34, 1149–1152.

van Diedenhoven, B., Cairns, B., Geogdzhayev, I. V., Fridlind, A. M., Ackerman, A. S., Yang, P., and Baum, B. A., 2012: Remote sensing of ice crystal asymmetry parameter using multidirectional polarization measurements – Part 1: Methodology and evaluation with simulated measurements, Atmos. Meas. Tech., 5, 2361–2374, doi:10.5194/amt-5-2361-2012.

van Diedenhoven, B., Cairns, B., Fridlind, A. M., Ackerman, A. S., and Garrett, T. J., 2013: Remote sensing of ice crystal asymmetry parameter using multi-directional polarization measurements – Part 2: Application to the Research Scanning Polarimeter, Atmos. Chem. Phys., 13, 3185-3203, doi:10.5194/acp-13-3185-2013.

Vaughan, J. M., 1989: The Fabry-Perot Interferometer, Adam Hilger, Philadelphia.

Vaughan, M. A., Z. Liu, M. J. McGill, Y. Hu, and M. D. Obland, 2010: On the spectral dependence of Backscatter from cirrus clouds: Assessing CALIOP's 1064 nm calibration assumptions using cloud physics lidar measurements, J. Geophys. Res., 115, D14206, doi:10.1029/2009JD013086.

Wang, Z., and K. Sassen, 2002: Cirrus cloud microphysical property retrieval using lidar and radar measurements. Part I: Algorithm description and comparison with in situ data. *J. Appl. Meteor*., **41**, 218–229.

Werner, C., 2005: "Doppler Wind Lidar," in *Lidar: Range-Resolved Optical Remote Sensing of the Atmosphere*, C. Weitkamp, ed. (Springer), 325-354.

Winker, D. M., 2003: Accounting for multiple scattering in retrievals from space lidar. *Lidar Scattering Experiments*, C. Werner, U. Oppel, and T. Rother, ed., International Society for Optical Engineering (SPIE Proceedings, Vol. 5059), 128–139.

Winker, D. M., M. A. Vaughan, A. H. Omar, Y. Hu, K. A. Powell, Z. Liu, W. H. Hunt, and S. A. Young, 2009: Overview of the CALIPSO Mission and CALIOP Data Processing Algorithms. *J. Atmos. Oceanic Technol*., **26**, 1105-1119, doi:10.1175/2009JTECHA1281.1.

Yang, P., et al., 2001: Sensitivity of cirrus bidirectional reflectance to vertical imhomogeneous of ice crystals habits and size distribution for two Moderate-Resolution Imaging Spectroradiometer (MODIS), J. Geophys. Res., 106, 17,267–17,291.

Yorks, J. E., D. L. Hlavka, W. D. Hart, M. J. McGill, 2011a: Statistics of Cloud Optical Properties from Airborne Lidar Measurements. *J. Atmos. Oceanic Technol.*, **28**, 869–883. doi: http://dx.doi.org/10.1175/2011JTECHA1507.1

Yorks, J. E., D. L. Hlavka, M. A. Vaughan, M. J. McGill, W. D. Hart, S. Rodier, and R. Kuehn, 2011b: Airborne validation of cirrus cloud properties derived from CALIPSO lidar measurements: Spatial properties, *J. Geophys. Res*., **116**, D19207, doi:10.1029/2011JD015942.

Yorks, J. E., M. McGill, V. S. Scott, A. Kupchock, S. Wake, D. Hlavka, W. Hart, P. Selmer, 2014a: The Airborne Cloud-Aerosol Transport System, Part I: Overview and Description of the Instrument and Retrieval Algorithms, *J. Atmos. Oceanic Technol*., submitted.

Yorks, J. E., M. McGill, D. Hlavka, W. Hart, P. Selmer, 2014b: The Airborne Cloud-Aerosol Transport System, Part II: Assessment of Cloud and Aerosol Retrievals Using Coincident Cloud Physics Lidar Data, *J. Atmos. Oceanic Technol*., submitted.

Young, A.T., 1981: Rayleigh scattering. *Phys. Today*, 35, 42–48.

Young, S. A., 1995: Analysis of lidar backscatter profiles in optically thin clouds, Appl. Opt., 34, 7019–7031.

Young, S. A., and M. A. Vaughan, 2009: The retrieval of profiles of particulate extinction from Cloud-Aerosol Lidar Infrared Pathfinder Satellite Observations (CALIPSO) data: Algorithm description*. J. Atmos. Oceanic Technol.*, **26**, 1105–1119.

Young, Stuart A., Mark A. Vaughan, Ralph E. Kuehn, David M. Winker, 2013: The Retrieval of Profiles of Particulate Extinction from Cloud–Aerosol Lidar and Infrared Pathfinder Satellite Observations (CALIPSO) Data: Uncertainty and Error Sensitivity Analyses. *J. Atmos. Oceanic Technol.*, **30**, 395–428. doi: http://dx.doi.org/10.1175/JTECH-D-12-00046.1

Zhao, Y., G. G. Mace, and J. M. Comstock, 2011: The occurrence of particle size distribution bimodality in midlatitude cirrus as inferred from ground-based remote sensing data, *J. Atmos. Sci.*, **68**, 1162–1177, doi:10.1175/2010JAS3354.1.